Peristaltic Flows with Heat and Mass Transfer in a Curved Channel

by

Raheel Ahmed

Department of Mathematics and Statistics
Faculty of Basic and Applied Sciences
International Islamic University, Islamabad, Pakistan
2018

Peristaltic Flows with Heat and Mass Transfer in a Curved Channel

by

Raheel Ahmed

Supervised by

Dr. Nasir Ali

Department of Mathematics and Statistics
Faculty of Basic and Applied Sciences
International Islamic University, Islamabad, Pakistan
2018

Peristaltic Flows with Heat and Mass Transfer in a Curved Channel

by

Raheel Ahmed

A DISSERTATION SUBMITTED IN THE PARTIAL FULFILLMENT OF THE REQUIREMENTS FOR THE DEGREE OF

DOCTOR OF PHILOSOPHY

IN

MATHEMATICS

Supervised by

Dr. Nasir Ali

Department of Mathematics and Statistics
Faculty of Basic and Applied Sciences
International Islamic University, Islamabad, Pakistan
2018

Author's Declaration

I, **Raheel Ahmed** Reg. No. **18-FBAS/PHDMA/F12** hereby state that my Ph.D. thesis titled: **Peristaltic Flows with Heat and Mass Transfer in a Curved Channel** is my own work and has not been submitted previously by me for taking any degree from this university, **International Islamic University, Sector H-10, Islamabad, Pakistan** or anywhere else in the country/world.

At any time if my statement is found to be incorrect even after my Graduation the university has the right to withdraw my Ph.D. degree.

Name of Student: ***(Raheel Ahmed)***
Reg. No. **18-FBAS/PHDMA/F12**
Dated: **21/12/2018**

Plagiarism Undertaking

I solemnly declare that research work presented in the thesis titled: **Peristaltic Flows with Heat and Mass Transfer in a Curved Channel** is solely my research work with no significant contribution from any other person. Small contribution/help wherever taken has been duly acknowledged and that complete thesis has been written by me.

I understand the zero tolerance policy of the HEC and University, **International Islamic University, Sector H-10, Islamabad, Pakistan** towards plagiarism. Therefore, I as an Author of the above titled thesis declare that no portion of my thesis has been plagiarized and any material used as reference is properly referred/cited.

I undertake that if I am found guilty of any formal plagiarism in the above titled thesis even after award of Ph.D. degree, the university reserves the rights to withdraw/revoke my Ph.D. degree and that HEC and the University has the right to publish my name on the HEC/University Website on which names of students are placed who submitted plagiarized thesis.

Student/Author Signature: _____

Name: **(Raheel Ahmed)**

Certificate of Approval

This is to certify that the research work presented in this thesis, entitled: **Peristaltic Flows with Heat and Mass Transfer in a Curved Channel** was conducted by **Mr. Raheel Ahmed,** Reg. No. **18-FBAS/PHDMA/F12** under the supervision of **Dr. Nasir Ali** no part of this thesis has been submitted anywhere else for any other degree. This thesis is submitted to the **Department of Mathematics & Statistics, FBAS, IIU, Islamabad** in partial fulfillment of the requirements for the degree of **Doctor of Philosophy in Mathematics, Department of Mathematics & Statistics, Faculty of Basic & Applied Science, International Islamic University, Sector H-10, Islamabad, Pakistan.**

Student Name: Raheel Ahmed **Signature: _____**

Examination Committee:

a) **External Examiner 1:**
Name/Designation/Office Address **Signature: _____**

Prof. Dr. Saleem Asghar
Professor of Mathematics,
Department of Mathematics,
COMSATS, IIT, Park Road, Chak Shahzad,
Islamabad.

b) **External Examiner 2:**
Name/Designation/Office Address) **Signature: _____**

Prof. Dr. Tasawar Hayat
Professor of Mathematics,
Department of Mathematics,
QAU, Islamabad

c) **Internal Examiner:**
Name/Designation/Office Address) **Signature: _____**

Dr. Ahmer Mehmood
Associate Professor

Supervisor Name:
Dr. Nasir Ali **Signature: _____**

Name of Dean/HOD:
Prof. Dr. Muhammad Sajid, T.I **Signature: _____**

Acknowledgements

I express my utmost gratitude to **Almighty Allah**, The most Beneficent and The most Merciful Who bestowed upon me the potential and ability to accomplish this intellectual endeavor. I offer my salaams to The **Holy Prophet (PBUH)**, who is forever a torch bearer of guidance for humanity as whole. He is a source of knowledge and blessings for the entire creations.

I express my sincere and respectful admiration to my worthy supervisor **Dr. Nasir Ali** for his scholarly guidance, mentorship and vast knowledge that help me to embark upon this important work. I also pay my regards to all my respected teachers who always directed me to right dimensions and made it possible for me to achieve an attractive goal.

I am thankful to whole of my family for their endurance and support throughout my studies. Especially my mother, brothers and sisters who always remain a source of motivation for me and encourage me to accomplish this crucial task. I am also grateful to my wife and kids Hurain Raheel and Zimal Raheel without whom support this would be a difficult task to achieve.

I am also thankful to all of my friends who supported me during my gloomiest time, particularly, Dr. Khurram Javed, Dr. Asif Javed, Dr. Samiullah, Dr. Mubashar Mehr, Dr. Bilal, Dr. Hafiz Atif, Zeeshan Asghar, Kaleemullah, Sadaqat Hussain, Waris Saeed, Arshad Siddique and M. Usman.

Raheel Ahmed

DEDICATION

This thesis is dedicated to my loving father (late)

& brother (late).

Preface

Peristaltic pumping is a fluid transport phenomenon which is attained through a progressive dynamic wave of expansion or contraction propagating along the walls of a distensible tube containing fluid. Many researchers, biologists, engineers and physicist studied peristaltic transport in different geometries due to its wide range applications in numerous fields. It is an intrinsic phenomena of several biological/physiological systems such as reproductive system, nervous system, digestive system, cardiovascular system and renal system. Several modern engineering devices also operate on the principle of peristalsis. Examples abound: diabetic pumps, corrosive fluid transport pumps in nuclear industry**,** roller and finger pumps, pharmacological delivery pumps, infusion pumps etc. In recent times, electro osmosis-modulated peristaltic transport in micro fluids channel is proposed as a model for the design of lab-on-a-chip device. It is evident from above mentioned applications that peristaltic motion is the nature's as well as humans way of transporting the fluids.

Heat transfer is an important phenomenon of nature, which works on the first law of thermodynamics. According to this law the energy added per unit mass to a closed system increases the total energy per unit mass of the system (fluid). The application of this law to flowing fluid yield the well-known energy equation. The study of non-isothermal peristaltic flows required the application of both momentum and energy equations. The motivation to analyze heat transfer in peristaltic flows arises due to applications of such flow in hemodialysis process, blood pumps, dispersion of chemical impurities, heart lung machine and corrosive fluids transport in machines. Moreover, temperature variations inside the fluid may affect the bolus movement. The latest techniques of heat transfer like

cryosurgery and laser therapy have also inspired researchers for thermal modeling in tissues.

Mass transfer phenomenon is vital in the diffusion process such as the nutrients diffuse out from the blood to the contiguous tissues. A multifarious relationship is observed between driving potentials and fluxes when heat and mass transfer are considered simultaneously. The analysis of peristaltic flow with heat and mass transfer is of valuable importance due to its promising applications in biomedical sciences. Example abound: conduction in tissue, convection due to circulation of blood in porous tissue, food processing and vasodilation. It is important to point out the mass diffusion from boundaries into the fluid is always happening in physiological flows and therefore a complete analysis of such flows must incorporate concentration equation along with momentum and energy equations.

The utility of peristaltic flow with heat and mass transfer is further enhanced when curvature effects with non-Newtonian characteristics of the fluid are also integrated in the whole analysis. However, not much literature is available pertaining to peristaltic flows of complex fluids with heat/ mass transfer through a curved channel. Motivated by this fact the main objective of this thesis is to develop and simulate mathematical models of peristaltic flows with heat/ mass transfer in a curved channel. The model development is achieved through the use of fundamental conservation laws of mass, momentum, energy and concentration for fluids. Employing these laws, a system of partial differential equations is developed which is later simplified by using physiologically relevant approximations. The reduced system is simulated by using appropriate numerical technique. The solution obtained through this technique is later used to explain physical

structure of flow and heat/ mass transfer features. This thesis is composed on following nine chapters.

Chapter 1 starts with brief explanation of the topics such as peristaltic flow, non-Newtonian fluids and heat/ mass transfer. The fundamental equations and dimensionless number related to the topic of research are provided in the main body. A comprehensive review of the available literature on peristaltic flows is also presented at the end.

Chapter 2 investigates the hydromagnetic peristaltic flow in a porous-saturated heated channel by utilizing Darcy-Forchiemmer law. The equations for velocity, temperature and mass concentration are developed by using the delta approximation. A finite difference scheme is employed to solve these equations. The effects of pertinent rheological parameters are thoroughly investigated. It is observed that presence of porous media obstructs the flow velocity and reduces circulations of streamlines. The results of this chapter are published in **Thermal Science; TSCI170825006A.**

Chapter 3 explores the heat and mass transfer to mixed convective hydromagnetic peristaltic flow in a curved channel in the presence of joule heating. Boussinesq approximation is used to couple the momentum and energy equations. Numerical solution of these equations is developed by neglecting the inertial and streamline curvature effects. The results of simulations are displayed graphically. It is noted that thermal Grashof number enhances the temperature while it has an opposite effect on mass concentration. The results of this chapter are submitted for publication in **Theoretical and Computational Fluid Dynamics.**

Chapter 4 presents the analysis of heat/ mass transfer to peristaltic flow of Sisko fluid in a curved channel. The fundamental equations are derived by employing an orthogonal coordinate system for delta approximation. The effect of relevant parameter are observed on velocity, pressure rise, temperature and concentration fields and streamlines. It is observed that circulating bolus shift from upper half to the lower half of the channel as we switch from shear-thinning to shear-thickening fluid. The results of this chapter are published in **Thermal Science; TSCI161018115A.**

Chapter 5 provides modeling and simulations for peristaltic flow of Carreau fluid model with heat/ mass transfer in a curved channel. The calculations for axial velocity, pressure rise per wavelength, temperature and concentration fields and stream function are carried out under delta approximation in the wave frame by employing suitable numerical implicit finite difference technique. It is noticed that rapid changes occur in flow velocity and streamlines for shear-thinning fluids due to which a boundary layer develop in the vicinity of channel walls for increasing values of Hartmann number. Furthermore, the amplitude of heat transfer coefficient is suppressed for larger values of channel curvature, power-law index and Hartmann number. The results of this chapter are submitted for publication in **Communications in Theoretical Physics**.

Chapter 6 investigates the analysis of peristaltic flow of Rabinowitsch fluid in a curved channel with heat transfer. The reduced set of equations is solved via a semi-analytic procedure while energy equation is simulated numerically using Mathematica routine "NDSolve". The effects of important parameters on flow velocity, temperature field and streamlines are shown in detail. It is observed that with increasing coefficient of

pseudoplasiticity flow velocity achieve symmetric profile. Moreover, flow velocity becomes symmetric with increasing dimensionless radius of curvature. The fluid temperature inside the channel rises with increasing the coefficient of pseudoplasiticity. The results of this chapter are published in **Zeitschrift für Naturforschung A 2016; 72(3): 245–251**.

Chapter 7 investigates the effects on heat and mass transfer in peristaltic flow of magnetically influenced incompressible micropolar fluid model through a curved channel. The set of fundamental equations is derived by utilizing delta approximation. The effects of coupling number, micropolar parameter, Hartmann number and curvature parameter on velocity, pressure rise and temperature and concentration fields are thoroughly examined. It is observed that the axial velocity rises with increasing micropolar parameter in vicinity of the lower wall while it shows opposite behavior near the upper wall. The fluid bolus concentrated in vicinity of upper part of the channel for lower values of micropolar parameter splits into two parts with increasing micropolar parameter. The results of this chapter are submitted for publication in **Journal of fluid mechanics.**

Chapter 8 reveals the features of heat and mass transfer in peristaltic flow of bi-viscosity fluid through a porous-saturated curved channel in the presence of magnetic field and Joule heating effect. The governing equations are reduced by using delta approximation and then integrated numerically using **FDM**. It is noted that bi-viscosity fluid parameter, permeability parameter and Hartmann number have similar effects on the axial velocity. The results of this chapter are submitted for publication in **Results in physics.**

Contents

Nomenclature

a	Amplitude of upper wall
a^*	Viscosity parameter
b_1	Index of consistency
Br	Brinkmann number
B^*	Characteristic magnetic induction
C_0	Mass concentration at lower wall
C_1	Mass concentration at upper wall
c	Wave speed
c_p	Specific heat at constant pressure
c_s	Concentration susceptibility
D_u	Dufour Effect
D_m	Molecular diffusivity
$\mathbf{E}$	Electric field
$\boldsymbol{e_R}$	Radial direction unit vector
$\boldsymbol{e_X}$	Azimuthal direction unit vector
$\boldsymbol{e_{lkm}}$	Permutation symbol
$\mathbf{F}$	Body force per unit mass
F_0	Forchiemmer parameter
Gr_C	Concentration Grashof number
Gr_T	Thermal Grashof number
g	Gravity
Ha	Hartmann number
$\mathbf{I}$	Identity tensor
$\mathbf{J}$	Current density
j	Micro moment of inertia
k	Thermal conductivity
k^*	Permeability of porous medium

K_T	Thermal diffusivity
k_1	Chemical reaction parameter
k_2	Dynamic micro-rotation
L	Characteristic length
m_{kl}	Moment stress tensor
n	Index of power-law
P	Pressure
Q	Amount of heat flux
q	Flow rate in moving frame
R	Radial coordinate in laboratory frame
Re	Reynolds number
$\mathbf{S}$	Extra stress tensor
Sr	Soret number
Sh	Sherwood number
T	Fluid temperature
T_0	Lower wall temperature
T_1	Upper wall temperature
t	Time
T_m	Mean fluid temperature
T_∞	Ambient Temperature
u_1, u_2	velocity components
w_k	Micro-rotation velocity
We	Weissenberg number
w	Half width of the curved channel
z	Coefficient of heat transfer

Greek letters

ρ	Density
Φ	Dissipation function
μ	Dynamic viscosity parameter
μ_b	Plastic dynamic viscosity
μ_0	Viscosity at zero-shear-rate
μ_∞	Viscosity at infinite-shear-rate
Π	Second invariant
Γ	Time constant
χ	Axial coordinate in laboratory frame
α	Ratio of infinite to zero shear-rate viscosity
γ	Dimensionless radius of curvature
$\dot{\gamma}$	Stress relation time
λ	Specific process time
δ	Wave number
λ, λ'	Amplitude ratio
β	Bi-viscosity fluid parameter
β'	Coefficient of pseudoplasiticity
λ^*	Wavelength
ϕ	Concentration
ψ	Stream function
β_T	Thermal expansion coefficient
β_C	Concentration expansion coefficient
$\alpha^*, \beta^*, \gamma,^*$	Coefficient of angular velocity

Chapter 1

Introduction

The objective of this chapter is to elaborate fundamental concepts such as non-Newtonian fluids, peristalsis and heat and mass transfer. The conservation laws necessary for flow and heat and mass transfer analyses are briefly explained. The dimensionless numbers related to the topic of thesis are defined. A brief review of available literature on the topic under consideration is also provided.

1.1 Peristaltic flow

The phenomenon of fluid transport is known as peristaltic pumping which is attained through a progressive dynamic wave of expansion or contraction propagating along the walls of a distensible tube containing fluid. Due to wide range of applications in engineering and medical sciences the peristaltic transport via tubes /channels have attracted substantial consideration of researchers. It is an inherent phenomena of numerous biological/physiological systems such as transport of lymph in the lymphatic vessels, chyme in small intestine, blood in small blood vessels, cardiovascular flows, fluids from the mouth through the esophagus (**Fig. 1.1**), movement of refluxes in neuron, the locomotion of worms and transport of urine from kidney to bladder. Modern machines which operate on the principle of peristalsis are roller and finger pumps, diabetic pumps (**Fig. 1.2**), corrosive fluid transport in nuclear industry**,** pharmacological delivery systems,

transport of sanitary fluids, uterine cavity, etc. Recently, electro osmosis-modulated peristaltic transport in micro fluids channel is proposed as a model for the design of lab-on-a-chip device. From above discussion it is clear that peristaltic motion is the nature's way of transporting the fluid in human beings.

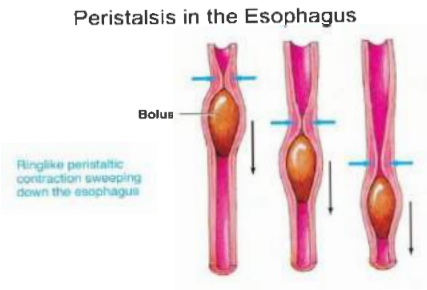

Fig. 1.1: Motion of food bolus through esophagus.

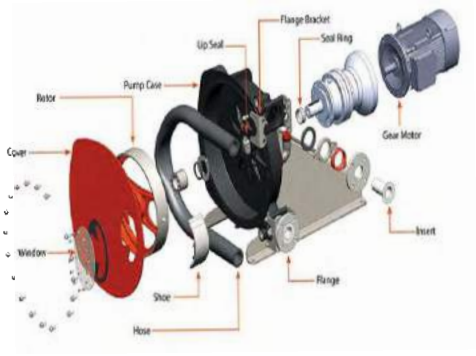

Fig. 1.2: Schematic diagram of peristaltic pump.

The peristaltic flow through curved channel is pertinent to many biological, environmental and industrial processes. Examples are physiological tubes, glandular ducts, laser accelerators, optical synchrotrons, laser guiding in curved plasma channels, harmonic generators, micro heat exchangers and circular x-ray. Therefore, it appears sound to study the peristaltic flow in a curved channel. In past, several researchers worked on peristaltic motion of Newtonian and non-Newtonian materials in different geometric setups subject to various boundary conditions. Several important aspects arising from consideration of porous media, magnetic field are also analyzed. Two frequently used assumptions in the modeling of peristaltic flows are known as long wavelength assumption (delta-approximation) and low Reynolds number assumption. These assumptions are quite

compatible as far as peristaltic flows in physiological system are concerned. However, there are some situations for instance, in engineering devices where such assumptions do not give reliable results. In such situations the above mentioned assumptions are dropped and the analysis is performed for complete two-dimensional equations.

1.2 Non-Newtonian fluids

The theory of fluids has gained attention of scientists, engineers, biologists and mathematicians in recent times. Generally, fluids are characterized as Newtonian and non-Newtonian fluid. Newtonian fluids are those in which the viscous stresses arising from their flow, at every point, are linearly proportional to the local strain rate. Newtonian fluids are the simplest mathematical models of fluids that account for viscosity. On the other hand, Navier-Stokes equations are unable to describe the flow of many fluids including suspensions, clay coatings, liquid detergents, drilling muds and oils etc. These fluids are known as non-Newtonian fluids. Many physiological, pharmacological and industrial liquids are known to be non-Newtonian in nature including bile, blood, mucus, digestive fluids, capillary fluids, bio membranes, custard, ketchup, starch, paint, flow of liquid metals, nuclear slurries, alloys, etc. In order to accurately describe the rheology of non-Newtonian fluids analysts have designed a number of non-Newtonian fluid models, which lead to the highly non-linear differential equations. Commonly used non-Newtonian model in literature are power-law model, Jeffery fluid model, Sisko model, Oldroyd-B model, Giesekus model, Carreau model, Johnson-Segalman model etc. Generally, non-Newtonian fluids are categorized as generalized Newtonian fluids (GNF) and viscoelastic fluids. For

later fluids, the shear stress is a function of shear rate at the specific interval, but independent of the history of deformation. Though GNF is non-Newtonian in nature but its fundamental equation is a generalized form of the Newtonian fluid. GNF are categorized in two main types, namely, time-independent GNF and time-dependent GNF. The fluids for which the value of shear rate at a point, within the fluid, is deliberated only by the present value of shear stress at that point are called time-independent fluids. These fluids are further classified as shear-thinning (pseudoplastic behavior) and shear-thickening (dilatant behavior) fluids depending upon viscosity. In shear-thinning fluids the viscosity gradually decreases with increasing shear rate while in case of shear-thickening fluids viscosity increases with increasing shear rate. The fluid for which the shear rate and shear stress shows dependence on the duration of kinematic and shearing history are called time-dependent fluid. These fluids are explicitly divided into two types: thixotropic fluids and rheopectic fluids. Thixotropy is a time-dependent shear thinning property while rheopexy is time-dependent shear thickening property.

The viscoelastic fluids are non-Newtonian fluids, possessing both viscous and elastic properties. Viscoelastic fluids in contrast to Newtonian liquids are not described by a universal equation. Hence a number of constitutive equations have been developed to describe rheological characteristics. The flows of such fluids are governed by higher order, complicated and more nonlinear equations than the Navier- Stokes equations. Examples of viscoelastic models are: Maxwell model, Oldroyd-B model, Burgers model, Generalized Maxwell model, Giesekus model and PTT model.

1.3 Heat and mass transfer

Heat transfer is an essential phenomenon of nature, which works on first law of thermodynamics, according to this law heat always travel from a region of higher concentration to a region of lower concentration. There are three basic modes of heat transfer namely, conduction, convection and radiation. In primary mode heat is transferred due to vibration of adjacent atoms due to which heat is transferred from region of higher temperature to lower temperature. Fluids and gases are less conductive than solids because they are less dense. In convection heat is transferred by physical movement of molecules. There are two types of convection i.e., natural convection and forced convection. Heat is transferred by convection in numerous phenomena for example wind, oceanic currents and movements within the Earth's mantle. In case of radiation heat is transferred due to waves. Radiation occurs without an intervening medium, for example, energy from the sun travels through the vacuum to the Earth due to convection. In peristalsis heat transfer is beneficial in number of applications for instance hemodialysis process, blood pumps, dispersion of chemical impurities, heart lung machine and corrosive fluids transport in machines. Physiologically thermal properties of tissues are analyzed by using evaporation technique. The latest techniques of heat transfer like cryosurgery and laser therapy have also inspired researchers for thermal modeling in tissues.

Mass concentration is measure of the extent to which a fluid resists a change in its direction or speed when a force is applied. Mass transfer phenomenon is vital in the diffusion process such as the nutrients diffuse out from the blood to the contiguous tissues. A multifarious relationship is observed between driving potentials and fluxes when heat/ mass transfer are

deliberated simultaneously. When heat/ mass transfer arise jointly in a moving fluid, then it affect many transport processes present in nature and also the applications relating to science and engineering. Studies pertaining to heat/mass transfer in peristaltic flows through straight geometries have also been carried out by various researchers. This is because of numerous applications of heat and mass transfer in industrial and physiological processes such as condensation, crystallization, evaporation, etc.

1.4 Objective

The purpose of present research is to investigate the peristaltic flow with heat and mass transfer in a curved channel through the use of different non-Newtonian fluid models. The system of equations is developed for the case when wave number is vanishingly small. A well-tested finite difference scheme is employed for the solution. The existing literature surveyed by the author deals with non-isothermal peristaltic flows of different non-Newtonian fluids in planar channel, axisymmetric tube, curved channel or a rectangular duct. However, less attention is given to the simultaneous effects of heat and mass transfer in peristaltic flow through curved geometry. Motivated by this fact, the research carried out in this thesis provides improvement of existing mathematical models of peristaltic transport of Newtonian and generalized Newtonian fluids, interpretation of the fundamental equations and examination of different key factors on flow and heat/ mass transfer features.

The analysis also take into account the presence of pertinent effects such as magnetohydrodynamic, Joule heating, Soret and Dufour and porous media effects. The

effects of porous medium are studied by utilizing Darcy's law which relates pressure gradient and flow velocity linearly through the porous medium. Similarly, Maxwell's equation with generalized Ohm's law have been used to study the magnetohydrodynamics effects.

1.5 Dimensionless numbers

The important dimensionless numbers pertaining to the topic of research are briefly explained in this section.

1.5.1 Reynolds number

Reynolds number is defined as ratio of the inertial force to the viscous force and usually denoted by Re. Mathematically, it is given by

$$\mathrm{Re} = \frac{\rho c L}{\mu}. \tag{1.1}$$

Reynolds number is used to describe two main types of flow i.e., laminar and turbulent flow. Laminar flows with vanishingly small Reynolds number are called creeping flows. Peristaltic flows, specifically relevant to physiology, usually occur at very low Reynolds number. For turbulent flow inertial force is dominant with large Reynolds number. This flow produces vortices, fluctuations and eddies.

1.5.2 Brinkman number

Brinkman number is defined as ratio of heat produced by viscous dissipation to the heat transported by molecular conduction. The higher value of Brinkman number correspond to increasing temperature rise due to lesser conduction of heat produced by viscous dissipation. Mathematically, Brinkmann number is defined as

$$Br = \frac{\mu c^2}{k\left(T_0 - T_1\right)}, \tag{1.2}$$

where *k*, T_0 and T_1 are the thermal conductivity, temperature of lower and upper wall, respectively.

1.5.3 Weissenberg number

Weissenberg number is used to describe the relation of stress relaxation time ($\dot{\gamma}$) and specific process time (λ) of the fluid. It is a dimensionless number used to describe viscoelastic flows. It is given by,

$$We = \dot{\gamma}\,\lambda. \tag{1.3}$$

1.5.4 Heat transfer coefficient

The heat transfer coefficient is proportionality constant between flux and thermodynamic driving force for the flow of heat, given by

$$z = \frac{Q}{\Delta T}, \tag{1.4}$$

where z is the heat transfer coefficient, Q is the amount of heat flux and ΔT is temperature difference between solid surface and area adjacent to fluid.

1.5.5 Hartmann number

Hartmann number is defined as the ratio of electromagnetic force to the viscous force. It is denoted by *Ha*. Mathematically,

$$Ha = B^* L \sqrt{\frac{\sigma}{\mu}}, \tag{1.5}$$

where B^* is magnetic induction and σ is Stefan-Boltzman constant.

1.5.6 Wave number

Wave number is defined as the ratio of width of channel to the wavelength of propagating wave along the channel wall. Mathematically

$$\delta = \frac{L}{\lambda^*}, \tag{1.6}$$

where δ is the wave number and λ^* is the wavelength.

1.5.7 Soret and Dufour numbers

The energy flux due to concentration gradient is termed as Dufour effect. Contrary to this mass flux can be created by temperature gradient and referred as Soret effect. These effects

are important when density difference exists in flow regime. The dimensionless numbers characterizing Soret and Dufour effects are Soret and Dufour numbers. Mathematically, it is given by

$$Sr = \frac{D_m K_T (T_0 - T_\infty)}{T_m \nu (C_0 - C_\infty)}, \tag{1.7}$$

$$Du = \frac{D_m K_T (C_0 - C_\infty)}{c_s c_p \upsilon (T_0 - T_\infty)}, \tag{1.8}$$

where D_m is the molecular diffusivity, K_T thermal diffusion ratio, T_m is the mean fluid temperature, c_p is the specific heat at constant pressure, c_s is the concentration susceptibility, T_∞ is the ambient temperature, C_0 is channel concentration and C_∞ is the ambient concentration.

1.5.8 Grashof number

Grashof number is the ratio of natural convection buoyancy force to the viscous force. It is given by

$$Gr = \frac{L^3 g \beta (T_0 - T_1)}{\nu^2}, \tag{1.9}$$

where g is the gravity and β is the bi-viscosity fluid parameter.

1.6 Governing laws for fluid mechanics

To describe the physical behavior of fluid flow, we must have to use some mathematical relations including law of conservation of mass, law of conservation of momentum and law of conservation of energy.

1.6.1 Law of conservation of mass

According to law conservation of mass, the mass of enclosed system always remains constant with passage of time, unless mass is added or removed from the system. The mathematical relation stating this law is called equation of continuity. The vector form of continuity equation for compressible fluid is

$$\frac{\partial \rho}{\partial t} + \nabla.(\rho \mathbf{V}) = 0, \tag{1.10}$$

where *t* is the time. For an incompressible flow above equation takes the form

$$\nabla.\mathbf{V} = 0. \tag{1.11}$$

1.6.2 Law of conservation of momentum

The law of conservation of momentum for an incompressible fluid is given by the equation

$$\rho \frac{d\mathbf{V}}{dt} = \nabla.\boldsymbol{\tau} + \rho \mathbf{F}, \tag{1.12}$$

where τ is Cauchy stress tensor, $\mathbf{F}$ is the body force per unit mass and d/dt is the material derivative.

1.6.3 Law of conservation of energy

The law of conservation of energy is recognized on the first law of thermodynamics. For incompressible fluid energy equation is given by

$$\rho c_p \frac{dT}{dt} = k\nabla^2 T + \mu\Phi. \tag{1.13}$$

1.6.4 Concentration equation

According to Fick's law, the rate of change in concentration with time is directly proportional to the rate at which the concentration gradient changes with distance in a given direction at a constant diffusivity. Mathematically

$$\frac{dC}{dt} = D_m \nabla^2 C + \frac{D_m K_T}{T_m} \nabla^2 T. \tag{1.14}$$

1.6.5 Maxwell's equations

A set of partial differential equations is referred as Maxwell's equations that account for the magnetic and electric field generation as charges/ current fluctuate. These equations are utilized in magnetohydrodynamics and given by

$$\nabla \times \mathbf{B} = \mu_m \mathbf{J} + \mu_0 \frac{\partial \mathbf{E}}{\partial t}, \tag{1.15}$$

$$\nabla \times \mathbf{E} = -\frac{\partial \mathbf{B}}{\partial t}, \tag{1.16}$$

$$\nabla \cdot \mathbf{B} = 0, \tag{1.17}$$

$$\nabla \cdot \mathbf{E} = 0. \tag{1.18}$$

Here, equation (1.15) is mathematical form of Ampere's law and (1.16) is Faraday's law while (1.17) and (1.18) characterizes Gauss laws for magnetic and electric fields, respectively. In above equations **J** is the current density while **B** and **E** are magnetic field and electric field, respectively.

1.6.6 Lorentz force

The Lorentz force is combination of magnetic and electric force arises due to electromagnetic fields on a point charge. Mathematically,

$$\mathbf{F} = \mathbf{J} \times \mathbf{B}, \tag{1.19}$$

where

$$\mathbf{J} = \sigma\left(\mathbf{E} + \mathbf{V} \times \mathbf{B}\right). \tag{1.20}$$

1.7 Fundamental equations in curvilinear coordinates system

In geometry, curvilinear coordinates are coordinates system for Euclidean space in which the coordinate lines may be curved. In curvilinear co-ordinates continuity Eq. (1.10), momentum Eq. (1.12), energy Eq. (1.13) and concentration Eq. (1.14) take the forms:

$$\frac{\partial \rho}{\partial t}+\frac{1}{b_1 b_2 b_3}\left(\frac{\partial}{\partial q_1}\left(b_2 b_3 \rho u_1\right)+\frac{\partial}{\partial q_2}\left(b_3 b_1 \rho u_2\right)+\frac{\partial}{\partial q_3}\left(b_1 b_2 \rho u_3\right)\right)=0, \tag{1.21}$$

$$\begin{aligned}&\rho\left(\frac{\partial u_1}{\partial t}-\frac{u_2}{b_1 b_2}\left(\frac{\partial}{\partial q_1}\left(b_2 u_2\right)-\frac{\partial}{\partial q_2}\left(b_1 u_1\right)\right)+\frac{u_3}{b_1 b_3}\left(\frac{\partial}{\partial q_3}\left(b_1 u_1\right)-\frac{\partial}{\partial q_1}\left(b_3 u_3\right)\right)+\frac{u_1}{b_1}\frac{\partial u_1}{\partial q_1}\right)\\&=\rho k_1+\frac{1}{b_1 b_2 b_3}\left(\frac{\partial}{\partial q_1}\left(b_2 b_3 S_{11}\right)+\frac{\partial}{\partial q_2}\left(b_3 b_1 S_{21}\right)+\frac{\partial}{\partial q_3}\left(b_1 b_2 S_{31}\right)\right)+\frac{S_{21}}{b_1 b_2}\frac{\partial b_1}{\partial q_2}+\frac{S_{31}}{b_1 b_3}\frac{\partial b_1}{\partial q_3}\\&-\frac{S_{22}}{b_1 b_2}\frac{\partial b_2}{\partial q_1}-\frac{S_{33}}{b_1 b_3}\frac{\partial b_3}{\partial q_1},\end{aligned} \tag{1.22}$$

$$\begin{aligned}&\rho\left(\frac{\partial u_2}{\partial t}-\frac{u_3}{b_2 b_3}\left(\frac{\partial}{\partial q_2}\left(b_3 u_3\right)-\frac{\partial}{\partial q_3}\left(b_2 u_2\right)\right)+\frac{u_1}{b_1 b_2}\left(\frac{\partial}{\partial q_1}\left(b_2 u_2\right)-\frac{\partial}{\partial q_2}\left(b_1 u_1\right)\right)+\frac{u_2}{b_2}\frac{\partial u_2}{\partial q_2}\right)\\&=\rho k_2+\frac{1}{b_1 b_2 b_3}\left(\frac{\partial}{\partial q_1}\left(b_2 b_3 S_{12}\right)+\frac{\partial}{\partial q_2}\left(b_3 b_1 S_{22}\right)+\frac{\partial}{\partial q_3}\left(b_1 b_2 S_{32}\right)\right)+\frac{S_{32}}{b_2 b_3}\frac{\partial b_2}{\partial q_3}+\frac{S_{12}}{b_2 b_1}\frac{\partial b_2}{\partial q_1}\\&-\frac{S_{33}}{b_2 b_3}\frac{\partial b_3}{\partial q_2}-\frac{S_{11}}{b_1 b_2}\frac{\partial b_1}{\partial q_2},\end{aligned} \tag{1.23}$$

$$\begin{aligned}&\rho\left(\frac{\partial u_3}{\partial t}-\frac{u_1}{b_1 b_3}\left(\frac{\partial}{\partial q_3}\left(b_1 u_1\right)-\frac{\partial}{\partial q_1}\left(b_3 u_3\right)\right)+\frac{u_2}{b_2 b_3}\left(\frac{\partial}{\partial q_2}\left(b_3 u_3\right)-\frac{\partial}{\partial q_3}\left(b_2 u_2\right)\right)+\frac{u_3}{b_3}\frac{\partial u_3}{\partial q_3}\right)\\&=\rho k_3+\frac{1}{b_1 b_2 b_3}\left(\frac{\partial}{\partial q_1}\left(b_2 b_3 S_{13}\right)+\frac{\partial}{\partial q_2}\left(b_3 b_1 S_{23}\right)+\frac{\partial}{\partial q_3}\left(b_1 b_2 S_{33}\right)\right)+\frac{S_{13}}{b_1 b_3}\frac{\partial b_3}{\partial q_1}+\frac{S_{23}}{b_2 b_3}\frac{\partial b_3}{\partial q_2}\\&-\frac{S_{11}}{b_1 b_3}\frac{\partial b_1}{\partial q_2}-\frac{S_{22}}{b_3 b_2}\frac{\partial b_2}{\partial q_3},\end{aligned} \tag{1.24}$$

$$\begin{aligned}&\rho c_p\left(\frac{\partial T}{\partial t}+\frac{u_1}{b_1}\frac{\partial T}{\partial q_1}+\frac{u_2}{b_2}\frac{\partial T}{\partial q_2}+\frac{u_3}{b_3}\frac{\partial T}{\partial q_3}\right)=\frac{k^*}{b_1 b_2 b_3}\left(\frac{\partial}{\partial q_1}\left(\frac{b_2 b_3}{b_1}\frac{\partial T}{\partial q_1}\right)+\frac{\partial}{\partial q_2}\left(\frac{b_3 b_1}{b_2}\frac{\partial T}{\partial q_2}\right)+\right.\\&\left.\frac{\partial}{\partial q_3}\left(\frac{b_1 b_2}{b_3}\frac{\partial T}{\partial q_3}\right)\right)+\mu\Phi,\end{aligned} \tag{1.25}$$

where

$$\Phi=S_{11}\frac{1}{b_1}\frac{\partial u_1}{\partial q_1}+S_{12}\frac{1}{b_2}\left(\frac{\partial}{\partial q_1}\left(b_2 u_2\right)+\frac{\partial u_1}{\partial q_2}\right)+S_{13}\frac{1}{b_3}\left(\frac{u_1}{q_1}+\frac{1}{b_2}\frac{\partial u_2}{\partial q_2}\right). \tag{1.26}$$

1.8 Literature Review

Due to wide range applications, mathematical modelling of peristaltic movement has received increasing interest among researchers, primarily because of its significance to industrial applications and biological systems. The fundamental work carried out by Latham (1966) and Shapiro (1969) et al. for tube and channel geometry theoretically evaluate the reflux and trapping phenomena related with peristaltic mechanism under long wavelength and low Reynolds number assumptions. The flow was investigated in the wave frame. Peristaltic flow in a circular tube under long wavelength approximation was proposed as a model of intestinal flow by Barton and Raynor (1968). Fung and Yih (1968) adopted an alternative approach based on perturbation technique to analyze the peristaltic flow in the fixed frame (without employing long wavelength and low Reynolds number approximations). A comprehensive review of initial theoretical and experimental work on peristaltic transport was reviewed by Jaffrin and Shapiro (1971). The reflux phenomenon was discussed for several values of Reynolds number. Jaffrin (1973) studied the peristaltic transport and highlight the streamline and inertial curvature effects. Raju and Devanathan (1974) considered the peristaltic motion of a power law fluid in a tube, with a sinusoidal wave of small amplitude travelling down the wall of channel. Gupta and Seshardi (1976) investigated peristaltic flow in non-uniform tube and channel. Poiseuille flow with superimposed peristaltic flow was investigated by Mittra and Parsad (1974) and Srivastava and Srivastava (1985). Numerical study of two-dimensional peristaltic flows was carried out by Brown and Hung (1977), Takabatake and Ayukawa (1982) and Takabatake et al. (1988). Peristaltic pumping of second grade fluid in planar channel and tube was discussed by Siddiqui et al. (1991) and Siddiqui and Schwarz (1994). The influence of peristaltic

flow in a channel for viscous flow was examined by Chu and Fang (2000). Elshehawey and Husseny (2002) studied analytically the peristaltic flow of an incompressible viscous fluid with suction in a channel by using perturbation technique. Peristaltic flows of Johnson-Segalman, third order fluid and Oldroyd-B model were also investigated by Hayat et al (2002; 2003; 2004). Srinivasacharya et al. (2003) investigated the peristaltic transport of micropolar fluid. Mishra and Rao (2003) investigated peristaltic flow in an asymmetric channel. Mekheimer (2003a) comprehensively discussed the peristaltic flow through a porous medium in an inclined planar channel for viscous fluid. Mekheimer (2003b) also studied the transport of magnetohydrodynamic viscous and incompressible peristaltic flow in an inclined planar channel. Hakeem et al. (2004a) observed the separated flow in peristaltic motion of an incompressible Carreau fluid in uniform tube under long wavelength approximation. Hakeem et al. (2004b) studied the effects of endoscope on peristaltic motion under low Reynolds number approximation. Elshahed and Haroun (2005) considered peristaltic transport of magnetically influenced Johnson-Segalman fluid through a flexible channel. Mishra and Rao (2005) studied peristaltic transport in both peripheral and core regions inside a porous channel. Hakeem et al. (2006) examined the peristaltic flow for generalized Newtonian fluid in presence of magnetic field. Elshehawey et al. (2006) used Adomian decomposition method to study the peristaltic transport of an incompressible viscous fluid in an asymmetric channel through a porous medium and found an explicit form of stream function.

The work of Elshehawey was extended by Hayat et al. (2008) by using partial slip condition with the conclusion that trapping is reduced in the presence of surface slip. Hayat et al. (2006) thoroughly studied the peristaltic flow of a Newtonian fluid in a tube. Hayat et al.

(2007) examined peristaltic motion of an incompressible non-Newtonian Burger's fluid in a planar channel for long wavelength case. Haroun (2007b) employed a third-order fluid to discuss peristaltic transport in an asymmetric channel and analyzed the effects of Deborah number and phase difference. Wang et al. (2008) studied magnetohydrodynamic peristaltic motion of a Sisko fluid in a symmetric or asymmetric channel. Ali et al. (2009) considered third grade fluid with peristalsis in a circular cylindrical tube. Pandey and Tripathi (2010) observed the peristaltic transport through a cylindrical tube under the influence of constant magnetic field for a viscous fluid. A variational method for optimizing peristaltic transport in a channel was presented by Walker and Shelley (2010). Ceniceros and Fisher (2013) employed immersed boundary method to study peristaltic flow in a pump for all possible occlusion ratios and Weissenberg number in excess of 100. Böhme and Müller (2013) performed an asymptotic analysis of axisymmetric two-dimensional peristaltic flow to investigate the influence of the aspect ratio, the Weissenberg number, the Deborah number and the wave shape on the pumping characteristics. Shit et al. (2014) studied effects of applied electric field on hydro- magnetic peristaltic flow through a micro-channel. Abbas et al. (2016a) analyzed hyperbolic tangent fluid in a non-uniform channel in the absence of inertial effects. The investigation of magnetohydrodynamics peristaltic blood flow of nanofluid in non-uniform channel is also carried out by Abbas et al. (2016b). More recently, Abbas et al. (2016c) studied peristaltic flow of entropy generation for nanofluids in a varying two-dimensional conduit. Mekheimer (2005; 2008b), Haroun (2007a), Tripathi and Beg (2014a; 2014b), Nabil et al. (2011), Tanveer et al. (2016), also contributed to the literature on peristaltic transport in various scenarios. The principle study of micropolar fluid was presented by Eringen (1964;

2001) to describe the suspensions of neutrally buoyant rigid particles in a viscous fluid. Eringen presented micropolar fluid as an extension of the classical Navier-Stokes theory to include the micro-rotation effects. Ariman et al. (1974) studied application of microcontinum fluid mechanics in a broader prospect. Na and Pop (1997) investigated boundary-layer flow of a micropolar fluid due to a stretching wall. The investigations dealing with peristaltic flow of micropolar fluid were carried out by Srinivasacharya et al. (2003), Hayat et al. (2007), Mekheimer (2008a).

The interaction of heat/ mass transfer with peristaltic flow of Newtonian and non-Newtonian fluids in different geometrical setups has also been reported by various researchers. For instance, Tang and Rankin (1992) investigated the symmetry of the solution of a heat-conducting fluid for peristaltic transport through an elastic tube. Tang and Shen (1993) considered the peristaltic flow of a heated fluid through a cylindrical channel. Radhakrishnamacharya and Murty (1993) considered the peristaltic transport with heat transfer in an asymmetrical channel. Vajravelu et al. (2008) studied peristaltic flow with heat transfer through a porous vertical annulus. Kothandapani and Srinivas (2008) considered hydromagnetic peristaltic flow through a porous medium with heated walls. Nadeem and Akbar (2008) examined the Herschel-Bulkley fluid with peristalsis under the influence of heat transfer in an irregular inclined tube under delta approximation. Srinivas et al. (2011) discussed heat/ mass transfer with peristalsis in an asymmetric channel. Hayat et al. (2010c; 2011b; 2013) considered motivating analysis of heat/ mass transfer phenomena with peristalsis. Shehzad et al. (2014) investigated the effects of thermophoresis on mixed convective nanofluid with peristalsis. Noreen (2017) studied the effect of heat/mass transfer in a non-uniform channel with peristalsis.

In above-mentioned studies the flow is assumed to occur through straight geometry while most of the geometries observed in nature are not straighter one. Generally, fluxes with curved patterns and temperature gradients possess great importance due to instability at comparatively lower values of the governing parameters, so that the transformation to disorder can be studied in a well-organized way. The pioneering work in this direction was analyzed by Sato et al. (2000) for a viscous fluid in a laboratory frame. The analysis of Sato et al. (2000) has been revisited by Ali et al. (2010a) in a wave frame. Ali et al. (2010b) investigated peristaltic flow in a curved channel with heated wall for the first time. In other study Ali et al. (2010c) examined the peristaltic flow through a curved channel for micropolar fluid. Ramanamurthy et al. (2013) considered the peristaltic transport for time-dependent generalized model in a finite length curved channel for laboratory frame of reference. Kalantari et al. (2013) examined numerically the peristaltic flow of Phan-Thien-Tanner non-Newtonian fluid model through a curved channel. Hina et al. (2012; 2013a; 2013b) observed the wall properties in a curved channel with peristalsis in different scenarios. Ali et al. (2015a) considered numerically a bio-rheological fluid having shear-dependent viscosity in a curved channel with peristalsis. Javid et al. (2016) investigated the peristaltic flow through a curved channel for viscoelastic and curvature effects simultaneously. Tanveer et al. (2017) discussed shear-thickening and shear-thinning effects through mixed convective peristaltic flow of Sisko fluid. Several recent studies relating peristaltic flow through curved channel are carried out by Hayat et al. (2011c, 2011d), Ali et al. (2015a, 2016).

Chapter 2

Numerical solution of hydromagnetic peristaltic flow in a porous-saturated heated channel

In this chapter, we analyze the hydromagnetic flow in sinusoidally heated porous channel by utilizing Darcy-Forchiemmer law with joule heating effect. The Darcy's resistance term in the momentum equation is acquired by using modified Darcy's law. The governing equations for flow velocity, temperature and mass concentration are developed under lubrication approximation, commonly known as long wavelength assumption in the realm of peristaltic flows. A well-tested implicit finite difference scheme is employed to solve the set of these equations along with appropriate boundary conditions. The governing equations involve important parameters namely, Forchiemmer parameter, dimensionless radius of curvature, permeability parameter, Hartmann number, Brinkmann number, Schmidt number and Soret number. The effect of these important parameters on velocity, temperature and mass concentration is illustrated through graphs. The pressure-flow rate relationship and streamlines are also shown. The presence of porous matrix inside the channel impedes the flow velocity and reduces the peristaltic transport and mingling. Moreover, temperature of the fluid rises with decreasing permeability of porous-matrix and Hartmann number.

2.1 Mathematical formulation

Consider a curved channel of width *2w* looped in a circle having center *O* and radius $\tilde{R}$. A homogenous Newtonian fluid flows inside the porous-saturated channel due to the sinusoidal deformation of the channel walls. The flow is also subjected to an applied magnetic field in the radial direction. Let *c* be the speed of the waves propagating along the channel walls while *a* and *b* denote the amplitudes of the upper and lower walls of the channel, respectively. Both the walls of passage are conserved at persistent temperature T_0 and T_1, respectively. Similarly, C_0 and C_1 specify the mass concentration at upper and lower walls, respectively. The flow can be well described in a curvilinear coordinate system (R, χ, Z), in which *R* is oriented along radial direction, χ is along the flow direction and *Z* is perpendicular to the plane spanned by *R* and χ. The geometry and coordinate system are illustrated in **Fig. 2.1**.

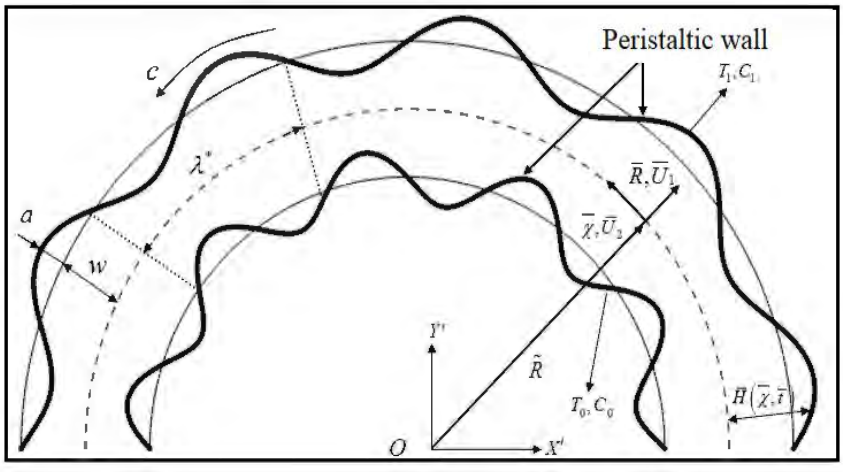

Fig. 2.1: Physical sketch of peristaltic flow scheme.

The shape of both walls is described mathematically as

$$H_1(\chi,t) = \quad w + a\sin\left(\left(\frac{2\pi}{\lambda^*}\right)(\chi - ct)\right), \qquad \text{Upper wall} \tag{2.1}$$

$$H_2(\chi,t) = -w - b\sin\left(\left(\frac{2\pi}{\lambda^*}\right)(\chi - ct)\right). \qquad \text{Lower wall} \tag{2.2}$$

It is intended to determine the flow, temperature and concentration fields. Due to complex nature of transport process in porous medium, the present work is based on simplified mathematical model with the following assumptions:

(1) The medium is homogenous and solid material does not chemically interact with the permeating fluid.

(2) The medium is isotropic.

(3) The fluid is assumed as a continuum.

(4) The fluid is single phase and obeys classical Newtonian constitutive equation. The density of fluid is constant i.e., fluid is incompressible.

(5) No heat source or sink exist in the channel. Moreover, thermal radiation effects are negligible.

(6) The solid matrix is in a local thermal equilibrium with the fluid.

(7) The walls of the channel are non-compliant.

(8) Flow is laminar with negligible gravitational effects.

(9) Effects of induced magnetic field are negligible.

(10) Joule heating and Soret effects are taken into account.

In view of above assumptions the equations governing the flow, heat and mass transfer are given by

$$\nabla \cdot \mathbf{U} = 0, \qquad \textit{(Continuity Equation)} \tag{2.3}$$

$$\rho \frac{d\,\mathbf{U}}{dt} = \nabla . \boldsymbol{\tau} - \frac{\mu}{k^*}\mathbf{U} - \frac{\rho CE}{\sqrt{k^*}}\left|\mathbf{U}\right|\mathbf{U} + \mathbf{J}\times\mathbf{B}, \qquad \textit{(Momentum Equation)} \tag{2.4}$$

$$\rho c_p \frac{dT}{dt} = k\nabla^2 T + \mu\Phi + \frac{\sigma B^{*2}\tilde{R}^2}{\left(R+\tilde{R}\right)^2}U^2, \qquad (\textit{Energy Equation}) \tag{2.5}$$

$$\frac{dC}{dt} = D_m \nabla^2 C + \frac{D_m K_T}{T_m}\nabla^2 T, \qquad (\textit{Mass Concentration Equation}) \tag{2.6}$$

where $\mathbf{U}$ is the velocity, $\boldsymbol{\tau}$ is the Cauchy stress tensor, T is the temperature, CE is a dimensionless form-drag constant, C is the mass concentration and Φ is the dissipation function. The form of the radial magnetic field $\mathbf{B}$ is given by

$$\mathbf{B} = \left(\frac{B^*\tilde{R}}{R+\tilde{R}}\right)\boldsymbol{e_R}. \tag{2.7}$$

In Eq. (2.7), $\boldsymbol{e_R}$ is the unit vector in the radial direction. The Cauchy stress tensor in Eq. (2.4) is given by

$$\boldsymbol{\tau} = -p\mathbf{I} + \mu\mathbf{A_1}, \tag{2.8}$$

where $\mathbf{A}_1$ is defined as

$$\mathbf{A_1} = \nabla\mathbf{V} + \left(\nabla\mathbf{V}\right)^{\Omega}, \tag{2.9}$$

where Ω denote the transpose. Using Eq. (2.7), the term $\mathbf{J}\times\mathbf{B}$ in Eq. (2.4) is given by (Kalantari et al. 2013)

$$\mathbf{J}\times\mathbf{B}=-\left(\frac{\sigma B^{*2}U_2\tilde{R}^2}{\left(R+\tilde{R}\right)^2}\right)\boldsymbol{e}_X, \tag{2.10}$$

where $\boldsymbol{e}_X$ is the azimuthal direction unit vector.

Assuming $\mathbf{U}=\left[U_1(\chi,R,t),U_2(\chi,R,t),0\right]$, $T=T(\chi,R,t)$, $C=C(\chi,R,t)$, (2.11)

Eqs. (2.3) - (2.6) yield

$$\frac{\partial}{\partial R}\left\{\left(R+\tilde{R}\right)U_1\right\}+\tilde{R}\frac{\partial U_2}{\partial\chi}=0, \tag{2.12}$$

$$\frac{\partial U_1}{\partial t}+U_1\frac{\partial U_1}{\partial R}+\frac{RU_2}{R+\tilde{R}}\frac{\partial U_1}{\partial\chi}-\frac{U_2{}^2}{R+\tilde{R}}=-\frac{1}{\rho}\frac{\partial P}{\partial R}+\upsilon\left[\frac{1}{R+\tilde{R}}\frac{\partial}{\partial R}\left\{\left(R+\tilde{R}\right)\frac{\partial U_1}{\partial R}\right\}+\left(\frac{\tilde{R}}{R+\tilde{R}}\right)^2\frac{\partial^2U_1}{\partial\chi^2}-\right.$$

$$\left.\frac{U_1}{\left(R+\tilde{R}\right)^2}-\frac{2\tilde{R}}{\left(R+\tilde{R}\right)^2}\frac{\partial U_2}{\partial\chi}\right]-\frac{\mu}{\rho k^*}U_1-\frac{CE}{\sqrt{k^*}}U_1{}^2, \tag{2.13}$$

$$\frac{\partial U_2}{\partial t}+U_1\frac{\partial U_2}{\partial R}+\frac{\tilde{R}U_2}{R+\tilde{R}}\frac{\partial U_2}{\partial\chi}+\frac{U_2U_1}{R+\tilde{R}}=-\frac{\tilde{R}}{\rho\left(R+\tilde{R}\right)}\frac{\partial P}{\partial\chi}+\nu\left[\frac{1}{\left(R+\tilde{R}\right)}\frac{\partial}{\partial R}\left\{\left(R+\tilde{R}\right)\frac{\partial U_2}{\partial R}\right\}\right.$$

$$\left.+\left(\frac{\tilde{R}}{R+\tilde{R}}\right)^2\frac{\partial^2U_2}{\partial\chi^2}-\frac{U_2}{\left(R+\tilde{R}\right)^2}+\frac{2\tilde{R}}{\left(R+\tilde{R}\right)^2}\frac{\partial U_1}{\partial\chi}\right]-\frac{\mu}{\rho k^*}U_2-\frac{CE}{\sqrt{k^*}}U_2{}^2-\frac{\sigma B^{*2}U_2\tilde{R}^2}{\left(\mathrm{R}+\tilde{R}\right)^2}, \tag{2.14}$$

$$\rho c_p\left[\frac{\partial T}{\partial t}+U_1\frac{\partial T}{\partial R}+\frac{\tilde{R}U_2}{R+\tilde{R}}\frac{\partial T}{\partial\chi}\right]=k\left(\frac{1}{\left(R+\tilde{R}\right)}\frac{\partial}{\partial R}\left\{\left(R+\tilde{R}\right)\frac{\partial T}{\partial R}\right\}+\left(\frac{\tilde{R}}{R+\tilde{R}}\right)^2\frac{\partial^2T}{\partial\chi^2}\right)+\mu\left[2\left(\frac{\partial U_1}{\partial R}\right)^2\right.$$

$$+\left(\frac{\tilde{R}}{R+\tilde{R}}\frac{\partial U_1}{\partial\chi}-\frac{U_2}{R+\tilde{R}}\right)\left(\frac{\partial U_2}{\partial R}+\frac{\tilde{R}}{R+\tilde{R}}\frac{\partial U_1}{\partial\chi}-\frac{U_2}{R+\tilde{R}}\right)+\frac{\partial U_2}{\partial R}\left(\frac{\partial U_2}{\partial R}+\frac{\tilde{R}}{R+\tilde{R}}\frac{\partial U_1}{\partial\chi}-\frac{U_2}{R+\tilde{R}}\right)$$

$$\left.+2\left(\frac{\tilde{R}}{R+\tilde{R}}\frac{\partial U_2}{\partial\chi}+\frac{U_1}{R+\tilde{R}}\right)\right]+\frac{\sigma B^{*2}\tilde{R}^2}{\left(\mathrm{R}+\tilde{R}\right)^2}U_2{}^2, \tag{2.15}$$

$$\left[\frac{\partial C}{\partial t}+U_1\frac{\partial C}{\partial R}+\frac{RU_2}{R+\tilde{R}}\frac{\partial C}{\partial\chi}\right]=D\left(\frac{\partial^2C}{\partial R^2}+\frac{\tilde{R}}{R+\tilde{R}}\frac{\partial C}{\partial R}+\left(\frac{\tilde{R}}{R+\tilde{R}}\right)^2\frac{\partial^2C}{\partial\chi^2}\right)+$$

$$\frac{DK_T}{T_m}\left(\frac{\partial^2T}{\partial R^2}+\frac{\tilde{R}}{R+\tilde{R}}\frac{\partial T}{\partial R}+\left(\frac{\tilde{R}}{R+\tilde{R}}\right)^2\frac{\partial^2T}{\partial\chi^2}\right). \tag{2.16}$$

The above equations are derived from the generalized equations given through Eqs. (1.21) - (1.26) in chapter 1. The scale factors b_1, b_2 and b_3 are such that:

$b_1 = 1,\ b_2 = \left(R + \tilde{R}\right)\Big/\tilde{R}, b_3 = 1.$

The boundary conditions associated with Eqs. (2.12) - (2.16) are (Ali 2010b)

$$U_2 = 0, U_1 = \frac{\partial H_1}{\partial t},\ T = T_0, C = C_0 \text{ at } R=H_1(\chi,t), \tag{2.17}$$

$$U_2 = 0, U_1 = \frac{\partial H_2}{\partial t}, T = T_1, C = C_1 \text{ at } R = H_2(\chi,t). \tag{2.18}$$

We use following transformations to shift from static $\left(R, \chi\right)$ to moving frame $\left(r, x\right)$:

$$x = \chi - ct,\ r = R,\ p = P,\ u_1 = U_1,\ u_2 = U_2 - c, T = T. \tag{2.19}$$

After making use of above transformations, the governing equations are obtained in the wave frame. These equations after defining the dimensionless variables

$$\begin{aligned} &\bar{x} = \frac{2\pi}{\lambda^*} x,\ \eta = \frac{r}{a}, \bar{u}_1 = \frac{u_1}{c}, \bar{u}_2 = \frac{u_2}{c},\ \bar{p} = \frac{2\pi a^2}{\lambda^* \mu c}\, p,\ K^* = \frac{a^2}{k^*}, \\ &\gamma = \frac{\tilde{R}}{a}, \theta = \frac{T - T_1}{T_0 - T_1},\ \phi = \frac{C - C_1}{C_0 - C_1}, \delta = \frac{2\pi a}{\lambda^*}, F_0 = \frac{CE\rho ca}{\mu}, \end{aligned} \tag{2.20}$$

and invoking long wavelength ($\delta \approx 0$) reduces to

$$\frac{\partial p}{\partial \eta} = 0, \tag{2.21}$$

$$\begin{aligned} &-\frac{\partial p}{\partial x} + \frac{1}{\gamma}\left(-\frac{\partial}{\partial \eta}\left\{(\eta+\gamma)\frac{\partial^2 \psi}{\partial \eta^2}\right\} - \frac{1}{\eta+\gamma}\left(1 - \frac{\partial \psi}{\partial \eta}\right)\right) - \frac{\eta+\gamma}{K^*\gamma}\left(1 - \frac{\partial \psi}{\partial \eta}\right) \\ &-\frac{\mathrm{Re}(\eta+\gamma)F_0}{\gamma\sqrt{K^*}}\left(1 - \frac{\partial \psi}{\partial \eta}\right)^2 - \frac{\gamma Ha^2}{\eta+\gamma}\left(1 - \frac{\partial \psi}{\partial \eta}\right) = 0, \end{aligned} \tag{2.22}$$

$$\frac{\partial^2 \theta}{\partial \eta^2} + \frac{1}{(\eta+\gamma)}\frac{\partial \theta}{\partial \eta} + Br\left(-\frac{1}{\eta+\gamma}\left(1 - \frac{\partial \psi}{\partial \eta}\right) - \frac{\partial^2 \psi}{\partial \eta^2}\right)^2 + \frac{BrHa^2\gamma^2}{(\eta+\gamma)^2}\left(1 - \frac{\partial \psi}{\partial \eta}\right)^2 = 0, \tag{2.23}$$

$$\left(\frac{\partial^2\phi}{\partial\eta^2}+\frac{1}{(\gamma+\eta)}\frac{\partial\phi}{\partial\eta}\right)=-SrSc\left(\frac{\partial^2\theta}{\partial\eta^2}+\frac{1}{(\gamma+\eta)}\frac{\partial\theta}{\partial\eta}\right). \tag{2.24}$$

In above equations δ, γ, Re, F_0 and K^* represent the wave number, the dimensionless radius of curvature, the Reynolds number, Forchiemmer parameter and dimensionless permeability parameter, respectively. The stream function ψ and velocity components u_1 and u_2 are related through the expressions

$$u_1=\delta\frac{\gamma}{\eta+\gamma}\frac{\partial\psi}{\partial x},\quad u_2=-\frac{\partial\psi}{\partial\eta}. \tag{2.25}$$

Solution of Eqs. (2.21) and (2.22) yield

$$\frac{\partial}{\partial\eta}\left[\frac{1}{\gamma}\left(-\frac{\partial}{\partial\eta}\left\{(\eta+\gamma)\frac{\partial^2\psi}{\partial\eta^2}\right\}-\frac{1}{\eta+\gamma}\left(1-\frac{\partial\psi}{\partial\eta}\right)\right)-\frac{\eta+\gamma}{K^*\gamma}\left(1-\frac{\partial\psi}{\partial\eta}\right)-\frac{\mathrm{Re}(\eta+\gamma)F_0}{\gamma\sqrt{K^*}}\left(1-\frac{\partial\psi}{\partial\eta}\right)^2 -\frac{\gamma Ha^2}{\eta+\gamma}\left(1-\frac{\partial\psi}{\partial\eta}\right)\right]=0. \tag{2.26}$$

The boundary conditions (2.17) and (2.18) transform to

$$\psi=-\frac{q}{2},\ \frac{\partial\psi}{\partial\eta}=1,\ \theta=0,\ \phi=0,\ \text{at}\ \ \eta=h_1=1+\lambda\sin x, \tag{2.27}$$

$$\psi=\frac{q}{2},\ \frac{\partial\psi}{\partial\eta}=1,\ \theta=1,\ \phi=1,\ \text{at}\ \ \eta=h_2=-1-\lambda'\sin x, \tag{2.28}$$

where $\lambda=a/w$ and $\lambda'=b/w$ are the amplitude ratios. In summary, we have to solve Eqs. (2.23), (2.24) and (2.26) subject to boundary conditions (2.27) and (2.28). The physical quantities of interest are given by (Chu 1996)

$$F_u = \int_0^{2\pi} -h_1 \frac{dp}{dx} dx,\ F_l = \int_0^{2\pi} -h_2 \frac{dp}{dx} dx, \qquad \text{(Frictional forces)} \qquad (2.29)$$

$$\Delta p = \int_0^{2\pi} \frac{dp}{dx} dx, \qquad \text{(Pressure rise per wavelength)} \qquad (2.30)$$

$$z_i = \frac{\partial h_i}{\partial x} \frac{\partial \theta}{\partial \eta}\bigg|_{\eta = h_i}, \ i = 1, 2. \qquad \text{(Heat transfer coefficients)} \qquad (2.31)$$

$$Sh = \frac{\partial h_i}{\partial x} \frac{\partial \phi}{\partial \eta}\bigg|_{\eta = h_i}. \ i = 1, 2. \qquad \text{(Sherwood number)} \qquad (2.32)$$

Now, in order to solve Eqs. (2.23), (2.24) and (2.26) subject to boundary conditions given by Eqs. (2.27) and (2.28), an implicit finite difference technique is employed for the solution.

2.2 Method of solution

In this procedure the nonlinear BVP is transformed into linear form at the $(m+1)$th reiteration step. Following reiteration process is adopted for the above specific problem:

$$\frac{\partial^4 \psi^{(m+1)}}{\partial \eta^4} + \frac{\partial^3 \psi^{(m+1)}}{\partial \eta^3} - \left\{ \frac{1}{\eta+\gamma} + \frac{\eta+\gamma}{K^*} + \frac{2\,\mathrm{Re}(\eta+\gamma)F_0}{\sqrt{K^*}} \left(1 - \frac{\partial \psi^{(m)}}{\partial \eta}\right) + \frac{\gamma^2 Ha^2}{\eta+\gamma} \right\} \frac{\partial^2 \psi^{(m+1)}}{\partial \eta^2} -$$
$$\left\{ -\frac{1}{(\eta+\gamma)^2} + \frac{1}{K^*} + \frac{\mathrm{Re}\,F_0}{\sqrt{K^*}} \left(\frac{\partial \psi^{(m)}}{\partial \eta} - 2 \right) - \frac{\gamma^2 Ha^2}{(\eta+\gamma)^2} \right\} \frac{\partial \psi^{(m+1)}}{\partial \eta} - \frac{1}{(\eta+\gamma)^2} + \frac{1}{K^*} + \qquad (2.33)$$
$$\frac{\mathrm{Re}\,F_0}{\sqrt{K^*}} - \frac{\gamma^2 Ha^2}{(\eta+\gamma)^2} = 0,$$

$$\frac{\partial^2 \theta^{(m+1)}}{\partial \eta^2} + \frac{1}{\eta+\gamma} \frac{\partial \theta^{(m+1)}}{\partial \eta} = -Br \left(-\frac{1}{\eta+\gamma} \left(1 - \frac{\partial \psi^{(m)}}{\partial \eta} \right) - \frac{\partial^2 \psi^{(m)}}{\partial \eta^2} \right)^2 - \frac{BrHa^2\gamma^2}{(\eta+\gamma)^2} \left(1 - \frac{\partial \psi^{(m)}}{\partial \eta} \right)^2, \qquad (2.34)$$

$$\frac{\partial^2 \phi^{(m+1)}}{\partial \eta^2} + \frac{1}{\eta+\gamma}\frac{\partial \phi^{(m+1)}}{\partial \eta} = -SrSc\left(\frac{\partial^2 \theta^{(m)}}{\partial \eta^2} + \frac{1}{(\eta+\gamma)}\frac{\partial \theta^{(m)}}{\partial \eta}\right), \tag{2.35}$$

$$\psi^{m+1} = -\frac{q}{2}, \frac{\partial \psi^{m+1}}{\partial \eta} = 1,\ \theta^{(m+1)} = 0,\ \phi^{(m+1)} = 0, \text{ at } \eta = h_1, \tag{2.36}$$

$$\psi^{(m+1)} = \frac{q}{2},\ \frac{\partial \psi^{(m+1)}}{\partial \eta} = 1, \theta^{(m+1)} = 1,\ \phi^{(m+1)} = 1, \text{ at } \eta = h_2, \tag{2.37}$$

where the index (*m*) shows the iterative step.

In the next step, we insert finite difference approximations of $\psi^{(m+1)}$, $\theta^{(m+1)}$, $\phi^{(m+1)}$ and their derivatives into Eqs. 2.33-2.35. In this way, we get a system of linear algebraic equations at each iterative step. These algebraic equations are solved at each cross-section to get numerical results of $\psi^{(m+1)}$, $\theta^{(m+1)}$ and $\phi^{(m+1)}$. It is important to note that, suitable initial guesses are required for $\psi^{(m)}$, $\theta^{(m)}$ and $\phi^{(m)}$ at every cross-section to start the reiteration way. For present computation, linear initial guesses (only satisfying the Dirichlet boundary conditions) are used. The iterative procedure at each cross-section is carried out until a convergent solution is reached. The convergent solution is obtained rapidly by sequential under-relaxation scheme. In this scheme the values of $\tilde{\psi}^{(m+1)}$, $\tilde{\theta}^{(m+1)}$ and $\tilde{\phi}^{(m+1)}$ at (*m+1*) th iterative step are used to define convergent values $\psi^{(m+1)}$, $\theta^{(m+1)}$ and $\phi^{(m+1)}$ at the same step as follows:

$$\psi^{(m+1)} = \psi^{(m)} + \tau'(\tilde{\psi}^{(m+1)} - \psi^{(m)}),$$
$$\theta^{(m+1)} = \theta^{(m)} + \tau'(\tilde{\theta}^{(m+1)} - \theta^{(m)}),$$
$$\phi^{(m+1)} = \phi^{(m)} + \tau'(\tilde{\phi}^{(m+1)} - \phi^{(m)}),$$

where τ' is under relaxation parameter usually assumed small. In present computation the iterative procedure is terminated after achieving the values of ψ, θ and ϕ convergent to 10^{-8}.

2.3 Algorithm validation

Before embarking on the physical interpretation of the obtained results it is better to validate our results by comparing them with the existing results in the literature. To this end, we have prepared **Figs. 2.2** and **2.3**. **Fig. 2.2** presents a comparison of velocity profile $u_2(\eta)$ computed using present numerical scheme for $K^* \to \infty, Ha = 0, \gamma = 2, \lambda = 0.4,$ $x = 0, \theta = 1$ (solid line) with the velocity profile given in **Fig. 2.3** of reference (Ali et al. 2010a) corresponding to $k = 2, \phi = 0.4, x = 0, \theta = 1$ (superimposed dots). Clearly, both curves coincide showing an excellent agreement between our results with the existing ones. **Fig. 2.3** shows a comparison of temperature profile $\theta(\eta)$ based on our numerical scheme for $\lambda = 0.4, x = 0, \gamma = 2$ and $\Theta = 1,$ (solid line) with the temperature profile in Fig. 4 of reference (Ali et al. 2010b) corresponding to $\Theta = 1, \phi = 0.4, x = 0, k = 2,$ (superimposed dots). Again, an excellent correlation is achieved which clearly testifies validity of our numerical results.

2.4 Computational results and their interpretation

In this section, we interpret the graphical results provided in **Figs. 2.4 - 2.28** to analyze flow and pumping characteristics, temperature distribution, mass concentration and trapping problem for various values of parameters like curvature parameter (γ), Forchiemmer parameter (F_0), Brinkman number (Br) and permeability parameter (K^*). The variation of friction forces and heat and mass transfer coefficients at both upper and lower walls is also shown.

The axial velocity distribution for some specific values of Forchiemmer parameter (F_0), permeability parameter (K^*), Hartmann number (*Ha*) and curvature parameter (γ), is shown in **Figs. 2.4 - 2.7**, respectively. **Fig. 2.4** shows that axial velocity is suppressed with increasing Forchiemmer parameter. The velocity profile becomes asymmetric with maximum appearing below the curve $\eta = 0.$ The Forchiemmer parameter (F_0) is the ratio of solid-liquid interaction of viscous resistance. Larger values of F_0 correspond to the situation when viscous resistance is smaller in comparison to resistance due to the solid obstacles. Therefore the suppression of velocity amplitude observed in **Fig. 2.4** for larger values of F_0 is attributed to the increase in resistance due to the solid obstacles. **Fig. 2.5** shows the effects of permeability parameter (K^*) on velocity $(u_2(\eta))$. Smaller values of K^* correspond to weaker porous medium effects while larger values represent the case when resistance due to porous matrix is strong. It is noticed that increasing values of K^* impede flow velocity amplitude and shift the maximum velocity away from the lower wall

of the channel towards the central line ($\eta = 0$). **Fig. 2.6** demonstrates the effects *Ha* on the flow velocity. Here it is quite obvious that flow velocity shows boundary layer behavior for larger values of *Ha*. In fact for large values of *Ha*, the disturbance in flow velocity is restrained in thin layer near both upper and lower walls. It is further noted from **Fig. 2.6** that the axial velocity for moderate values of Hartmann number recaptures its symmetric profile. The boundary layer behavior revealed by the flow velocity is due to resistive nature of magnetic force. This resistance due to magnetic force suppresses the flow in the vicinity of the channel center. In order to maintain the prescribed mass flux, the velocity near the boundary walls will rise. The simultaneous occurrence of both these phenomena leads to the function of boundary layer at the channel walls. **Fig. 2.7** depicts the effects of dimensionless radius of curvature (γ) on velocity distribution. For smaller values of γ the velocity is asymmetric about $\eta = 0$ with maximum appearing in the lower half of the channel. The asymmetry in flow velocity is due to the pressure accelerated fluid layers near lower wall of channel due to curvature. With increasing γ, the velocity regains its symmetry about $\eta = 0$. This is expected because for large values of γ channel becomes straight.

Figs 2.8 - 2.11 demonstrate the effect of different parameters on pressure rise per wavelength. **Fig 2.8** depicts the effects of Forchiemmer parameter on Δp. No peristaltic pumping region can be identified from this figure. The maximum pressure rise (i.e., Δp corresponding to $\Theta = 0$) is zero against which peristalsis has to work. This clearly indicate that for suitable choice of involved parameters the resistance offered by pressure gradient to peristaltic flow can be avoided. The profile of pressure rise per wavelength for K^*

(permeability parameter) is shown in **Fig. 2.9**. Here, it is noted that in peristaltic pumping region $(\Theta > 0, \Delta p > 0)$ Δp increases with decreasing K^* for a fixed value of prescribed flow rate. Thus, in the present settings the porous medium inside the channel hampers the normal flow of the fluid and peristalsis has to do greater work against Δp to maintain the same flux as in the case of clear medium inside the channel. This eventually reduces the pumping efficiency. **Figs. 2.10** and **2.11** demonstrate effect of Δp on flow rate Θ for different values of *Ha* and γ, respectively. In pumping region Δp rises, by mounting *Ha*. It is observed that as Hartmann number increases, the value of pressure rise per wavelength decreases. **Fig. 2.11** shows that below a particular critical value of Θ, Δp decreases as we shift from curved to straight channel in pumping region. An opposite trend is noticed above this particular value. This opposite trend is also observed in free pumping and co-pumping regions.

The friction forces at upper and lower walls denoted by F_u and F_l, respectively for various values of Forchiemmer parameter $\left(F_0\right)$, permeability parameter $\left(K^*\right)$ and Hartman number (*Ha*) are shown in **Figs. 2.12 - 2.14.** It is observed that the behavior of friction forces is opposite to that of pressure rise. Moreover, they resist the flow in the pumping region and magnitude of resistance increases with increasing permeability parameter and Hartmann number. However, the resistance due to friction forces in pumping region decreases with increasing Forchiemmer parameter. Further, resistance at lower wall is greater than at upper wall.

The radial distribution of temperature of the fluid present in the channel for different values of Brinkmann number (*Br*), permeability parameter $\left(K^*\right)$, Hartman number (*Ha*) and

Forchiemmer parameter (F_0) is shown in **Figs. 2.15 - 2.18**. Here it is noted that the effect of *Br*, K^* and *Ha* is to increase the fluid temperature inside the channel while the effect of F_0 is quite opposite. It is observed that an increase in Forchiemmer parameter impedes the fluid motion only in the vicinity of the channel while remaining cross-section is unaffected with change in F_0. Due to this reason the heat transfer rate from boundaries to the fluid is reduced and the fluid temperature is decreased inside the channel with increasing Forchiemmer parameter.

The variations of *z* at both walls for various values of F_0, *Ha* and *Br* are shown through **Fig. 2.19**. The profiles of *z* are clearly oscillating (periodic) due to periodic oscillating nature of the boundary walls. The amplitude of oscillation increases with increasing F_0, *Ha* and *Br*.

The profiles of mass concentration inside the channel with several values of Br, K^*, Ha and F_0 are shown in **Figs. 2.20 - 2.23**. It is observed that the behavior of mass concentration is similar to behavior of temperature i.e. mass concentration inside the channel increases with increasing Br, K^* and *Ha* while its magnitude reduces with increasing F_0. The effects of Forchiemmer parameter (F_0), Hartmann number (*Ha*) and Brinkmann number (*Br*) on Sherwood number at both walls are shown through **Fig. 2.24**. It is observed that Sherwood number also exhibits oscillatory behavior and its amplitude at both walls increases with increasing F_0 and *Br*. In contrast, the amplitude at lower wall (upper wall) decreases (increasing) with large values of *Ha*.

The streamline of flow inside the channel for different values of F_0 (Forchiemmer parameter), K^* (permeability parameter), *Ha* (Hartman number) and γ (curvature parameter) are shown in **Figs. 2.25 - 2.28**. These plots demonstrate trapping phenomenon in which a quantity of the fluid called bolus is trapped within closed streamlines. It is observed through **Fig. 2.25** that bolus is not significantly affected with an increase in Forchiemmer parameter. However, the bolus gets shrinked and center of circulation shift from lower to upper half with increasing K^* as shown in **Fig. 2.26**. Figure **2.27** shows the effects of Hartmann number on streamlines. Here it is noted that mingling bolus concerted in upper part of channel for *Ha = 0.5* transforms to the bolus whose center of rotation lies in the lower half of the channel with increasing *Ha* to *3.5*. In the process of transformation the size of the bolus is also reduced. **Fig. 2.28** shows that the bolus is asymmetric and concerted in upper part of channel for smaller values of γ i.e. in a curved channel. However, it regains its symmetry when $\gamma \to \infty$ i.e. when channel becomes straight.

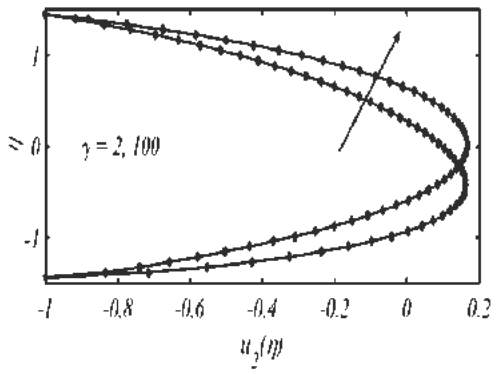

Fig. 2.2: Comparison of present results for velocity (solid line) with the results for velocity reported in ref. (Ali et al. 2010) (superimposed line).

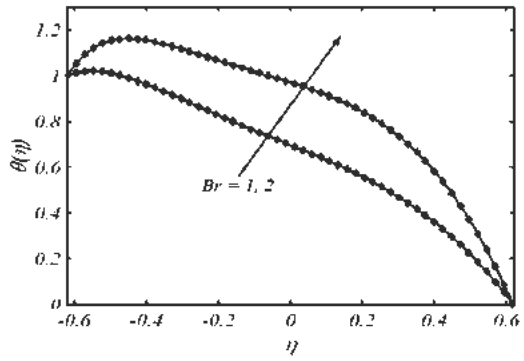

Fig. 2.3: Comparison of present results for temperature (solid line) with the results for temperature reported in ref. (Ali et al. 2010) (superimposed line).

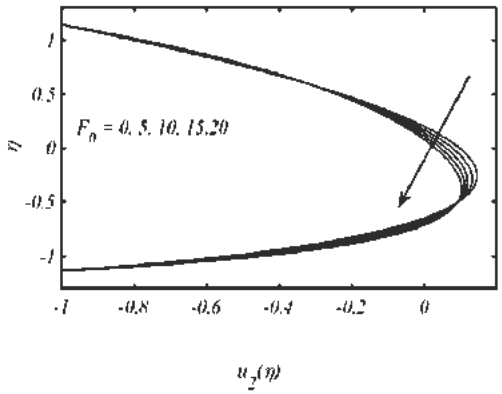

Fig. 2.4: Influence of F_0 on velocity $u_2(\eta)$ for γ =1.5, K^*=2, Ha = 0.5, $\lambda = 0.4$ and $\Theta = 1.2.$

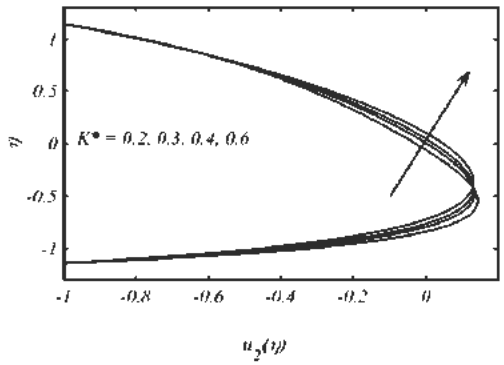

Fig. 2.5: Influence of K^* on velocity $u_2(\eta)$ for γ = 1.5, F_0 =2, Ha = 0.5, $\lambda = 0.4$, and $\Theta = 1.2.$

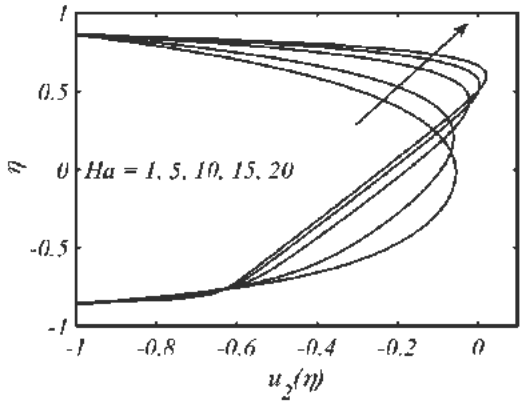

Fig. 2.6: Effect of *Ha* on velocity $u_2(\eta)$ for γ = 1.5, F_0 =2, K^* = 0.2, $\lambda = 0.4$, and $\Theta = 1.2$.

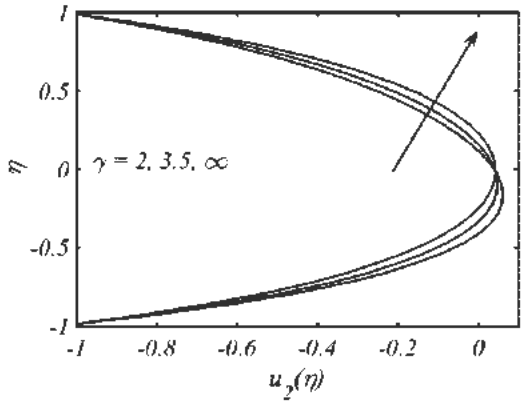

Fig. 2.7: Effect of γ on velocity $u_2(\eta)$ for K^* = 0.2, F_0 =2, *Ha* = 0.2, $\lambda = 0.4$, and $\Theta = 1.2$.

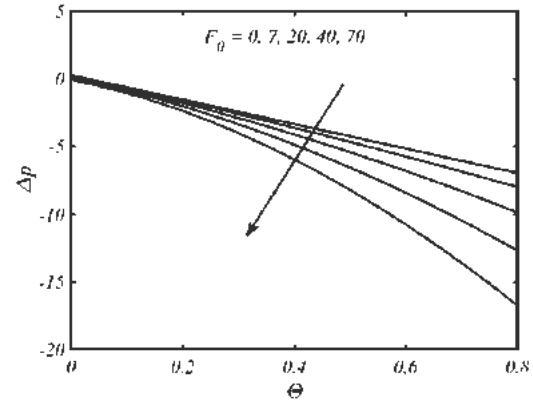

Fig. 2.8: Effects of F_0 on pressure rise per wavelength for γ =2, K^* = 2, *Ha* = 0.5 and $\lambda = 0.4$.

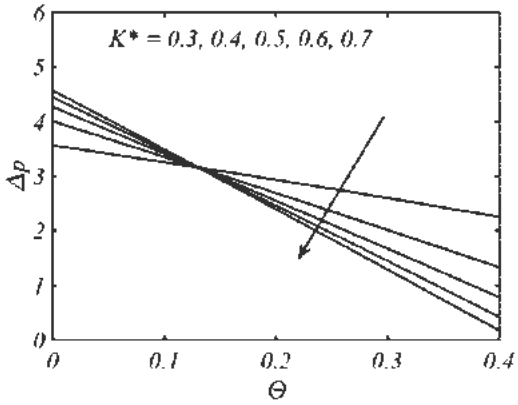

Fig. 2.9: Effect of K^* on pressure rise per wavelength for γ =2, F_0 = 2, *Ha* = 0.5 and $\lambda = 0.4$.

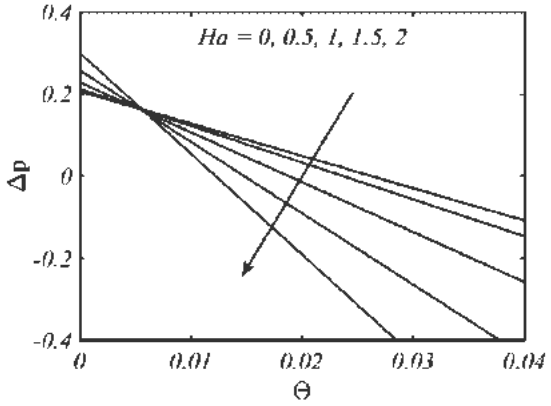

Fig. 2.10: Effect of *Ha* on pressure rise per wavelength for γ =2, K^* = 2, F_0 = 2 and $\lambda = 0.4$.

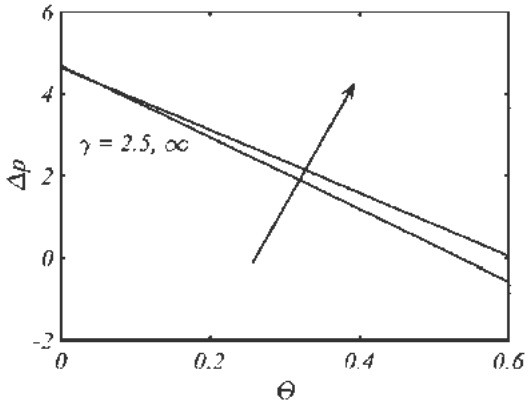

Fig. 2.11: Effect of γ on pressure rise per wavelength for *Ha* = 0.2, K^* = 0.5, γ =2 and $\lambda = 0.4$.

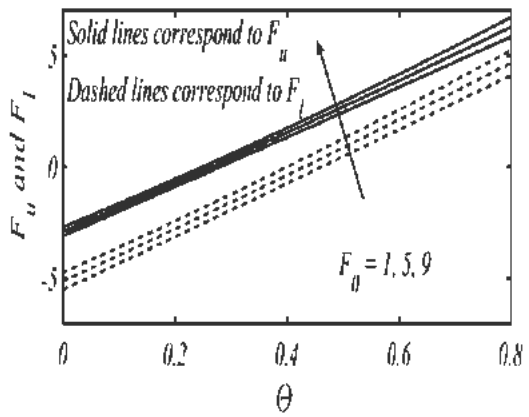

Fig. 2.12: Friction forces at upper and lower walls for F_0 using *Ha* = 0.2, γ =2 and $\lambda = 0.4$.

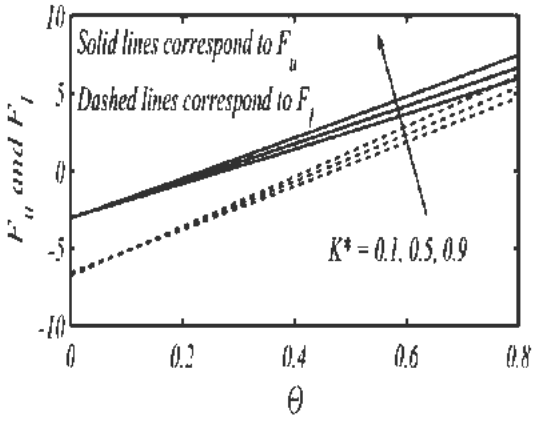

Fig. 2.13: Friction forces at upper and lower walls for K^* using F_0 = 2, γ =2 and $\lambda = 0.4$.

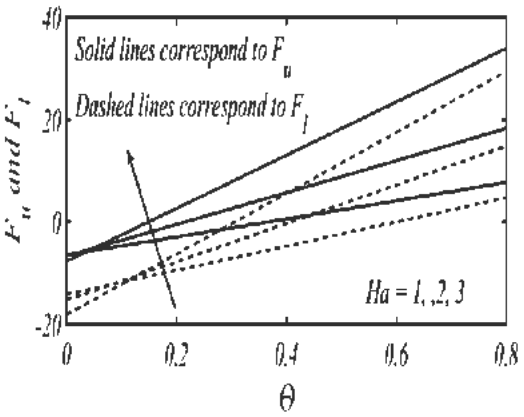

Fig. 2.14: Friction forces at upper and lower walls for *Ha* using $F_0 = 2$, γ =2 and $\lambda = 0.4$.

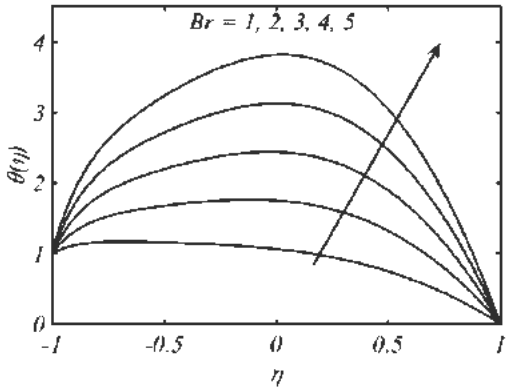

Fig. 2.15: Effect of temperature $\theta(\eta)$ for *Br* using $F_0 = 2, \lambda = 0.4$, $\gamma = 2$ and $\Theta = 1.2$.

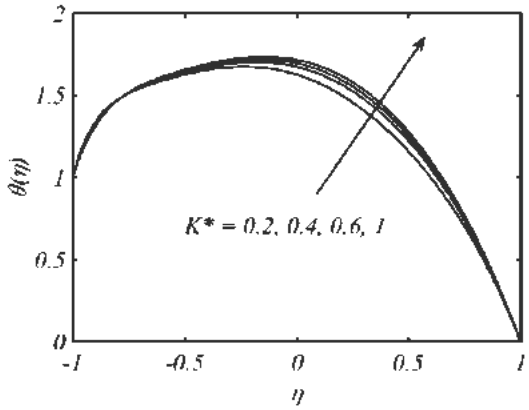

Fig. 2.16: Effect of K^* on temperature $\theta(\eta)$ for $F_0 = 2, Br = 2, \lambda = 0.4, \gamma = 2$ and $\Theta = 1.2$.

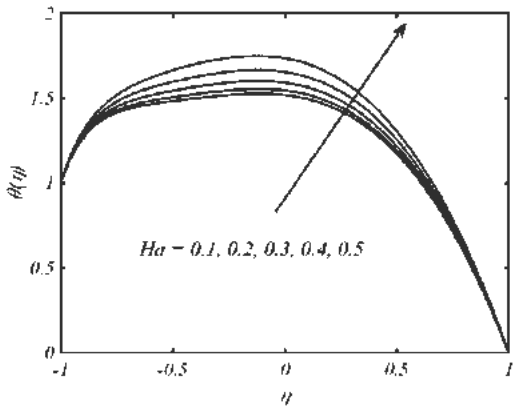

Fig. 2.17: Effect of *Ha* on temperature $\theta(\eta)$ for $F_0 = 2, Br = 2, \lambda = 0.4, \gamma = 2$ and $\Theta = 1.2$.

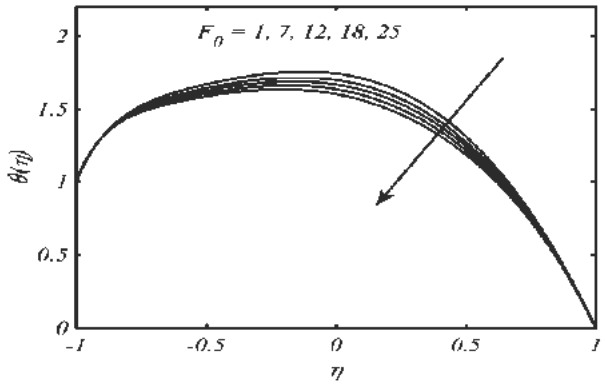

Fig. 2.18: Effect of F_0 on temperature $\theta(\eta)$ for $Br = 2$, $\lambda = 0.4$, $\gamma = 2$ and $\Theta = 1.2$.

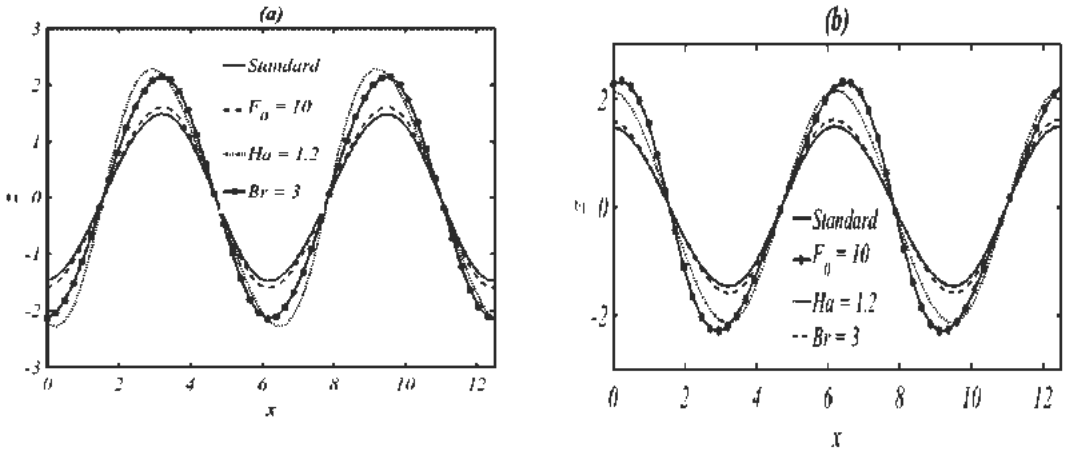

Fig. 2.19: Variation of *z* at upper (a) and lower (b) walls for different parameters with $\Theta = 1.2$ $\lambda = 0.4$ and $\gamma = 2$.

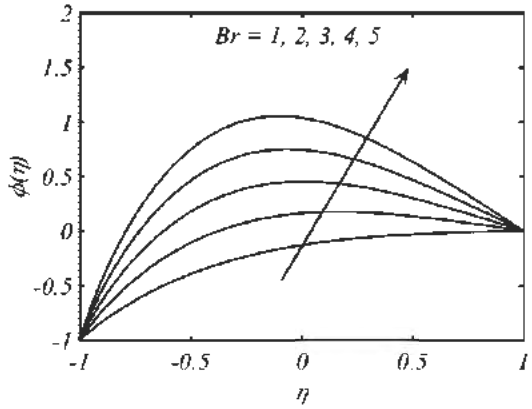

Fig. 2.20: Effect of *Br* on concentration $\phi(\eta)$ for *Ha* = 1, *Sr* = 0.5, *Sc* = 0.2, $\lambda = 0.4$ and $\gamma = 2.$

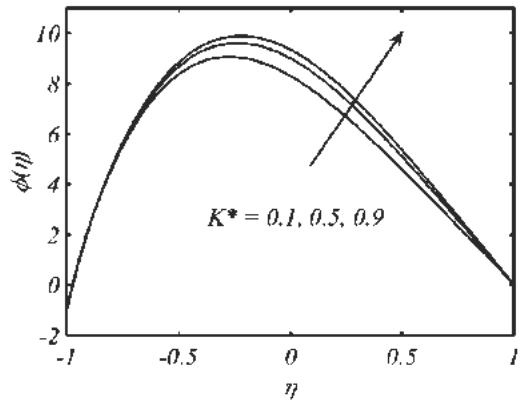

Fig. 2.21: Effect of K^* on concentration $\phi(\eta)$ for *Br* =2, *Sr* = 0.5, *Sc* = 0, $\lambda = 0.4$ and $\gamma = 2.$

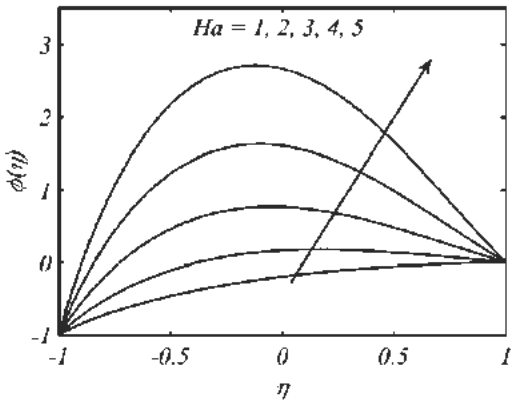

Fig. 2.22: Effect of *Ha* on concentration $\phi(\eta)$ for *Br* = 2, *Sr* = 0.5, *Sc* = 0.2, K^* =0.5, $\lambda = 0.4$ and $\gamma = 2.$

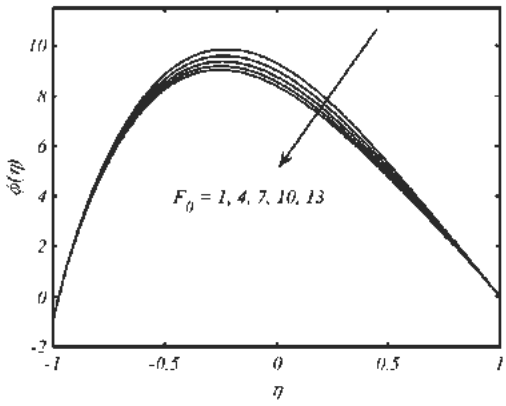

Fig. 2.23: Effect of F_0 on concentration $\phi(\eta)$ for *Br* = 2, K^* =0.5, *Sr* = 1.5, *Sc* = 1.2, $\lambda = 0.4$ and $\gamma = 2.$

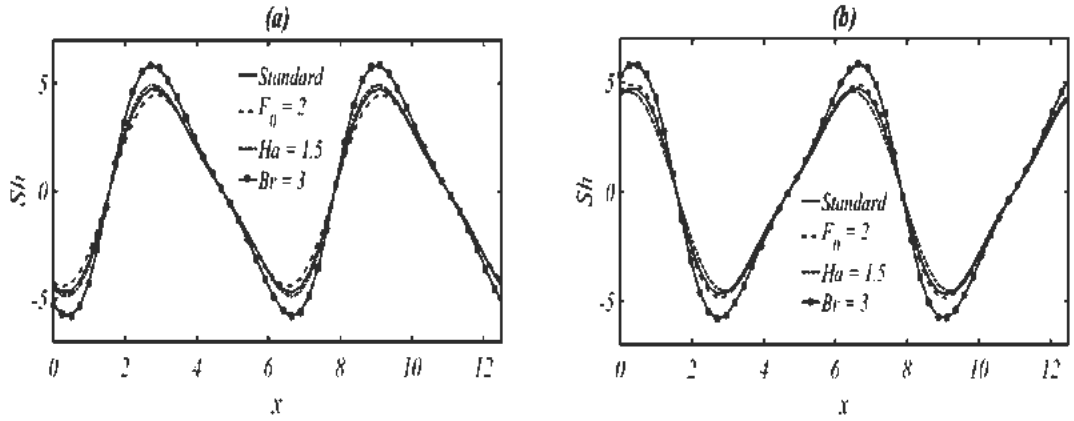

Fig. 2.24: Variation of Sherwood number *Sh* at upper (a) and lower (b) walls for different parameters with $\Theta = 1.5,\ \lambda = 0.4$ and $\gamma = 2.$

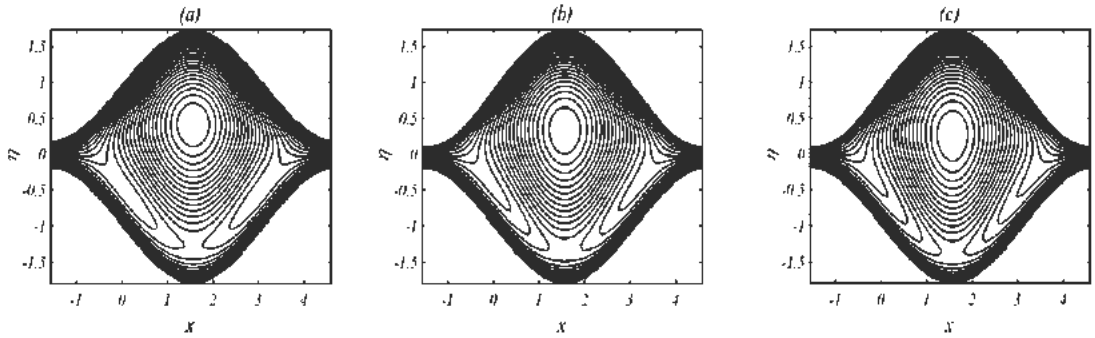

Fig. 2.25: Flow patterns for (a) $F_0 = 1,$ (b) $F_0 = 5,$ and (c) $F_0 = 10,$ with $\gamma = 2$ $K^* = 2$ and $\lambda = 0.8.$

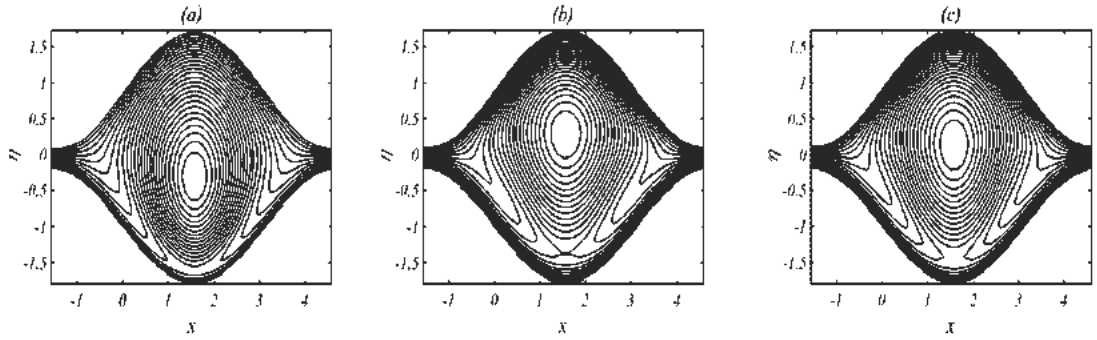

Fig. 2.26: Flow patterns for (a) $K^* = 0.1$, (b) $K^* = 0.5$ and (c) $K^* = 1$, using $\gamma = 2$ and $\lambda = 0.8$.

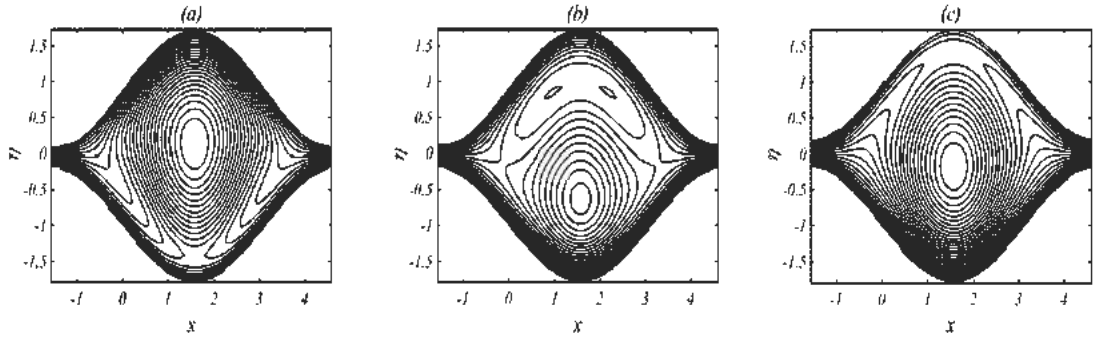

Fig. 2.27: Flow patterns for (a) *Ha* = 0.5, (b) *Ha* = 2.5 and (c) *Ha* =3.5, with F_0 = 1.5, $\gamma = 2$, and $\lambda = 0.8$.

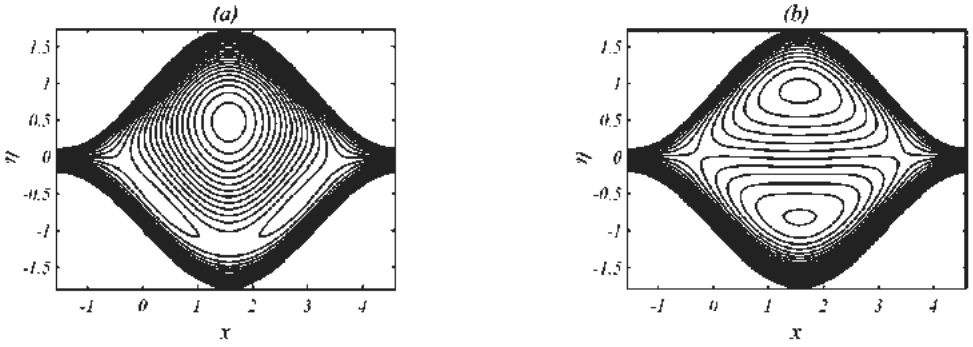

Fig. 2.28: Flow patterns for (a) $\gamma = 3$ and (b) $\gamma \to \infty$, with F_0 = 1.5, *Ha* = 0.5, $K^* = 0.5$ and $\lambda = 0.8$.

Chapter 3

Mixed convective hydromagnetic peristaltic flow in a curved channel with Joule heating effect

In this chapter, we investigate the flow, heat and mass transfer characteristics in peristaltic motion through a curved channel in the presence of mixed convection. The coupling between momentum and energy equation is attained using Boussinesq approximation. The equations describing the flow and heat/ mass transfer are developed using curvilinear coordinates. A reduction of these equations is made based on delta approximation. The reduced linear ordinary differential equations are integrated numerically using an implicit finite difference scheme. The effects of thermal and concentration Grashof numbers, Hartmann number, Brinkmann number and curvature parameter on longitudinal velocity, pressure rise, temperature and mass concentration are analyzed in detail. The flow patterns in the channel illustrating the effects of Grashof numbers, Brinkmann number and Hartmann number are also displayed.

3.1 Mathematical Modeling

The geometric scheme for this problem is similar as described in chapter 2 section 2.1. Similarly the fluid mentioned here is also same as described in previous chapter. However, due to consideration of buoyancy force (arising due to gravity, as shown in **Fig 3.1**) the momentum equations is modified as given below

$$\rho\frac{d\,\mathbf{U}}{dt}=\nabla.\boldsymbol{\tau}-\rho\mathbf{g}\beta_T(T-T_0)-\rho\mathbf{g}\beta_C(C-C_0)+\mathbf{J}\times\mathbf{B}, \tag{3.1}$$

where β_T and β_C thermal and concentration expansion coefficients, respectively. The continuity, energy and concentration equations are same as given by Eqs. (2.3), (2.5) and (2.6), respectively. For two-dimensional velocity field given by Eq. (2.9), Eq. (3.1) yields:

$$\frac{\partial U_1}{\partial t}+U_1\frac{\partial U_1}{\partial R}+\frac{RU_2}{R+\tilde{R}}\frac{\partial U_1}{\partial \chi}-\frac{{U_2}^2}{R+\tilde{R}}=-\frac{1}{\rho}\frac{\partial P}{\partial R}+\upsilon\left[\frac{1}{R+\tilde{R}}\frac{\partial}{\partial R}\left\{\left(R+\tilde{R}\right)\frac{\partial U_1}{\partial R}\right\}+\left(\frac{\tilde{R}}{R+\tilde{R}}\right)^2\frac{\partial^2 U_1}{\partial \chi^2}-\right.$$

$$\left.\frac{U_1}{\left(R+\tilde{R}\right)^2}-\frac{2\tilde{R}}{\left(R+\tilde{R}\right)^2}\frac{\partial U_2}{\partial \chi}\right], \tag{3.2}$$

$$\frac{\partial U_2}{\partial t}+U_1\frac{\partial U_2}{\partial R}+\frac{\tilde{R}U_2}{R+\tilde{R}}\frac{\partial U_2}{\partial \chi}+\frac{U_2U_1}{R+\tilde{R}}=-\frac{\tilde{R}}{\rho\left(R+\tilde{R}\right)}\frac{\partial P}{\partial \chi}+\nu\left[\frac{1}{\left(R+\tilde{R}\right)}\frac{\partial}{\partial R}\left\{\left(R+\tilde{R}\right)\frac{\partial U_2}{\partial R}\right\}+\left(\frac{\tilde{R}}{R+\tilde{R}}\right)^2\frac{\partial^2 U_2}{\partial \chi^2}\right.$$

$$\left.-\frac{U_2}{\left(R+\tilde{R}\right)^2}+\frac{2\tilde{R}}{\left(R+\tilde{R}\right)^2}\frac{\partial U_1}{\partial \chi}\right]-\rho g\beta_T(T-T_0)-\rho g\beta_C(C-C_0)-\frac{\sigma B^{*2}\tilde{R}^2U_2}{\left(\mathrm{R}+\tilde{R}\right)^2}. \tag{3.3}$$

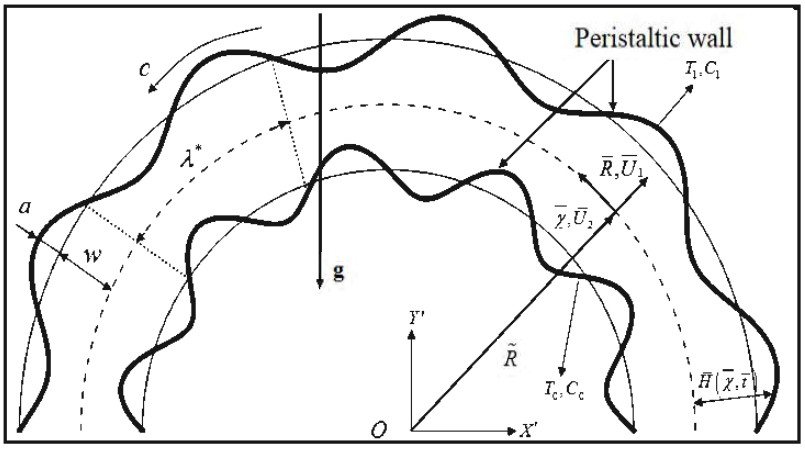

Fig. 3.1 Physical sketch of the problem

The boundary conditions associated with Eqs. (3.2) and (3.3) are (2.17) and (2.18). After using transformations given in Eq. (2.19), the governing equations in the wave frame become:

$$-c\frac{\partial u_1}{\partial x}+u_1\frac{\partial u_1}{\partial r}+\frac{\tilde{R}\left(u_2+c\right)}{r+\tilde{R}}\frac{\partial u_1}{\partial x}-\frac{\left(u_2+c\right)^2}{r+\tilde{R}}=-\frac{1}{\rho}\frac{\partial P}{\partial r}+\upsilon\left[\frac{1}{r+\tilde{R}}\frac{\partial}{\partial r}\left\{\left(r+\tilde{R}\right)\frac{\partial u_1}{\partial r}\right\}+\left(\frac{\tilde{R}}{r+\tilde{R}}\right)^2\frac{\partial^2 u_1}{\partial x^2}-\frac{u_1}{\left(r+\tilde{R}\right)^2}-\frac{2\tilde{R}}{\left(r+\tilde{R}\right)^2}\frac{\partial u_2}{\partial x}\right], \tag{3.4}$$

$$-c\frac{\partial u_2}{\partial x}+u_1\frac{\partial u_2}{\partial r}+\frac{\tilde{R}\left(u_2+c\right)}{r+\tilde{R}}\frac{\partial u_2}{\partial x}-\frac{\left(u_2+c\right)u_1}{r+\tilde{R}}=-\frac{\tilde{R}}{\rho\left(r+\tilde{R}\right)}\frac{\partial P}{\partial x}+\nu\left[\frac{1}{\left(r+\tilde{R}\right)}\frac{\partial}{\partial r}\left\{\left(r+\tilde{R}\right)\frac{\partial u_2}{\partial r}\right\}+\left(\frac{\tilde{R}}{r+\tilde{R}}\right)^2\frac{\partial^2 u_2}{\partial x^2}-\frac{u_2}{\left(r+\tilde{R}\right)^2}+\frac{2\tilde{R}}{\left(r+\tilde{R}\right)^2}\frac{\partial u_1}{\partial x}\right]-\rho g\beta_T(T-T_0)-\rho g\beta_C(C-C_0)-\frac{\sigma B^{*2}\tilde{R}^2\left(u_2+c\right)}{\left(\mathrm{r}+\tilde{R}\right)^2}. \tag{3.5}$$

The following dimensionless variables are defined to reduce the above equations in normalized form:

$$\left.\begin{aligned}&\overline{x}=\frac{2\pi}{\lambda^*}x,\ \eta=\frac{r}{a},\overline{u}_1=\frac{u_1}{c},\overline{u}_2=\frac{u_2}{c},\ \overline{p}=\frac{2\pi a^2}{\lambda^*\mu c}p,\delta=\frac{2\pi a}{\lambda^*},\ \mathrm{Re}=\frac{\rho ca}{\mu},Ha=aB^*\sqrt{\frac{\sigma}{\mu}},\\&\gamma=\frac{\tilde{R}}{a},\theta=\frac{T-T_1}{T_0-T_1},\phi=\frac{C-C_1}{C_0-C_1},Br=\frac{\mu c^2}{k\left(T_0-T_1\right)},Gr_C=\frac{a^2\rho g\beta_C(C-C_0)}{\mu c},Gr_T=\frac{a^3 g\beta_T(T_0-T_1)}{\nu^2}.\end{aligned}\right\} \tag{3.6}$$

Using the dimensionless variables given by Eq. (3.6) and stream function given by Eq. (2.25) and employing delta approximation. Eqs. (3.4) and (3.5) will contract to

$$\frac{\partial p}{\partial\eta}=0, \tag{3.7}$$

$$-\frac{\partial p}{\partial x}-\frac{1}{\gamma}\left(\frac{\partial}{\partial\eta}\left\{\left(\eta+\gamma\right)\frac{\partial^2\psi}{\partial\eta^2}\right\}+\frac{1}{\eta+\gamma}\left(1-\frac{\partial\psi}{\partial\eta}\right)\right)+\frac{Gr_T\theta\left(\eta+\gamma\right)}{\mathrm{Re}\,\gamma}+\frac{Gr_C\phi\left(\eta+\gamma\right)}{\mathrm{Re}\,\gamma}-\frac{\gamma Ha^2}{\eta+\gamma}\left(1-\frac{\partial\psi}{\partial\eta}\right)=0. \tag{3.8}$$

Elimination of pressure between Eqs. (3.7) and (3.8) yield

$$\frac{\partial}{\partial\eta}\left[\frac{1}{\gamma}\left(\frac{\partial}{\partial\eta}\left\{(\eta+\gamma)\frac{\partial^2\psi}{\partial\eta^2}\right\}+\frac{1}{\eta+\gamma}\left(1-\frac{\partial\psi}{\partial\eta}\right)\right)-\frac{Gr_T\theta(\eta+\gamma)}{\mathrm{Re}\gamma}+\frac{\phi Gr_C(\eta+k)}{k}+\frac{\gamma Ha^2}{\eta+\gamma}\left(1-\frac{\partial\psi}{\partial\eta}\right)\right]. \quad (3.9)$$

In summary, we have to solve Eqs. (2.23), (2.24) and (3.9) subject to boundary conditions (2.27) and (2.28). Now, in order to solve Eqs. (2.23), (2.24) and (3.9), one has to rely on suitable numerical method. Although Eqs. (2.23), (2.24) and (3.9) are linear ordinary differential equation, yet its closed form solution is difficult to obtain. Therefore, an implicit finite difference technique is employed for the solution, for which detail is already provided in chapter 2. Once the solution is known, the quantities of interest such as pressure rise, heat and mass transfer coefficients can be readily obtained through the formulas given in preceding chapter.

3.2 Computational results and interpretation

The computations carried out using the aforementioned method are displayed in terms of velocity profiles, pressure rise per wavelength profiles, temperature and concentration profiles, streamlines contours and heat transfer coefficient.

The axial velocity for some specific values of thermal Grashof number (Gr_T), concentration Grashof number (Gr_C), Hartmann number (Ha) and curvature parameter (γ) are shown in **Figs. 3.2 - 3.5**, respectively. **Fig. 3.2** shows an increase in the amplitude of the axial velocity with increasing thermal Grashof number. Thermal Grashof number is a parameter based on relative magnitudes of buoyancy and viscous forces. Larger values of

Grashof number correspond to the situation in which buoyancy effects are dominant over the viscous effects. Now due to curvature in channel, it is naturally anticipated that flow velocity will be asymmetric for smaller values of thermal Grashof number i.e. for weaker buoyancy effects. **Fig. 3.2** confirms the anticipated asymmetric profile for $Gr_T = 0$ with maximum lying below $\eta = 0$. This observation is quite interesting and it may finds application in scenarios where it is desired to minimize the effects of curvature without changing the geometry of the channel. This observation also highlights the role of thermal field in tunning the transport process without altering the geometrical and rheological parameters of the model. The role of rheological features of the fluid in tunning the transport is already highlighted by Javid et al. (2016). **Fig. 3.3** presents the axial velocity profile for several values of concentration Grashof number Gr_C. Concentration Grashof number is a parameter based on relative magnitudes of buoyancy force due to concentration gradients and viscous force. Larger values of Gr_C. correspond to situation in which buoyancy force due to concentration gradients is large. Contrary to **Fig. 3.2**, **Fig. 3.3** shows that rise in concentration Grashof number shifts the maxima in velocity profile toward lower wall of the channel. In this way, a rise in the concentration Grashof number intensifies the effect of curvature. The effects of Hartmann number on axial velocity are displayed in **Fig. 3.4**. Hartmann number is a parameter number based on relative magnitudes of magnetic force and viscous force. Larger values of Hartmann number correspond to the situation in which magnetic force dominates the viscous force. It is noticed that a rise in the Hartmann number suppresses the velocity in the upper part of the channel. The suppression is due to the fact that Lorentz force in presence of magnetic field

acts as a resistance to the flow as a result of peristalsis. However, suppression in axial velocity amplitude is not observed over the entire cross-section. **Fig. 3.5** displays the effect of dimensionless radius of curvature parameter γ on axial velocity. This figure clearly demonstrates asymmetry in axial velocity for decreasing values of γ.

Figs 3.6 - 3.9 demonstrate the effect of different parameters on pressure rise per wavelength. **Fig. 3.6** depicts the effect of thermal Grashof number Gr_T on Δp. It is noticed that Δp rises with increasing Gr_T in all three regions. **Fig. 3.7** shows the effect of concentration Grashof number Gr_C on Δp. A reverse trend is noted here i.e. pressure rise per wavelength decreases with increasing Gr_C in all three regions. **Fig. 3.8** demonstrates the effect of *Ha* on Δp. In pumping region $(\Theta > 0, \Delta p > 0)$, Δp increases with increasing *Ha*, while opposite results are obtained for free (Δp = 0) and co-pumping region $(\Theta > 0, \Delta p < 0)$. Here Δp decreases by rising *Ha*. **Fig. 3.9** depicts the effect of non-dimensional radius of curvature on Δp. It is examined that Δp rises with rising γ in all three regions. Both figures clearly highlight the significant effects of buoyancy force, magnetic force and curvature on Δp. In fact, the resistance offered by pressure gradient to peristaltic flow can be minimized by suitable choice of the involved parameters.

The profiles of temperature field for different values of thermal Grashof number (Gr_T), Brinkman number (*Br*) and Hartmann number (*Ha*) are shown through **Figs. 3.10 - 3.12**. It is noted that $\theta(\eta)$ increases over the entire cross-section with increasing each of Gr_T, Br and *Ha*. The increase in $\theta(\eta)$ with increasing Gr_T and *Ha* is due to retarding effect of these parameters on velocity. Brinkmann number is a parameter which is the ratio of

viscous heat to the heat transported by conduction. Larger values of Brinkmann correspond to the scenario when heat generated due to viscous dissipation is dominant. In such situation, increase in fluid temperature inside the channel is obviously justified.

The variations of *z* at upper wall for several values of Gr_T, Br and *Ha* are presented through **Figs. 3.13 - 3.15**. The profiles of *z* are clearly oscillating due to periodic oscillating nature of the channel walls. The amplitude of oscillations is found to increase with increasing Gr_T, Br and *Ha*.

The effects of Gr_T (thermal Grashof number), Br (Brinkman number), *Ha* (Hartmann number) and Gr_C (concentration Grashof number) on mass transfer are demonstrated through **Figs. 3.16 - 3.19.** It is observed that ϕ (η) decreases with increasing Gr_T, *Br* and *Ha*. In contrast, ϕ (η) rises with mounting Gr_C.

The streamlines of flow for different values of *Br* (Brinkman number), Gr_T (Grashof number) and *Ha* (Hartmann number) are shown in **Figs. 3.20 - 3.22**. The objective is to investigate the trapping phenomenon. **Fig. 3.20** shows the effect of *Br* on streamlines. For *Br* = 0.1, two circulating rolls exist in the channel. The lower roll increases in size while the upper one reduces with increasing *Br*. The two circulating cells in the lower roll also merge into a single cell with increasing *Br*. The effects of Gr_T on streamlines are shown through **Fig. 3.21**. This figure shows a complex streamlines pattern with multiple circulating cells for $Gr_T = 0.1$. All these cells merge into a single circulating roll with increasing Gr_T. **Fig. 3.22** depicts the effects of Hartmann number on streamlines. For *Ha* = 0.6, two circulating rolls can be identified in the flow field. The upper one in the

neighborhood of the upper wall is smaller in size than the lower one. The inner most circulating cells in the lower roll splits into circulating cells with increasing Hartmann number.

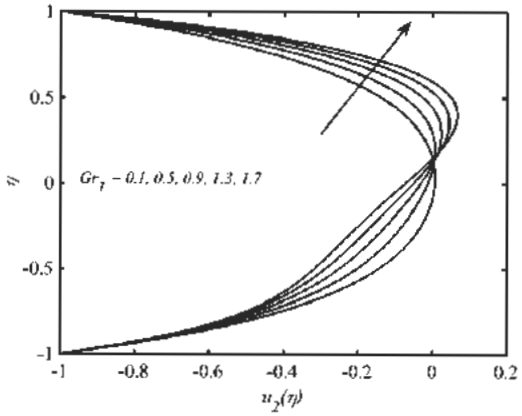

Fig. 3.2: Effect of Gr_T on velocity $u_2(\eta)$ for γ = 2, *Ha* = 0.5, $\lambda = 0.4$, Gr_C = 2 and Θ = 1.5.

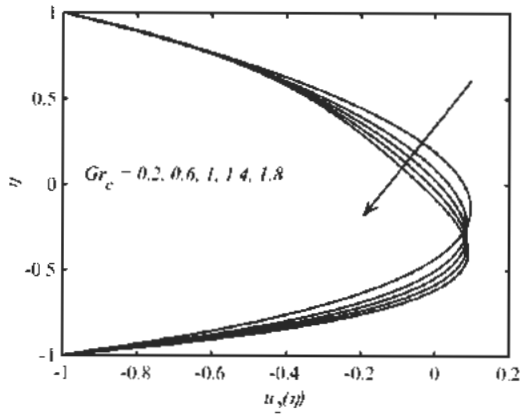

Fig. 3.3: Effect of Gr_C on velocity $u_2(\eta)$ for γ = 2, *Ha* = 0.5, $\lambda = 0.4$, and Θ = 1.5.

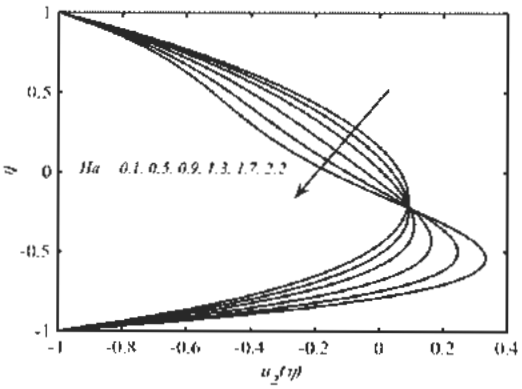

Fig. 3.4: Influence of *Ha* on $u_2(\eta)$ for γ = 2, Gr_T = 0.2, $\lambda = 0.4$, = 2 and $\Theta = 1.5$.

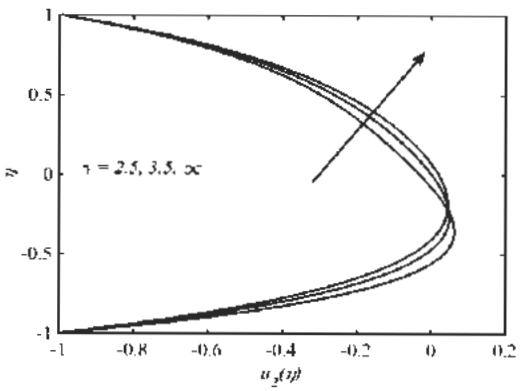

Fig. 3.5: Influence of γ on $u_2(\eta)$ for Gr_T = 0.2, *Ha* = 0.5, $\lambda = 0.4$, and $\Theta = 1.5$.

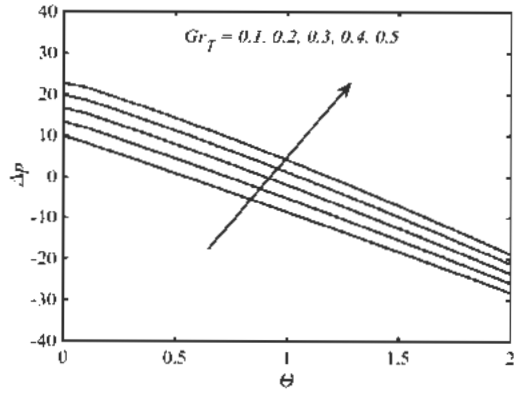

Fig. 3.6: Effect of Gr_T on Δp for $\gamma = 2$, $Ha = 0.5$, $\lambda = 0.4$, $Gr_C = 2$ and $\Theta = 1.5$.

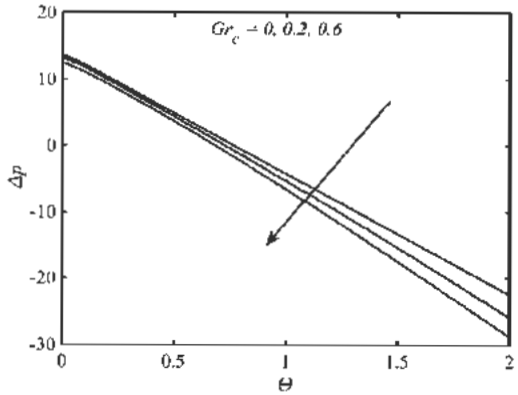

Fig. 3.7: Effect of Gr_C on Δp for $\gamma = 2$, $Ha = 0.5$, $\lambda = 0.4$, $Gr_T = 0.2$ and $\Theta = 1.5$.

.

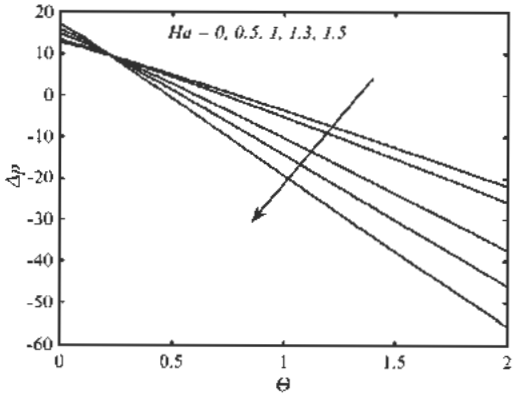

Fig. 3.8: Effect of Ha on Δp for $\gamma = 2$, $Gr_T = 0.2$, $\lambda = 0.4$, $Gr_C = 2$ and $\Theta = 1.5$.

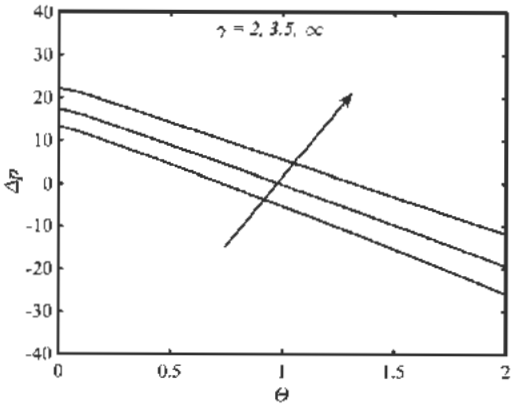

Fig. 3.9: Effect of γ on Δp for $Gr_T = 0.2$, $Ha = 0.5$, $\lambda = 0.4$, $Gr_C = 2$ and $\Theta = 1.5$.

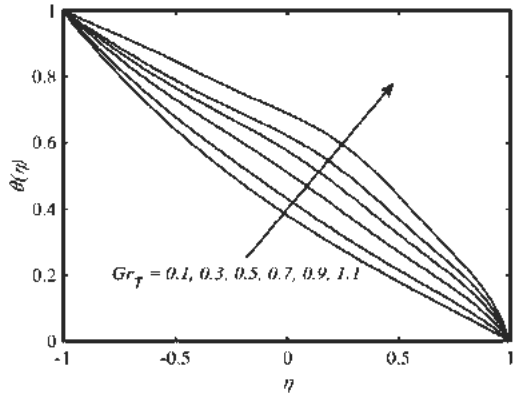

Fig. 3.10: Effect of Gr_T on temperature $\theta(\eta)$ for γ = 2, *Ha* = 0.5, $\lambda = 0.4$, Br = 2 and $\Theta = 1.5$.

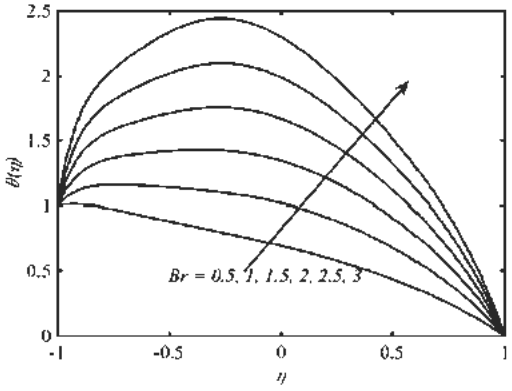

Fig. 3.11: Effect of *Br* on temperature $\theta(\eta)$ for γ = 2, *Ha* = 0.5, $\lambda = 0.4$, Gr_T = 0.2 and $\Theta = 1.5$.

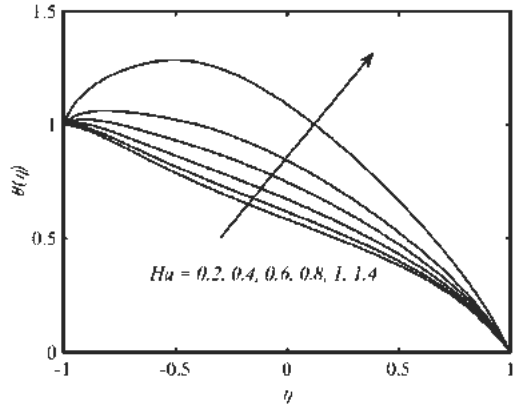

Fig. 3.12: Effect of *Ha* on temperature $\theta(\eta)$ for γ = 2, Gr_T = 0.2, $\lambda = 0.4$, Br = 2 and $\Theta = 1.5$.

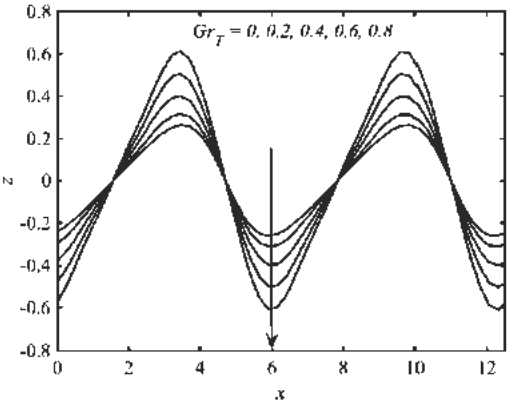

Fig. 3.13: Effect of Gr_T on heat transfer coefficient *z* for γ = 2, *Ha* = 0.5, $\lambda = 0.4$, Br = 0.5 and $\Theta = 1.5$.

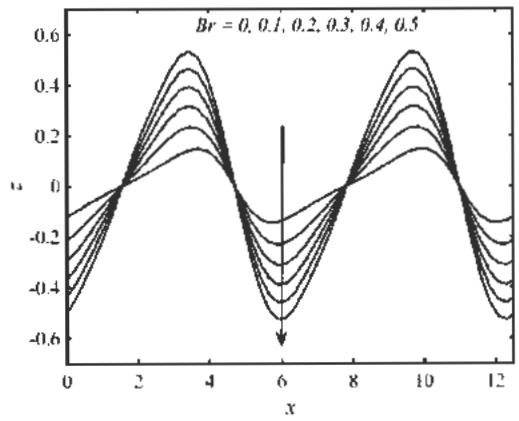

Fig. 3.14: Effect of *Br* on heat transfer coefficient *z* for γ = 2, *Ha* = 0.5, $\lambda = 0.4$, Gr_T = 0.2 and $\Theta = 1.5$.

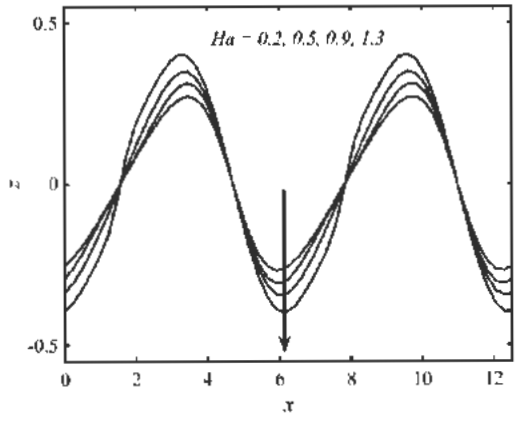

Fig. 3.15: Effect of *Ha* on heat transfer coefficient *z* for γ = 2, *Br* = 0.5, $\lambda = 0.4$, Gr_T = 0.2 and $\Theta = 1.5$.

.

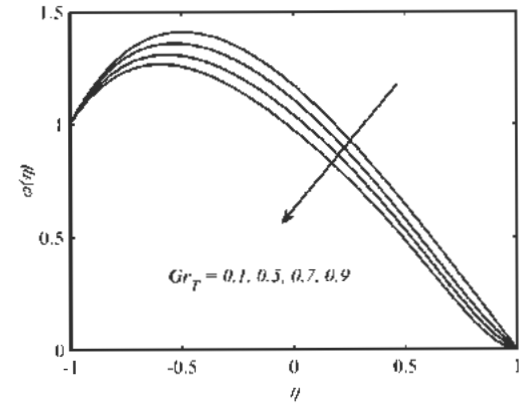

Fig. 3.16: Effect of Gr_T on concentration $\phi(\eta)$ for γ = 2, *Br* = 0.5, $\lambda = 0.4$, *Sr* = 1.5, *Sc* = 1.2 and Θ = 1.5.

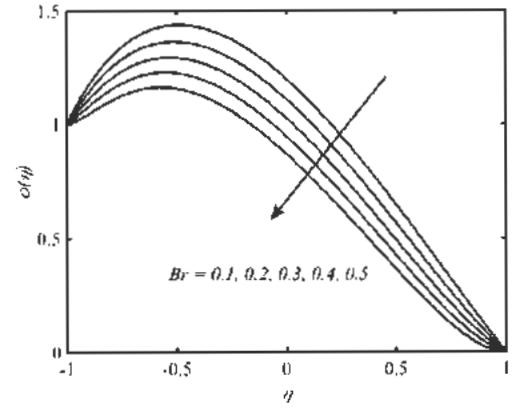

Fig. 3.17: Effect of *Br* on concentration $\phi(\eta)$ for γ = 2, Gr_T = 0.2, $\lambda = 0.4$, *Sr* = 1.5, *Sc* = 1.2 and Θ = 1.5.

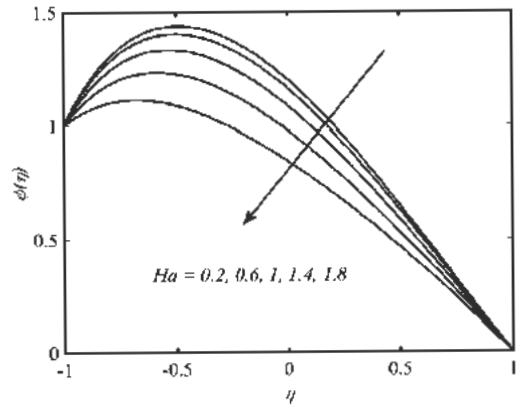

Fig. 3.18: Effect of *Ha* on $\phi(\eta)$ for $\gamma = 2$, $Gr_T = 0.2$, $\lambda = 0.4$, $Sr = 1.5$, $Sc = 1.2$ and $\Theta = 1.5$.

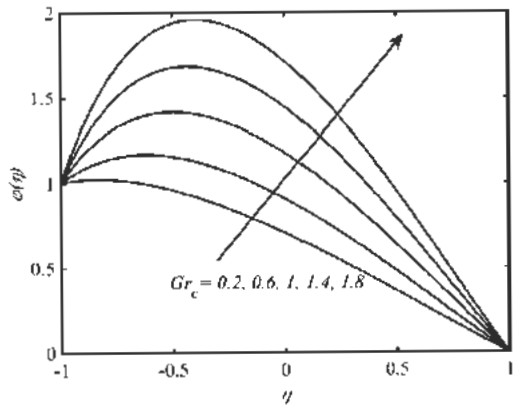

Fig. 3.19: Effect of Gr_C on $\phi(\eta)$ for $\gamma = 2$, $Gr_T = 0.2$, $\lambda = 0.4$, $Sr = 1.5$, $Sc = 1.2$ and $\Theta = 1.5$.

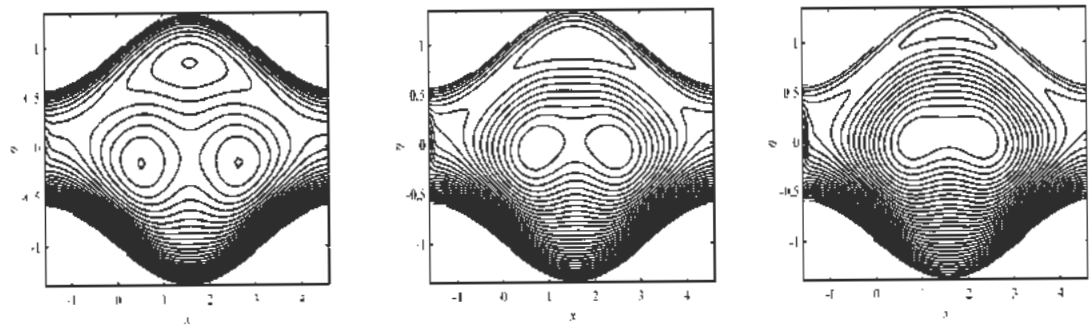

Fig 3.20: Flow patterns for (a) $Br = 0.1$ (b) $Br = 0.2$ (c) $Br = 0.3$. The other parameters chosen are $\gamma = 2$, $Ha = 0.5$, $\lambda = 0.4$, $Gr_T = 0.2$ and $\Theta = 1.5$.

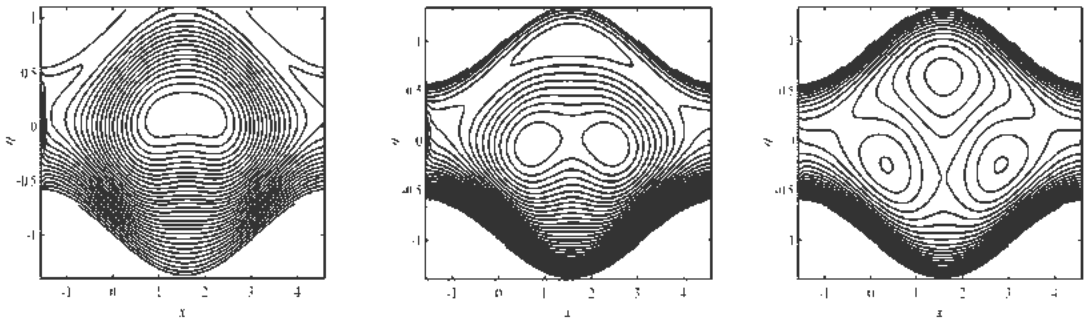

Fig 3.21: Flow patterns for (a) Gr_T = 0.1 (b) Gr_T = 0.2 (c) Gr_T = 0.3. The other parameters chosen are γ = 2, *Ha* = 0.5, $\lambda = 0.4$, *Br* = 2 and $\Theta = 1.5$.

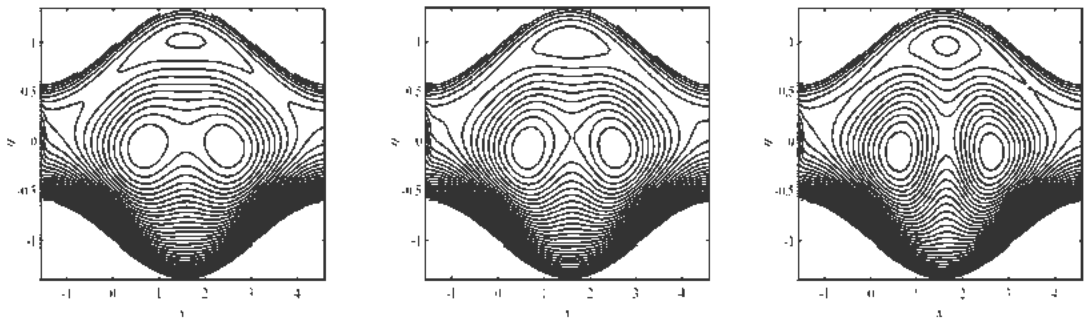

Fig 3.22: Flow patterns for (a) *Ha* = 0.6 (b) *Ha* = 1 (c) *Ha* = 1.4. The other parameters chosen are γ = 2, Gr_T = 0.2, $\lambda = 0.4$, *Br* = 2 and $\Theta = 1.5$.

Chapter 4

Heat and mass transfer effects on the peristaltic flow of Sisko fluid in a curved channel

In the present chapter heat and mass transfer phenomena in flow of non-Newtonian Sisko fluid induced by peristaltic activity through a curved channel have been investigated numerically using FDM. The governing equations are formulated in terms of curvilinear coordinates with appropriate boundary conditions. The velocity field, pressure rise per wavelength, stream function, concentration and temperature fields have been analyzed for the effects of curvature parameter, viscosity parameter and power law index. Additionally, the computation for heat transfer coefficient and Sherwood number carried out for selected thermo-physical parameters.

4.1 Mathematical formulation

An incompressible Sisko fluid is assumed inside the channel. The momentum and energy equations are given by

$$\rho \frac{d\,\mathbf{U}}{dt} = \nabla . \boldsymbol{\tau}, \tag{4.1}$$

$$\rho c_p \frac{d\,T}{dt} = k\nabla^2 T + \mu\Phi \ . \tag{4.2}$$

Eq. (4.2) can be also retrieved from Eq. (2.5) by setting Joule heating term equal to zero. The continuity equation remain same as used in previous chapters. Similarly, the concentration equation is given by Eq. (2.6). The Cauchy stress tensor $\boldsymbol{\tau}$ is given by

$$\boldsymbol{\tau} = -P\mathbf{I}+\mathbf{S}, \tag{4.3}$$

where $\mathbf{I}$ is the identity tensor, P is the pressure and $\mathbf{S}$ is the extra stress tensor which for Sisko fluid model (Wang et al. 2008) satisfies

$$\mathbf{S} = \left[a_1 + b_1 \left(\Pi\right)^{n-1} \right] \mathbf{A}_1. \tag{4.4}$$

Here a_1, b_1 and n are the infinite shear-rate viscosity, the consistency index and the power-law index, respectively. Also Π is given by

$$\Pi = \sqrt{\frac{1}{2}\mathbf{A}_1 : \mathbf{A}_1}. \tag{4.5}$$

Using Eq. (4.3) in Eq. (4.1) we get

$$\rho \frac{d\mathbf{U}}{dt} = -\nabla P + \nabla.\mathbf{S}. \tag{4.6}$$

Assuming velocity field defined by Eq. (2.11), Eqs. (4.2) and (4.3) yield

$$\begin{aligned} \rho\left[\frac{\partial U_1}{\partial t} + U_1 \frac{\partial U_1}{\partial R} + \frac{RU_2}{R+\tilde{R}} \frac{\partial U_1}{\partial \chi} - \frac{{U_2}^2}{R+\tilde{R}} \right] &= -\frac{\partial P}{\partial R} + \frac{1}{R+\tilde{R}} \frac{\partial}{\partial R}\left\{ \left(R+\tilde{R}\right) S_{RR} \right\} \\ &+ \frac{\tilde{R}}{R+\tilde{R}} \frac{\partial}{\partial \chi} S_{R\chi} - \frac{S_{\chi\chi}}{R+\tilde{R}}, \end{aligned} \tag{4.7}$$

$$\rho\left[\frac{\partial U_2}{\partial t}+U_1\frac{\partial U_2}{\partial R}+\frac{\tilde{R}U_2}{R+\tilde{R}}\frac{\partial U_2}{\partial \chi}-\frac{U_2U_1}{R+\tilde{R}}\right]=-\left(\frac{\tilde{R}}{R+\tilde{R}}\right)\frac{\partial P}{\partial \chi}+\frac{1}{\left(R+\tilde{R}\right)^2}\frac{\partial}{\partial R}\left\{\left(R+\tilde{R}\right)^2 S_{R\chi}\right\}$$
$$+\frac{\tilde{R}}{R+\tilde{R}}\frac{\partial}{\partial \chi}S_{\chi\chi}, \tag{4.8}$$

$$\rho c_p\left[\frac{\partial T}{\partial t}+U_1\frac{\partial T}{\partial R}+\frac{\tilde{R}U_2}{R+\tilde{R}}\frac{\partial T}{\partial \chi}\right]=k^*\left(\frac{1}{\left(R+\tilde{R}\right)}\frac{\partial}{\partial R}\left\{\left(R+\tilde{R}\right)\frac{\partial T}{\partial R}\right\}+\left(\frac{\tilde{R}}{R+\tilde{R}}\right)^2\frac{\partial^2 T}{\partial \chi^2}\right)+$$
$$S_{RR}\frac{\partial U_1}{\partial R}+S_{R\chi}\left(\frac{\partial U_2}{\partial R}+\frac{\tilde{R}}{R+\tilde{R}}\frac{\partial U_1}{\partial \chi}+\frac{\tilde{R}}{R+\tilde{R}}\frac{\partial U_2}{\partial \chi}-\frac{U_2}{R+\tilde{R}}\right)+S_{\chi\chi}\left(\frac{U_1}{R+\tilde{R}}+\frac{\tilde{R}}{R+\tilde{R}}\frac{\partial U_2}{\partial \chi}\right), \tag{4.9}$$

The boundary conditions associated with Eqs. (4.7) - (4.9) are given Eqs. (2.17) and (2.18). After using transformations given by Eq. (2.19), the governing equations in the wave frame become

$$\rho\left[-c\frac{\partial u_1}{\partial x}+u_1\frac{\partial u_1}{\partial r}+\frac{\tilde{R}\left(u_2+c\right)}{r+\tilde{R}}\frac{\partial u_1}{\partial x}-\frac{\left(u_2+c\right)^2}{r+\tilde{R}}\right]=-\frac{\partial p}{\partial r}+\frac{1}{r+\tilde{R}}\frac{\partial}{\partial r}\left\{\left(r+\tilde{R}\right)S_{rr}\right\}$$
$$+\frac{\tilde{R}}{r+\tilde{R}}\frac{\partial}{\partial x}S_{rx}-\frac{S_{xx}}{r+\tilde{R}}, \tag{4.10}$$

$$\rho\left[-c\frac{\partial u_2}{\partial x}+u_1\frac{\partial u_2}{\partial r}+\frac{\tilde{R}\left(u_2+c\right)}{r+\tilde{R}}\frac{\partial u_2}{\partial x}-\frac{\left(u_2+c\right)u_1}{r+\tilde{R}}\right]=-\left(\frac{\tilde{R}}{r+\tilde{R}}\right)\frac{\partial p}{\partial x}+\frac{1}{\left(r+\tilde{R}\right)^2}\frac{\partial}{\partial r}\left\{\left(\mathrm{r}+\tilde{R}\right)^2 S_{rx}\right\}$$
$$+\frac{\tilde{R}}{r+\tilde{R}}\frac{\partial}{\partial x}S_{xx}, \tag{4.11}$$

$$\rho c_p\left[-c\frac{\partial T}{\partial x}+u_1\frac{\partial T}{\partial r}+\frac{\tilde{R}\left(u_2+c\right)}{r+\tilde{R}}\frac{\partial T}{\partial x}\right]=k^*\left(\frac{1}{\left(r+\tilde{R}\right)}\frac{\partial}{\partial r}\left\{\left(r+\tilde{R}\right)\frac{\partial T}{\partial r}\right\}+\left(\frac{\tilde{R}}{r+\tilde{R}}\right)^2\frac{\partial^2 T}{\partial x^2}\right)+$$
$$S_{rr}\frac{\partial u_1}{\partial r}+S_{rx}\left(\frac{\partial u_2}{\partial r}+\frac{\tilde{R}}{r+\tilde{R}}\frac{\partial u_1}{\partial x}+\frac{\tilde{R}}{r+\tilde{R}}\frac{\partial u_2}{\partial x}-\frac{\left(u_2+c\right)}{r+\tilde{R}}\right)+S_{xx}\left(\frac{u_1}{r+\tilde{R}}+\frac{\tilde{R}}{r+\tilde{R}}\frac{\partial u_2}{\partial x}\right). \tag{4.12}$$

After using these dimensionless variables defined by Eq. (2.20) and stream function given by Eq. (2.25), applying long wavelength and low Reynolds approximations, Eqs (4.10) - (4.12) will contract to

$$\frac{\partial p}{\partial \eta} = 0, \tag{4.13}$$

$$-\frac{\partial p}{\partial x} + \frac{1}{\gamma(\eta+\gamma)}\frac{\partial}{\partial \eta}\left(\left(\eta+\gamma\right)^2 S_{\eta x}\right) = 0, \tag{4.14}$$

$$\frac{1}{(\eta+\gamma)}\frac{\partial}{\partial \eta}\left(\left(\eta+\gamma\right)\frac{\partial \theta}{\partial \eta}\right) + BrS_{\eta x}\left(-\frac{1}{\eta+\gamma}\left(1-\frac{\partial \psi}{\partial \eta}\right) - \frac{\partial^2 \psi}{\partial \eta^2}\right) = 0, \tag{4.15}$$

where

$$\bar{\boldsymbol{S}} = \frac{a_1}{\mu c}\boldsymbol{S}, a^* = \frac{a_1}{\mu}, \mu = \frac{b_1}{\left(\frac{a_1}{c}\right)^{n-1}}, \tag{4.16}$$

$$S_{xx} = 0, \tag{4.17}$$

$$S_{\eta x} = \left(a^* + \left(\Pi\right)^{n-1}\right)\left(-\frac{\partial^2 \psi}{\partial \eta^2} - \frac{1}{\eta+\gamma}\left(1-\frac{\partial \psi}{\partial \eta}\right)\right), \tag{4.18}$$

$$S_{\eta\eta} = 0, \tag{4.19}$$

$$\Pi = -\frac{\partial^2 \psi}{\partial \eta^2} - \frac{1}{\eta+\gamma}\left(1-\frac{\partial \psi}{\partial \eta}\right). \tag{4.20}$$

Inserting Eq. (4.18) into Eqs. (4.14) and (4.15), we get

$$-\frac{\partial p}{\partial x}+\frac{1}{\gamma(\eta+\gamma)}\frac{\partial}{\partial\eta}\left(\left(\eta+\gamma\right)^2\left(a^*+\left(\prod\right)^{n-1}\right)\left(-\frac{\partial^2\psi}{\partial\eta^2}-\frac{1}{\eta+\gamma}\left(1-\frac{\partial\psi}{\partial\eta}\right)\right)\right)=0, \qquad (4.21)$$

$$\frac{1}{(\eta+\gamma)}\frac{\partial}{\partial\eta}\left(\left(\eta+\gamma\right)\frac{\partial\theta}{\partial\eta}\right)+Br\left(a^*+\left(\prod\right)^{n-1}\right)\left(-\frac{1}{\eta+\gamma}\left(1-\frac{\partial\psi}{\partial\eta}\right)-\frac{\partial^2\psi}{\partial\eta^2}\right)^2=0. \qquad (4.22)$$

Solving Eq. (4.13) and (4.21), we get

$$\frac{\partial}{\partial\eta}\left(\left(\frac{1}{(\eta+\gamma)}\frac{\partial}{\partial\eta}\left(\left(\eta+\gamma\right)^2\left(a^*+\left(\prod\right)^{n-1}\right)\right)\right)\left(\frac{1}{\eta+\gamma}\left(1-\frac{\partial\psi}{\partial\eta}\right)+\frac{\partial^2\psi}{\partial\eta^2}\right)\right)=0. \qquad (4.23)$$

Now, we have to solve Eqs. (2.24), (4.22) and (4.23) subject of boundary conditions defined by Eqs. (2.27) and (2.28). The finite difference scheme employed for the solution in previous two chapters is also used here to simulate the above mentioned boundary value problem.

4.2 Computational results and interpretation

In this section, we interpret the computational results provided in **Figs. 4.1 - 4.20** to analyze flow velocity, pressure rise over one wavelength, temperature distribution, mass concentration and streamlines for different values of the factors γ, *n*, *Br*, *Sr*, *Sc*, and a^*.

Figs. 4.1 and **4.2** present the redial distribution of the transverse velocity u_2 for different values of a^* and *n*. **Fig. 4.1** shows for shear-thinning bio-fluids (*n<1*) an increase in a^* accelerate the flow. The structure of axial velocity is also substantially affected with the increase in a^*. For smaller values of a^* the flow velocity is asymmetric with maximum in it appearing above $\eta=0.$ With increasing a^* to 1.5 the velocity approximately regained its

symmetry. Larger values of a^* represent the case when viscous effects are stronger than the power-law effects. In such situation, the curvature effects on $u_2(\eta)$ are not significant. However, as a^* decreases in value, the effects of curvature become dominant. **Fig. 4.2** illustrates the axial velocity profile for three different values of power-law index (n). It is noticed that axial velocity rises with rising n. For $n<1$ (pesudoplastic/ shear- thinning bio-fluids), the axial velocity exhibits a boundary layer type character. However, such characteristic of axial velocity vanishes for Newtonian ($n = 0$) and shear-thinning/ dilatant fluids. For such fluids, non-vanishing gradients in axial velocity occur in the whole flow span $[0, h]$.

The pressure rise per wavelength against flow rate is plotted in **Figs. 4.3 - 4.5** for different values of a^*, n and γ. Three distinct cases can be identified from these figures namely peristaltic pumping case, free pumping case and augmented pumping case. It is noticed that for peristaltic pumping case, Δp rises by rising a^*, n and γ for a fixed value of Θ. This is consistent with observations already made for the axial velocity in **Figs. 4.1** and **4.2**. For the case when $\Delta p = 0$ an increase in a^* does not significantly affect the magnitude of the flow rate Θ. However, the magnitude of Θ corresponding to $\Delta p = 0$ increases with increasing power-law index and channel curvature. In augmented pumping case, the flow due to peristalsis is assisted by the pressure gradient and the magnitude of assistance increase with increasing $a^*$and n. In contrast, the assistance provided by Δp declines with increasing γ.

The effects of a^* and Br on the temperature inside the channel are graphically displayed in **Figs. 4.6** and **4.7** for shear thinning bio-fluid ($n<1$). An enhancement in the temperature

inside the channel is observed with increase in a^* and *Br*.

Figs 4.8 and **4.9** depict the effects of a^* and *Br* on z at the upper wall. It is noticed through both figures that *z* (heat transfer coefficient) varies periodically along the channel. This is in fact a direct consequence of the periodic characteristic of the peristaltic wall. Furthermore, the amplitude of heat transfer coefficient enhances via increasing a^* and *Br*.

Figs 4.10 - 4.13 depict the conduct of the mass concentration $\phi(\eta)$ for various values of a^*, *Br*, *Sr* and *Sc*, respectively. These figures show that $\phi(\eta)$ enhancing with increasinga^*, *Br*, *Sr* and *Sc*.

The impact of several parameters such as a^*, *Br*, *Sr*, and *Sc* on the Sherwood number (*Sh*) at the upper wall is shown through **Figs. 4.14 - 4.17**. Similar to the heat transfer coefficient, Sherwood number also oscillates periodically. Further, the amplitude of oscillations in Sherwood number (*Sh*) enhance via increasing a^*, *Br*, *Sr*, and *Sc*.

The particular flow patterns for three various values of viscosity parameter (a^*) are shown in **Fig. 4.18**. This figure shows that for a^*= 0.1 a mingling fluid bolus concerted in the upper half of channel. No significant change is observed by increasing a^* from 0.1 to 2, except the appearance of tiny vortices near the lower part of channel. **Fig. 4.19** exhibits the effect of *n* (power law index) on streamlines for a^* = 0.1. This figure shows that a concentrated fluid bolus is mingling in the lower part of the channel for $n \geq 0.9$. It is also noticed that a tiny eddy is appeared in neighborhood of upper wall. Furthermore, it is examined that with further increase in value of *n* from 0.98 to 1 the fluid behavior is changing from shear thinning to Newtonian fluid. A further rise in the value of (power-law index) *n* does not effect on the circulating phenomena in the upper part of the channel.

However, a slight decrease in the size of eddy near the lower wall is noted. The influence of channel curvature on trapping phenomena is illustrated through **Fig. 4.20**. This figure shows that for $\gamma = 2$ a concentrated bolus of mingling fluid is observed in neighborhood of upper wall. The bolus regain its symmetric shape as $\gamma \to \infty$. From the above discussion it is concluded that the role of γ is to affect the bolus symmetry while the effect of *n* is to shift the center of circulation from lower part of channel to the upper one.

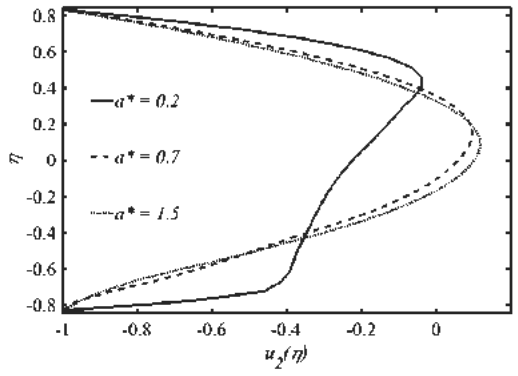

Fig. 4.1: Effect of a^* on velocity $u_2(\eta)$ for $n = 0.7$, $\lambda = 0.4$, and $\Theta = 1.5$.

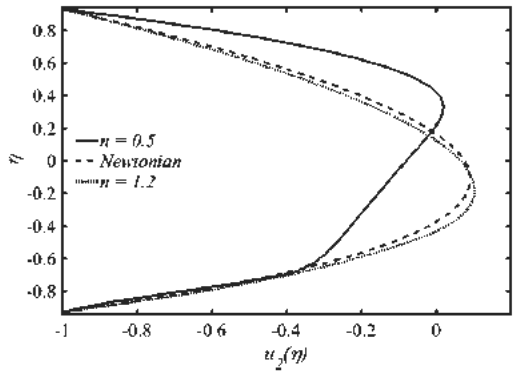

Fig. 4.2: Effect of n on velocity $u_2(\eta)$ for $\gamma = 2$, $\lambda = 0.4$, and $\Theta = 1.5$.

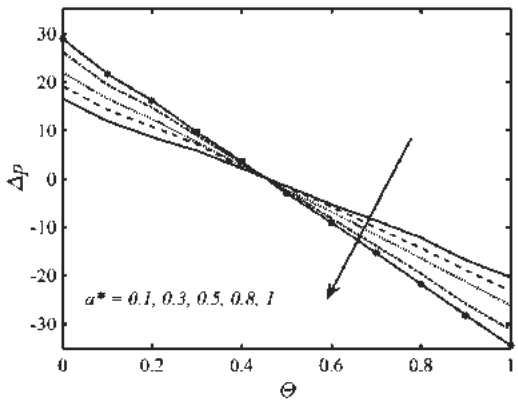

Fig. 4.3: Effect of a^* on pressure rise per wavelength for $n = 0.7$, $\lambda = 0.4$, and $\gamma = 2$.

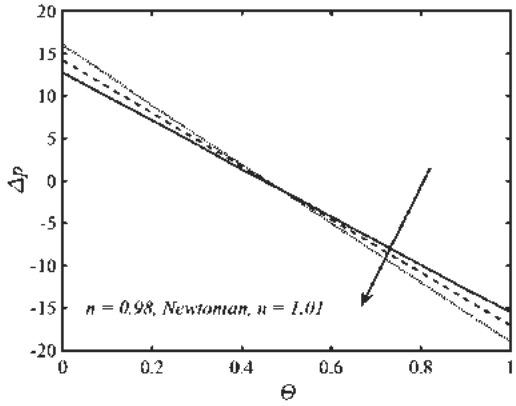

Fig. 4.4: Effect of n on pressure rise per wavelength for $a^* = 0.1$, $\lambda = 0.4$, and $\gamma = 2$.

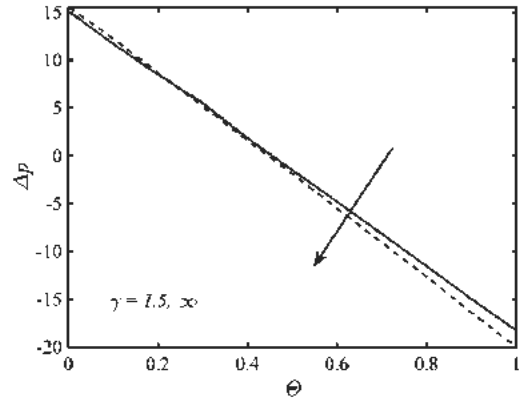

Fig. 4.5: Effect of γ on pressure rise per wavelength for n = 0.99, a^* = 0.1, and $\lambda = 0.4$.

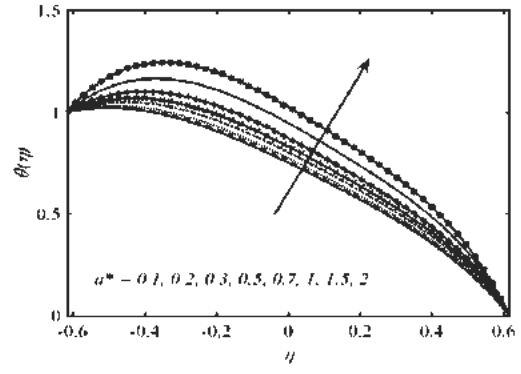

Fig. 4.6: Effect of a^* on temperature $\theta(\eta)$ for n = 0.95, Br = 0.5, $\lambda = 0.4$ and $\gamma = 2$.

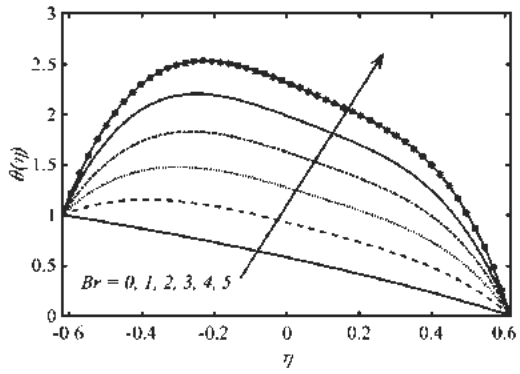

Fig. 4.7: Effect of Br on temperature $\theta(\eta)$ for n = 0.95, a^* = 0.1, $\lambda = 0.4$ and $\gamma = 2$.

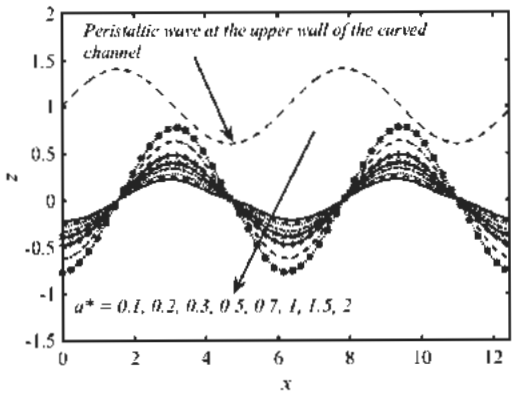

Fig. 4.8: Influence of a^* on z at upper wall for n = 0.98, Br = 0.5 and $\gamma = 2$.

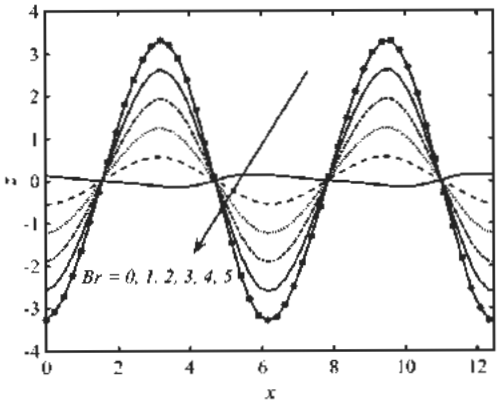

Fig. 4.9: Influence of Br on z at upper wall for a^* = 0.1, n = 0.98 and $\gamma = 2$.

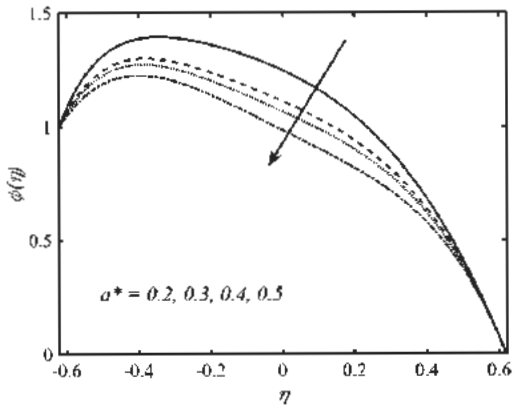

Fig. 4.10: Influence of a^* on $\phi(\eta)$ for n = 0.9, Br = 2, Sr = 1, Sc = 1, $\lambda = 0.4$ and $\gamma = 2$.

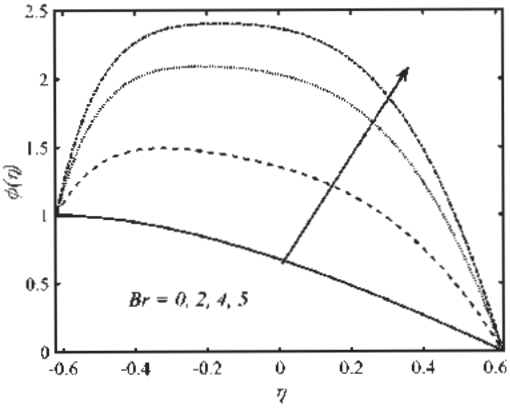

Fig. 4.11: Influence of Br on $\phi(\eta)$ for n = 0.9, Sr = 1, Sc = 1, $\lambda = 0.4$, and $\gamma = 2$.

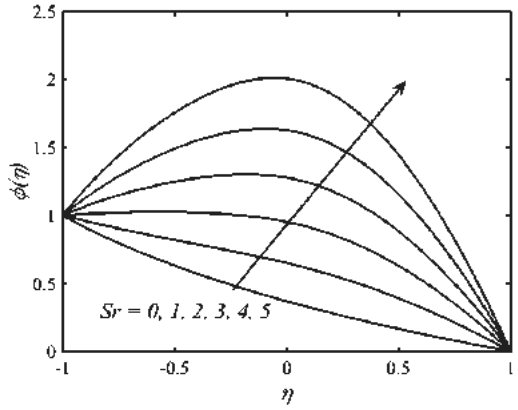

Fig. 4.12: Influence of *Sr* on $\phi(\eta)$ for *n* = 0.9, a^* = 0.1, *Br* = 2, $\lambda = 0.4$ and $\gamma = 2$.

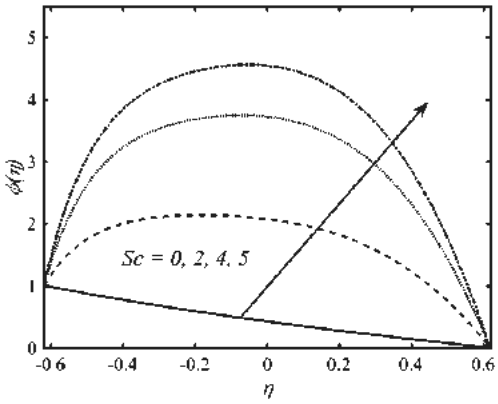

Fig. 4.13: Influence of *Sc* on $\phi(\eta)$ for *n* = 0.9, a^* = 0.1, *Sr* = 1, *Br* = 2 and $\gamma = 2$.

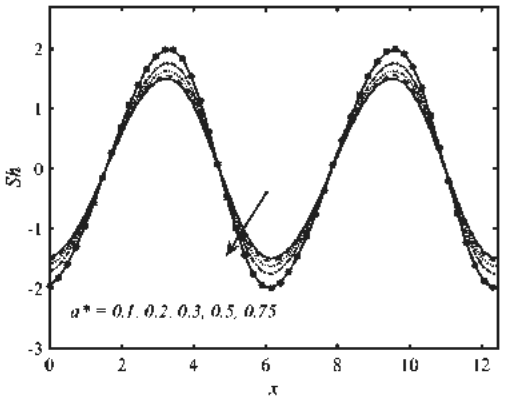

Fig. 4.14: Effect of a^* on Sherwood number *Sh* at upper wall for *n* = 0.9, *Br* = 2, *Sr* = 1, *Sc* = 1, $\lambda = 0.4$, and $\gamma = 2$.

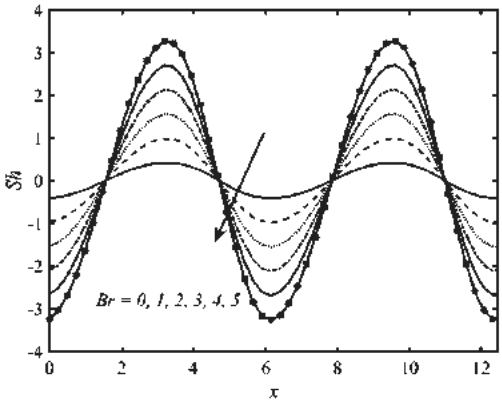

Fig. 4.15: Effect of *Br* on Sherwood number *Sh* at upper wall for *n* = 0.98, *Sr* = 1, *Sc* = 1, $\lambda = 0.4$, and $\gamma = 2$.

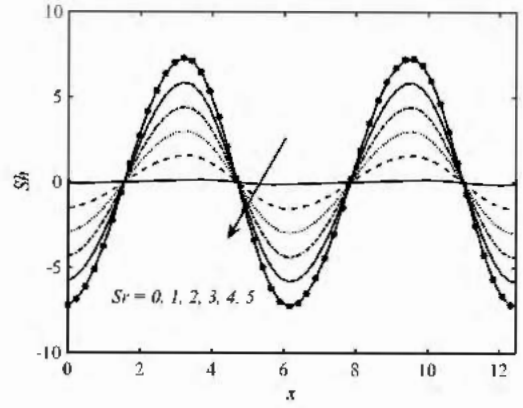

Fig. 4.16: Effect of Soret number *Sr* on Sherwood number *Sh* at upper wall for *n* = 0.98, *Sc* = 1, $\lambda = 0.4$, and $\gamma = 2$.

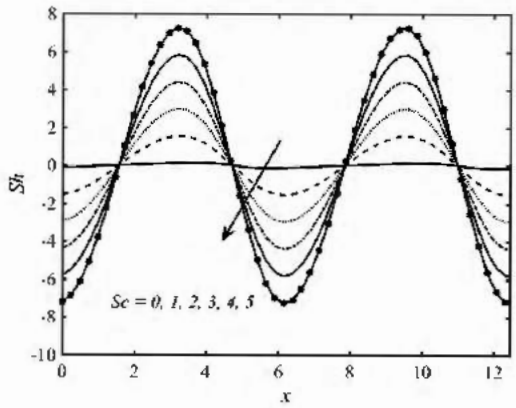

Fig. 4.17: Effect of Schmidt number *Sc* on Sherwood number *Sh* at upper wall for *n* = 0.98, *Sr* = 1, $\lambda = 0.4$, and $\gamma = 2$.

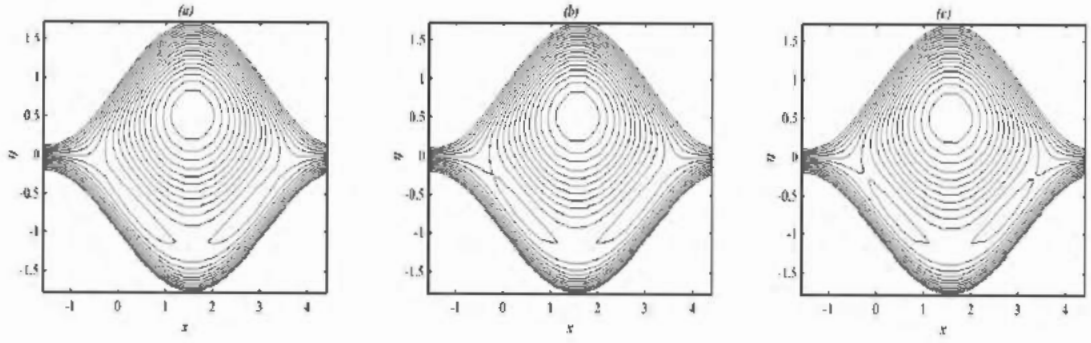

Fig. 4.18: Flow patterns for (a) $a^* = 0.1$, (b) $a^* = 0.98$, and (c) $a^* = 2$, for *n* = 0.98, using $\lambda = 0.4$ and $\gamma = 2$.

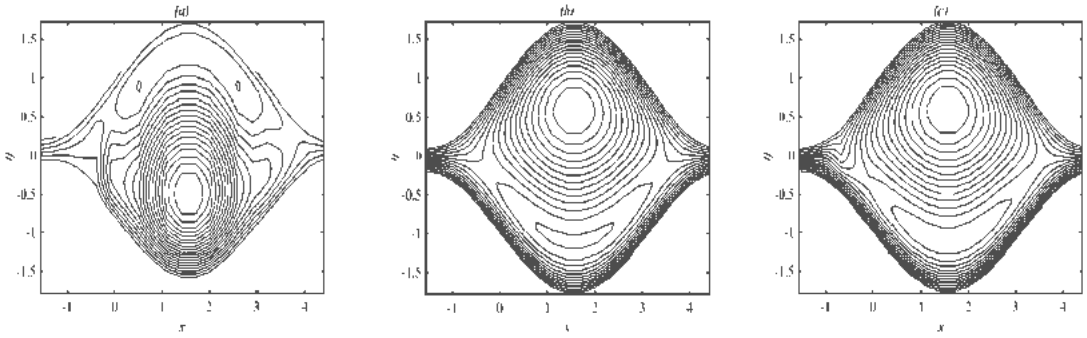

Fig. 4.19: Flow patterns for (a) n = 0.9, (b) n = 1, and (c) n = 1.05, for $\gamma = 2$, using $a^* = 0.1$ and $\lambda = 0.4$.

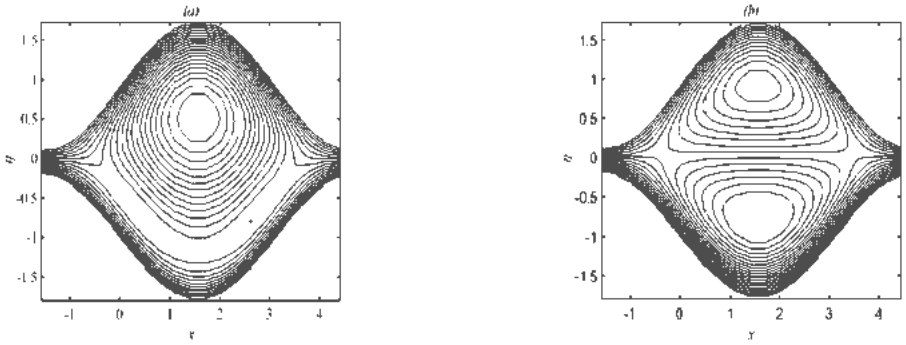

Fig. 4.20: Flow patterns for (a) $\gamma = 2$, and (b) $\gamma \to \infty$, for n = 0.98, using $a^* = 0.1$, and $\lambda = 0.4$.

Chapter 5

Numerical modeling of non-isothermal hydromagnetic peristaltic flow of a bio-fluid in a curved channel

In this chapter we investigate numerically the theoretical aspects of heat and mass transfer in peristaltic transport of Carreau fluid through a curved channel. The computations for axial velocity, pressure rise, temperature field, mass concentration and stream function are carried out under delta approximation by utilizing appropriate numerical implicit finite difference technique. The implementation of numerical procedure and graphical representation of the computations are accomplished using MATLAB language. The impacts of rheological parameters of Carreau fluid, Brinkmann number curvature parameter and Hartmann number are shown and discussed briefly.

5.1 Mathematical formulation

It is assumed that Carreau fluid occupied the space inside the magnetically influenced curved channel. The shape of both walls is described mathematically given by Eqs. (2.1) and (2.2). The momentum and energy equations are given by

$$\rho \frac{d\,\mathbf{U}}{dt} = -\nabla P + \nabla.\mathbf{S} + \mathbf{J} \times \mathbf{B}, \tag{5.1}$$

$$\rho c_p \frac{d\,T}{dt} = k\nabla^2 T + \mu\Phi. \tag{5.2}$$

The continuity and concentration equations are given by Eqs. (2.3) and (2.6), respectively. For Carreau fluid model extra stress tensor $\mathbf{S}$ in Eq. (5.1) is given by **(**Ali et al. 2015a)

$$\mathbf{S}=\left[\mu_{\infty}+\left(\mu_{0}-\mu_{\infty}\right)\left(1+\left(\Gamma\Pi\right)^{2}\right)^{\frac{n-1}{2}}\right]\mathbf{A_1}, \tag{5.3}$$

where μ_0 is the zero shear-rate viscosity, μ_∞ is the infinite-shear-rate viscosity, *n* is the index of power-law, Γ is the time constant and Π is determined by Eq. (4.5). The magnetic field $\mathbf{B}$ in radial direction is given by Eq. (2.7) and the term $\mathbf{J}\times\mathbf{B}$ is given by Eq. (2.10). After using velocity field given in Eq. (2.11), Eqs. (5.1) and (5.2) will become

$$\begin{aligned}&\rho\left[\frac{\partial U_1}{\partial t}+U_1\frac{\partial U_1}{\partial R}+\frac{\tilde{R}U_2}{R+\tilde{R}}\frac{\partial U_1}{\partial \chi}-\frac{{U_2}^2}{R+\tilde{R}}\right]=-\frac{\partial P}{\partial R}+\frac{1}{R+\tilde{R}}\frac{\partial}{\partial R}\left\{\left(R+\tilde{R}\right)S_{RR}\right\}\\&+\frac{\tilde{R}}{R+\tilde{R}}\frac{\partial}{\partial \chi}S_{R\chi}-\frac{S_{\chi\chi}}{R+\tilde{R}},\end{aligned} \tag{5.4}$$

$$\begin{aligned}&\rho\left[\frac{\partial U_2}{\partial t}+U_1\frac{\partial U_2}{\partial R}+\frac{\tilde{R}U_2}{R+\tilde{R}}\frac{\partial U_2}{\partial \chi}-\frac{U_2U_1}{R+\tilde{R}}\right]=-\left(\frac{\tilde{R}}{R+\tilde{R}}\right)\frac{\partial P}{\partial \chi}+\frac{1}{\left(R+\tilde{R}\right)^2}\frac{\partial}{\partial R}\left\{\left(R+\tilde{R}\right)^2S_{R\chi}\right\}\\&+\frac{\tilde{R}}{R+\tilde{R}}\frac{\partial}{\partial \chi}S_{\chi\chi}-\frac{\sigma B^{*2}U_2\tilde{R}^2}{\left(\mathrm{R}+\tilde{R}\right)^2},\end{aligned} \tag{5.5}$$

$$\begin{aligned}&\rho c_p\left[\frac{\partial T}{\partial t}+U_1\frac{\partial T}{\partial R}+\frac{\tilde{R}U_2}{R+\tilde{R}}\frac{\partial T}{\partial X}\right]=k^*\left(\frac{1}{\left(R+\tilde{R}\right)}\frac{\partial}{\partial R}\left\{\left(R+\tilde{R}\right)\frac{\partial T}{\partial R}\right\}+\left(\frac{\tilde{R}}{R+\tilde{R}}\right)^2\frac{\partial^2T}{\partial X^2}\right)+\\&S_{RR}\frac{\partial U_1}{\partial R}+S_{RX}\left(\frac{\partial U_2}{\partial R}+\frac{\tilde{R}}{R+\tilde{R}}\frac{\partial U_1}{\partial X}+\frac{\tilde{R}}{R+\tilde{R}}\frac{\partial U_2}{\partial X}-\frac{U_2}{R+\tilde{R}}\right)+S_{XX}\left(\frac{U_1}{R+\tilde{R}}+\frac{\tilde{R}}{R+\tilde{R}}\frac{\partial U_2}{\partial X}\right).\end{aligned} \tag{5.6}$$

Now employing the transformations given by Eq. (2.19) and using dimensionless variables defined by Eq. (2.20) we get

$$\delta \,\mathrm{Re}\left[-\delta \frac{\partial u_1}{\partial x} + u_1 \frac{\partial u_1}{\partial \eta} + \delta \frac{\gamma \left(u_2 + 1\right)}{\eta + \gamma} \frac{\partial u_1}{\partial x} - \frac{\left(u_2 + 1\right)^2}{\eta + \gamma} \right] = -\frac{\partial p}{\partial \eta} + \delta \left(\frac{1}{\eta + \gamma} \frac{\partial}{\partial \eta} \left\{ \left(\eta + \gamma\right) S_{\eta\eta} \right\} + \delta \frac{\gamma}{\eta + \gamma} \frac{\partial}{\partial x} S_{\eta x} - \frac{S_{xx}}{\eta + \gamma} \right), \tag{5.7}$$

$$\mathrm{Re}\left[-\delta \frac{\partial u_2}{\partial x} + u_1 \frac{\partial u_2}{\partial \eta} + \delta \frac{\gamma \left(u_2 + 1\right)}{\eta + \gamma} \frac{\partial u_2}{\partial x} - \frac{\left(u_2 + 1\right) u_1}{\eta + \gamma} \right] = -\left(\frac{\gamma}{\eta + \gamma} \right) \frac{\partial p}{\partial x} + \frac{1}{\left(\eta + \gamma\right)^2} \frac{\partial}{\partial \eta} \left\{ \left(\eta + \gamma\right)^2 S_{\eta x} \right\} + \delta \frac{\gamma}{\eta + \gamma} \frac{\partial}{\partial x} S_{xx} - \frac{\mathrm{Ha}^2 \gamma^2 \left(u_2 + 1\right)}{\left(\eta + \gamma\right)^2}, \tag{5.8}$$

$$\frac{\rho c_p}{k^*} \left[-c\delta \frac{\partial \theta}{\partial x} + u_1 \frac{\partial \theta}{\partial \eta} + \delta \frac{k \left(u_2 + c\right)}{\eta + k} \frac{\partial \theta}{\partial x} \right] = \frac{1}{\left(\eta + k\right)} \frac{\partial}{\partial \eta} \left\{ \left(\eta + k\right) \frac{\partial \theta}{\partial \eta} \right\} + \delta^2 \left(\frac{k}{\eta + k} \right)^2 \frac{\partial^2 \theta}{\partial x^2} + Br \left(S_{\eta\eta} \frac{\partial u_1}{\partial \eta} + S_{\eta x} \left(\frac{\partial u_2}{\partial \eta} + \frac{\delta k}{\eta + k} \frac{\partial u_1}{\partial x} + \delta \frac{k}{\eta + k} \frac{\partial u_2}{\partial x} - \frac{\left(u_2 + c\right)}{\eta + k} \right) + S_{xx} \left(\frac{u_1}{\eta + k} + \delta \frac{k}{\eta + k} \frac{\partial u_2}{\partial x} \right) \right). \tag{5.9}$$

In components form, Eq. (5.3) gives

$$\left.\begin{aligned} S_{xx} &= 2\left(\alpha + \left(1 - \alpha\right) \left(1 + We^2 \Pi^2\right)^{\frac{n-1}{2}} \right) \frac{\partial u_1}{\partial \eta}, && (a) \\ S_{\eta x} &= \left(\alpha + \left(1 - \alpha\right) \left(1 + We^2 \Pi^2\right)^{\frac{n-1}{2}} \right) \left(\frac{\partial u_2}{\partial \eta} + \frac{\gamma}{\eta + \gamma} \frac{\partial u_1}{\partial \eta} - \frac{\left(1 + u_2\right)}{\eta + \gamma} \right), && (b) \\ S_{\eta\eta} &= 2\left(\alpha + \left(1 - \alpha\right) \left(1 + We^2 \Pi^2\right)^{\frac{n-1}{2}} \right) \left(\delta \frac{\gamma}{\eta + \gamma} \frac{\partial u_2}{\partial x} + \frac{u_1}{\eta + \gamma} \right), && (c) \end{aligned}\right\} \tag{5.10}$$

where

$$\Pi^2 = \frac{1}{2} \left(\left(2 \frac{\partial u_1}{\partial \eta} \right)^2 + 2 \left(\frac{\partial u_2}{\partial \eta} + \frac{\gamma}{\eta + \gamma} \frac{\partial u_1}{\partial \eta} - \frac{\left(1 + u_2\right)}{\eta + \gamma} \right)^2 + \left(\delta \frac{2\gamma}{\eta + \gamma} \frac{\partial u_2}{\partial x} + \frac{2u_1}{\eta + \gamma} \right)^2 \right). \tag{5.11}$$

After using stream function defined by Eq. (2.25) and low Reynolds and long wavelength number approximations, the Eqs. (5.7) - (5.10) are reduced to

$$\frac{\partial p}{\partial \eta}=0, \tag{5.12}$$

$$-\frac{\partial p}{\partial x}+\frac{1}{\gamma(\gamma+\eta)}\frac{\partial}{\partial \eta}\left(\left(\gamma+\eta\right)^2 S_{\eta x}\right)-\frac{Ha^2\gamma}{(\gamma+\eta)}\left(1-\frac{\partial \psi}{\partial \eta}\right)=0, \tag{5.13}$$

$$\frac{1}{(k+\eta)}\frac{\partial}{\partial \eta}\left(\left(k+\eta\right)\frac{\partial \theta}{\partial \eta}\right)+BrS_{\eta x}\left(-\frac{1}{k+\eta}\left(1-\frac{\partial \psi}{\partial \eta}\right)-\frac{\partial^2 \psi}{\partial \eta^2}\right)=0, \tag{5.14}$$

$$\left.\begin{aligned} &S_{xx}=0, && (a)\\ &S_{x\eta}=\left(\alpha+\left(1-\alpha\right)\left(1+We^2\Pi^2\right)^{\frac{n-1}{2}}\right)\left(-\frac{\partial^2 \psi}{\partial \eta^2}-\frac{1}{\eta+\gamma}\left(1-\frac{\partial \psi}{\partial \eta}\right)\right), && (b)\\ &S_{\eta\eta}=0. && (c) \end{aligned}\right\} \tag{5.15}$$

Inserting Eq. (5.15) into Eqs. (5.13) and (5.14) we get

$$\begin{aligned} &-\frac{\partial p}{\partial x}+\frac{1}{\gamma(\eta+\gamma)}\frac{\partial}{\partial \eta}\left(\left(\eta+\gamma\right)^2\left(\alpha+\left(1-\alpha\right)\left(1+We^2\Pi^2\right)^{\frac{n-1}{2}}\right)\left(-\frac{\partial^2 \psi}{\partial \eta^2}-\frac{1}{\eta+\gamma}\left(1-\frac{\partial \psi}{\partial \eta}\right)\right)\right)\\ &-\frac{Ha^2\gamma}{(\eta+\gamma)}\left(1-\frac{\partial \psi}{\partial \eta}\right)=0, \end{aligned} \tag{5.16}$$

$$\frac{1}{(k+\eta)}\frac{\partial}{\partial \eta}\left(\left(k+\eta\right)\frac{\partial \theta}{\partial \eta}\right)+Br\left(\alpha+\left(1-\alpha\right)\left(1+We^2\Pi^2\right)^{\frac{n-1}{2}}\right)\left(-\frac{1}{k+\eta}\left(1-\frac{\partial \psi}{\partial \eta}\right)-\frac{\partial^2 \psi}{\partial \eta^2}\right)^2=0. \tag{5.17}$$

Solving Eq. (5.12) and (5.16) we get

$$\begin{aligned} &\frac{\partial}{\partial \eta}\left(\left(\frac{1}{(\eta+\gamma)}\frac{\partial}{\partial \eta}\left(\left(\eta+\gamma\right)^2\left(\alpha+\left(1-\alpha\right)\left(1+We^2\Pi^2\right)^{\frac{n-1}{2}}\right)\left(\frac{1}{\eta+\gamma}\left(1-\frac{\partial \psi}{\partial \eta}\right)+\frac{\partial^2 \psi}{\partial \eta^2}\right)\right)\right.\right.\\ &\left.\left.-\frac{Ha^2\gamma}{(\eta+\gamma)}\left(1-\frac{\partial \psi}{\partial \eta}\right)\right)\right)=0. \end{aligned} \tag{5.18}$$

The dimensionless concentration equation for problem under consideration is given by Eq. (2.24). The boundary conditions associated with Eqs. (2.24), (5.17) and (5.18) are defined through Eqs. (2.27) and (2.28). The boundary value problems comprising of above mentioned equations and boundary conditions are simulated using the finite difference technique which is already elaborated in previous chapters.

5.2 Computational results and interpretation

In this section, we interpret the numerical results to highlight some significant characteristics of the peristaltic motion for example flow velocity, pumping characteristics, temperature distribution, mass concentration and trapping for different values of the factors like *Ha*, γ, *n*, *Br*, *Sr* and *We* through **Figs. 5.1** - **5.2**1.

5.2.1. Flow velocity

The axial velocity distribution for power-law index (*n*) and Hartmann number (*Ha*) is shown in **Figs. 5.1** and **5.**2, respectively. **Fig. 5.1** shows that axial velocity rises with rising *n*. For $n = 0.01$ the velocity profile is asymmetric with maximum appearing above the curve $\eta = 0$. However, for $n = 0.55$ the velocity profile approximately regain its symmetry. A further rise in *n* exhibit asymmetric velocity profile with maxima lying below $\eta = 0$. With the change in behavior of fluid from shear-thinning to shear-thickening, substantial changes in velocity are observed. In fact during this transformation of fluid the original non-symmetric velocity profile with maxima appearing above $\eta = 0$ transform to

asymmetric form with maxima lying below $\eta = 0$. During this transformation process the velocity also approximately regains its symmetric shape. The whole scenario also indicates that the role of power-law index is to counteract the effects of channel curvature. **Fig. 5.2** exhibits the effects *Ha* on $u_2(\eta)$. Here it is observed that $u_2(\eta)$ shows boundary layer nature for increasing values of *Ha*. In fact for larger values of *Ha*, the disturbance in $u_2(\eta)$ is restrained in skinny layer near both upper and lower walls. The fluid outside these boundary layers moves with linear velocity. This observation is in contrast to the previously reported results on peristaltic flows in straight channel (Wang 2008). In straight channel the fluid outside the boundary layers moves with constant velocity.

5.2.2 Pumping characteristics

The effects of index of power-law (*n*) and curvature parameter (γ) on pressure rise per wavelength (Δp) plotted against time-averaged flow rate in the laboratory frame Θ $(= f + 2)$ are presented in **Figs. 5.3** and **5.4**. The computations of pressure rise are carried out using the formula (2.29). The present analysis demonstrate three pumping regions namely peristaltic pumping region, free pumping region and co-pumping region respectively. Here it is observed that Δp rises with rising γ and *n.*

2.3 Heat transfer phenomena

The effects of viscoelastic parameter (*We*), power-law index (*n*), channel curvature (γ) and Hartmann number (*Ha*) on the temperature distribution are graphically demonstrated in **Figs. 5.5 - 5.8,** respectively. **Fig. 5.5** depicts the effects of *We* on the temperature

distribution for both shear thinning ($n < 1$) and thickening ($n > 1$) fluids. It shows that the temperature profile is a decreasing function of *We* for shear-thinning bio-fluid while reverse phenomena is observed for shear-thickening bio-fluids with increasing viscoelastic parameter *We*. **Fig 5.6** shows enhancement in the magnitude of temperature profile when behavior of fluid shifts from shear-thinning fluid to shear-thickening. In **Fig. 5.7**, the effects of curvature parameter γ are discussed. It is observed that $\theta(\eta)$ inside the channel enhances with enhancing the values of γ. Similarly **Fig. 5.8** also shows an increase in temperature inside the channel with increasing *Ha*.

Figs 5.9 - 5.13 depicts the effects of power-law index (*n*), Weissenberg number (*We*), Brinkmann number (*Br*), Hartmann number (*Ha*) and curvature of the channel (γ) on *z* at the upper wall (computed via the expression (2.31)). These figures shows oscillatory behavior of *z* due to peristaltic phenomena. The amplitude of the heat transfer coefficient decreases for shear-thinning fluid while it shows an increasing trend for shear-thickening fluids with increasing the Weissenberg number *We*. Moreover, the amplitude of heat transfer coefficient is found to decrease via increasing *n*, γ, *Br* and *Ha*.

5.2.4 Mass concentration

Figs. 5.14 - 5.17 depict the behavior of the mass concentration (ϕ) for various values of *We*, *n*, γ and *Sr*. The impact of *We* on concentration distribution is displayed in **Fig. 5.14** for two mounting values of *n*. It is noticed from **Fig. 5.14** that for shear-thinning fluids $(n < 1)$, the concentration distribution is a decreasing function of *We* while it shows reverse trend for shear-thickening fluids $(n > 1)$. It is noticed from **Fig. 5.15** that the

magnitude of mass concentration enhances when behavior of fluid shifts from shear-thinning fluid to shear-thickening. **Fig 5.16** reveals that mass concentration decreases with increasing γ. **Fig. 5.17** indicate that the magnitude of ϕ rises by rising *Sr*.

The effects of *We, n* and γ on Sherwood number (*Sh*) at the upper wall (computed via the expression (2.32)) are graphically shown in **Figs. 5.18 - 5.20**. Similar to the heat transfer coefficient the behavior of Sherwood number is also oscillatory. The amplitude of the Sherwood number (*Sh*) decreases for shear-thinning fluids while it increases for shear-thickening fluids with increasing the values of *We*. Moreover, the amplitude of Sherwood number (*Sh*) enhances via increasing *n*. In contrast a reverse trend is observed with increasing the values of curvature parameter (γ).

5.2.5 Trapping

The streamlines of the flow for different values of Hartmann number are shown in **Fig. 5.21**. A circulating bolus of fluid can be clearly identified from all four panels. It is examined that the shape of the circulating bolus is greatly influenced with increasing *Ha*. In this transformation process the bolus also regain its symmetric shape approximately for *Ha* = 0.7.

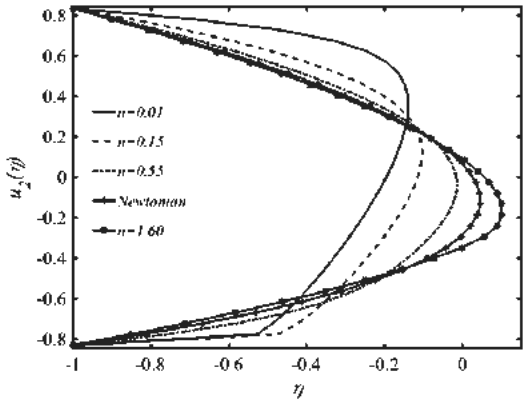

Fig. 5.1: Influence of *n* on $u_2(\eta)$ for *Ha* = 0.5, $\mu_0 = 1.3$, $\mu_\infty = 0.05$, $\Theta = 1.5$ and $\gamma = 2$.

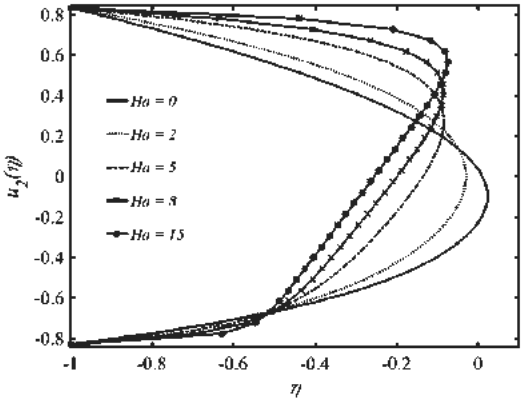

Fig. 5.2: Influence of *Ha* on $u_2(\eta)$ for *n* = 0.8, $\mu_0 = 1.3$, $\mu_\infty = 0.05$, $\Theta = 1.5$ and $\gamma = 2$.

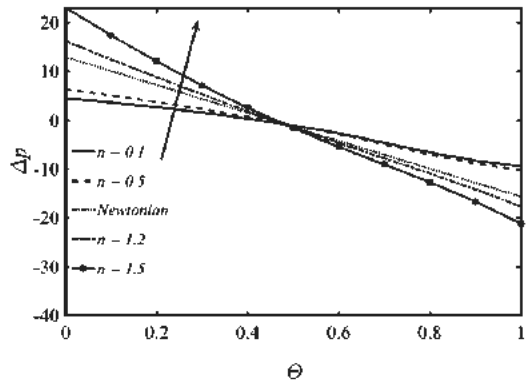

Fig. 5.3: Effect of *n* on (Δp) for $\lambda = 0.4$, *We* = 2, *Ha* = 0.2, $\Theta = 1.5$ and $\gamma = 2$.

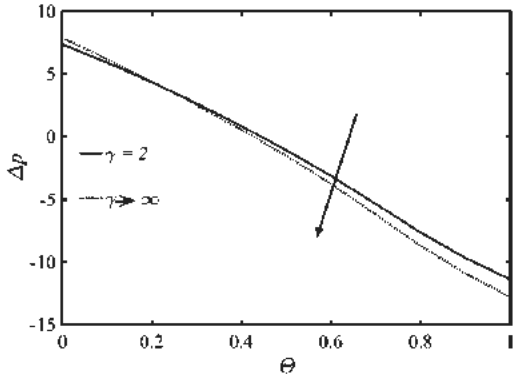

Fig.5.4: Effect of γ on (Δp) for *Ha* = *0.2*, $\lambda = 0.4$, *We* = 2, *n* = 0.4 and $\Theta = 1.5$.

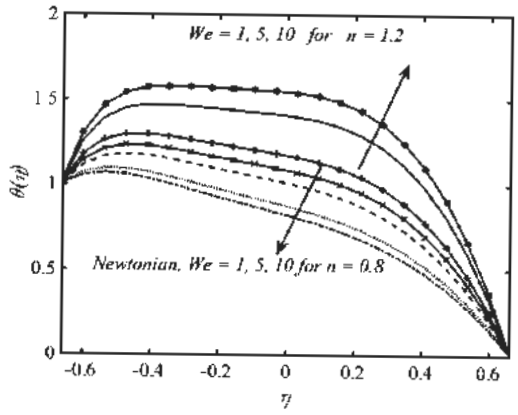

Fig. 5.5: Effect of *We* on temperature $\theta(\eta)$ for $\lambda = 0.4$, $Br = 2$, $Ha = 1$, $\gamma = 2$ and $\Theta = 1.5$.

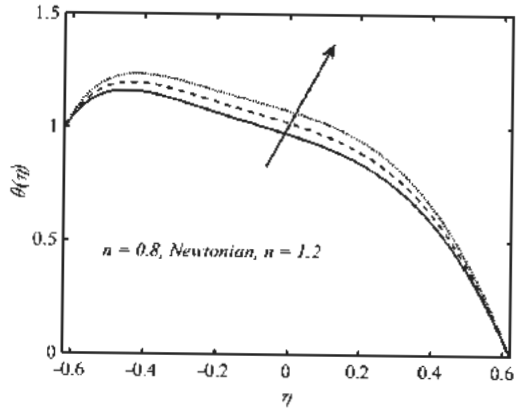

Fig. 5.6: Effect of *n* on temperature $\theta(\eta)$ for $\lambda = 0.4$, $Br = 2$, $Ha = 1$, $\Theta = 1.5$ and $\gamma = 2$.

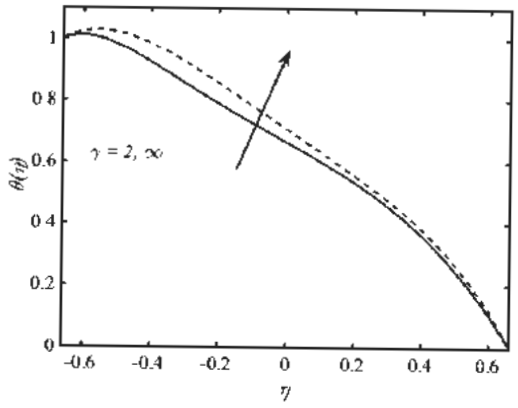

Fig. 5.7: Effect of γ on temperature $\theta(\eta)$ for $n = 0.8$, $Br = 0.5$, $Ha = 1$, $\lambda = 0.4$, and $\Theta = 1.5$.

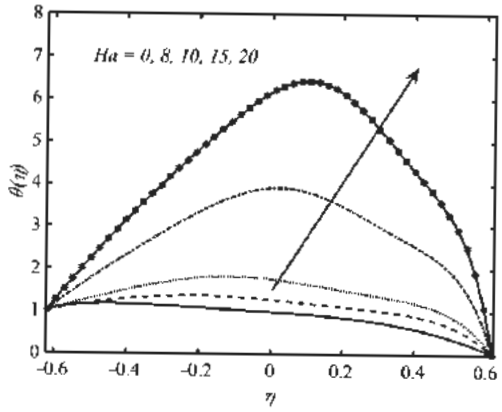

Fig. 5.8: Effect of *Ha* on temperature $\theta(\eta)$ for $n = 0.8$, $Br = 2$, $\lambda = 0.4$, $\gamma = 2$ and $\Theta = 1.5$.

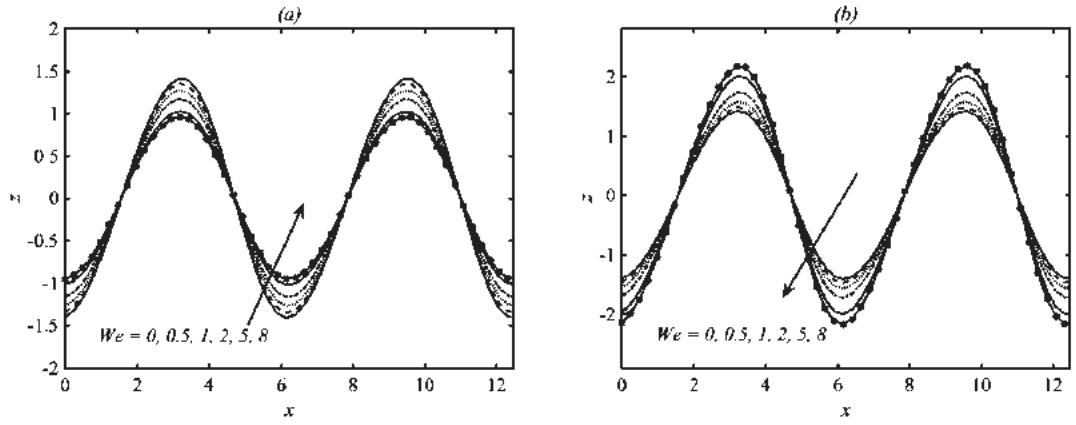

Fig. 5.9: z at upper wall for *We* with (a) n = 0.8 (shear thinning) and (b) n = 1.2 (shear thickening), with $\gamma = 2$, *Ha* = 1, *Br* = 2, $\Theta = 1.5$ and $\lambda = 0.4$.

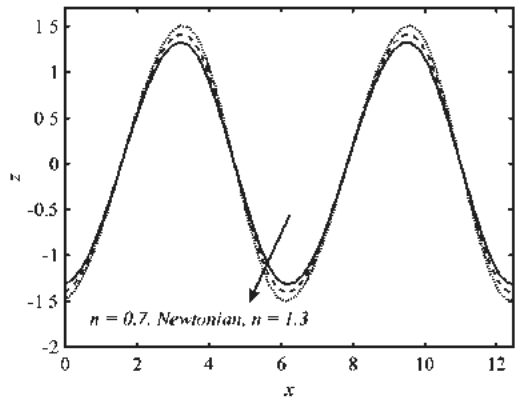

Fig. 5.10: Influence of n (power-law index) on z for *We* = 0.5, $\gamma = 2$, *Ha* = 1 and $\lambda = 0.4$.

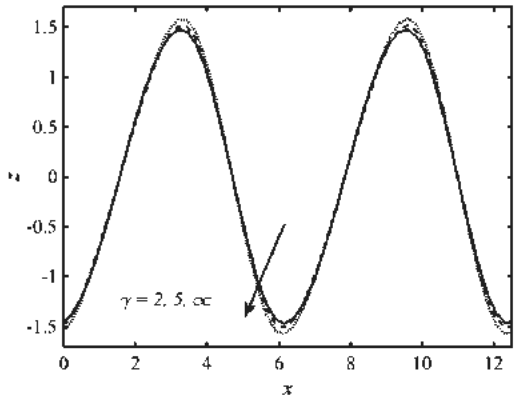

Fig. 5.11: Influence of γ (dimensionless radius of curvature) on z for n = 0.8, *Ha* = 1, $\Theta = 1.5$ and $\lambda = 0.4$.

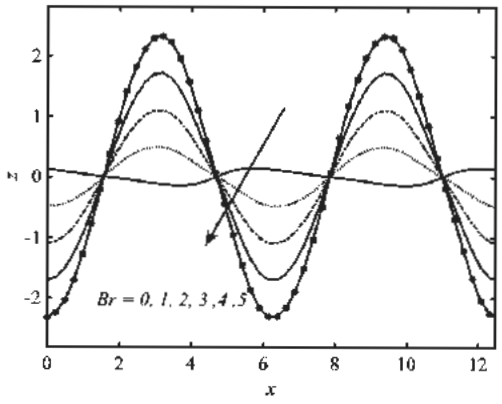

Fig. 5.12: Influence of *Br* on *z* for *We* = 0.5, $\gamma = 2$, *n* = 0.8, *Ha* = 1, $\Theta = 1.5$ and $\lambda = 0.4$.

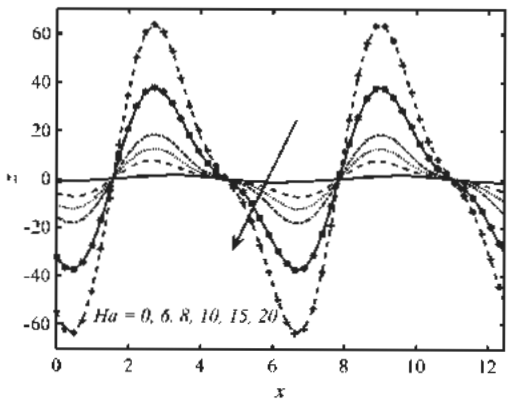

Fig. 5.13: Influence of *Ha* on *z* for *We* = 0.5, $\gamma = 2$, *n* = 0.8, *Br* = 2, $\Theta = 1.5$ and $\lambda = 0.4$.

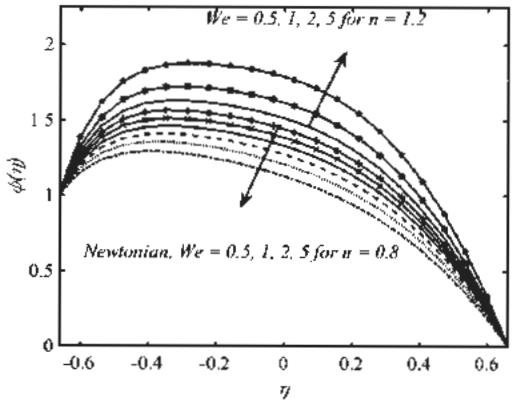

Fig.5.14: Effect of *We* on $\phi(\eta)$ for $\gamma = 2$, *Br* = 2, *Sr* = 1 and *Sc* = 1.

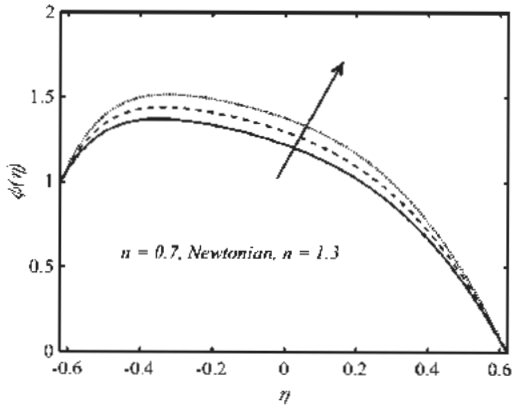

Fig. 5.15: Effect of *n* on $\phi(\eta)$ for $\gamma = 2$, *Br* = 2, *Sr* = 1 and *Sc* = 1.

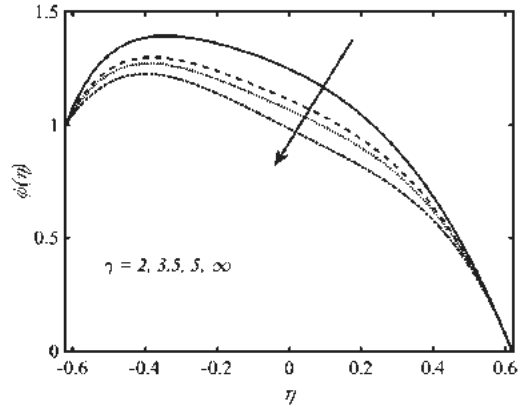

Fig. 5.16: Effect of γ on $\phi(\eta)$ for *We* = 0.5, *n* = 0.8, *Br* = 2 and $\lambda = 0.4$.

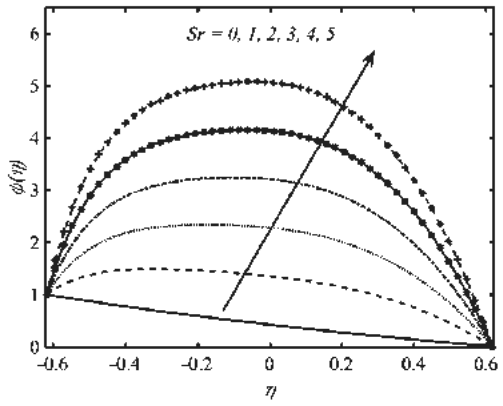

Fig. 5.17: Effect of *Sr* on $\phi(\eta)$ for *We* = 0.5, *n* = 0.8, *Br* = 2 and $\lambda = 0.4$.

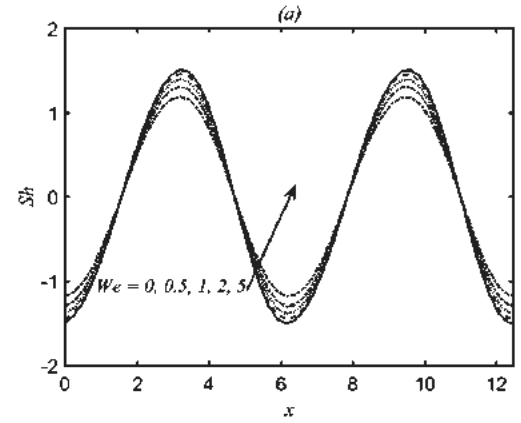

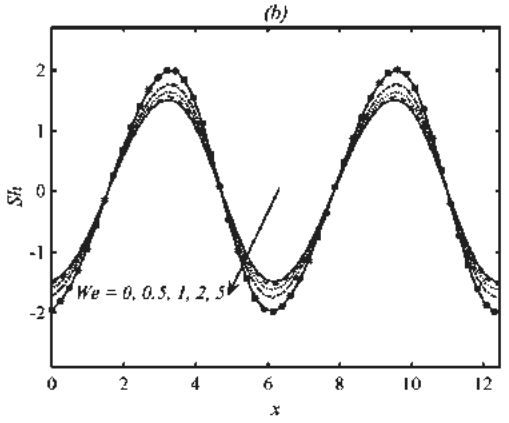

Fig. 5.18: Effect of *We* on Sherwood number *Sh* at upper wall for (a) shear thinning (*n* = 0.8) and (b) shear thickening (*n* = 1.2), with $\gamma = 2$, *Ha* = 1, *Sr* = 1, *Sc* = 1, $\Theta = 1.5$ and $\lambda = 0.4$.

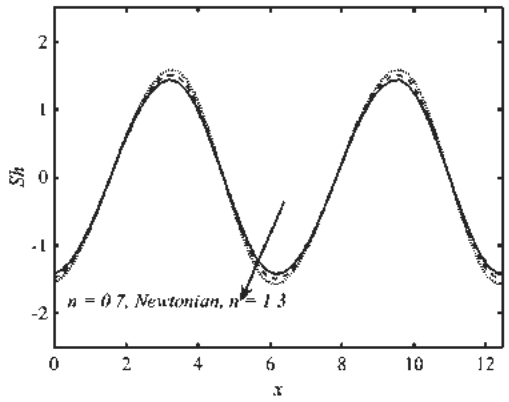

Fig. 5.19: Effect of *n* on Sherwood number *Sh* at upper wall for $\gamma = 2,$ *Ha* = 1, *Sr* = 1, $\Theta = 1.5$ and $\lambda = 0.4.$

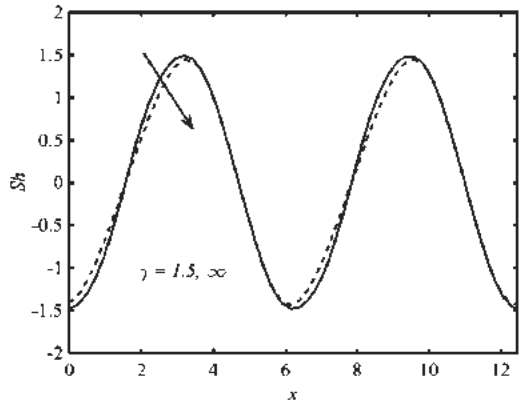

Fig. 5.20: Effect of γ on Sherwood number *Sh* at upper wall for *n* = 0.8, We $= 0.5,$ *Sr* = 1, $\Theta = 1.5$ and $\lambda = 0.4.$

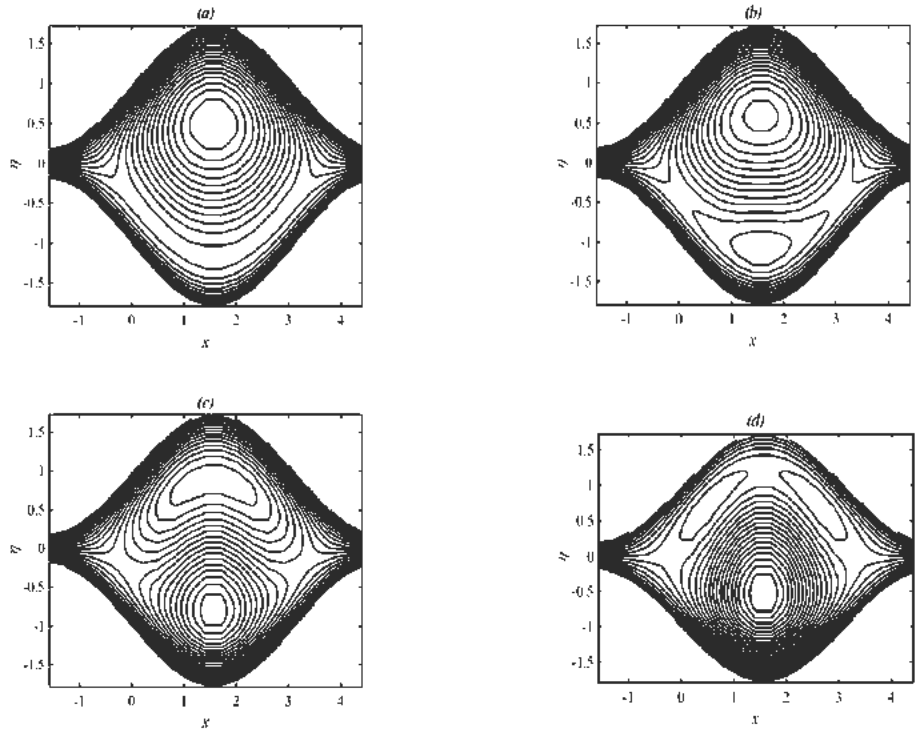

Fig. 5.21: Flow patterns for (a) *Ha* = 0.1, (b) *Ha* = 0.35, (c) *Ha* = 0.7, and (e) *Ha* = 1.3 for *n* = 0.1 using $\gamma = 2$, *We* = 0.5, $\Theta = 1.5$ and $\lambda = 0.4$.

Chapter 6

Peristaltic flow of Rabinowitsch fluid in a curved channel: Mathematical analysis

In this chapter we discussed the Rabinowitsch fluid model for the mathematical analysis of peristaltic flow with heat transfer in a curved channel. The fundamental equations of flow and heat transfer are developed using curvilinear coordinates. The set of these equations reduced by using delta approximation. The reduced set of equations is solved by semi-analytic procedure while energy equation is simulated numerically using Mathematica routine "NDSolve". The effects of curvature parameter and the coefficient of pseudoplasiticity on flow velocity, temperature and streamlines are shown in detail.

6.1 Mathematical Formulation

Let us consider a curved channel occupied with an incompressible Rabinowitsch fluid. The continuity, momentum and energy equations in components form are given by

$$\frac{\partial}{\partial R}\left\{\left(R+\tilde{R}\right)U_1\right\}+\tilde{R}\frac{\partial U_2}{\partial \chi}=0, \tag{6.1}$$

$$\begin{aligned}\rho\left[\frac{\partial U_1}{\partial t}+U_1\frac{\partial U_1}{\partial R}+\frac{RU_2}{R+\tilde{R}}\frac{\partial U_1}{\partial \chi}-\frac{{U_2}^2}{R+\tilde{R}}\right]&=-\frac{\partial P}{\partial R}+\frac{1}{R+\tilde{R}}\frac{\partial}{\partial R}\left\{\left(R+\tilde{R}\right)S_{RR}\right\}\\&+\frac{\tilde{R}}{R+\tilde{R}}\frac{\partial}{\partial \chi}S_{R\chi}-\frac{S_{\chi\chi}}{R+\tilde{R}},\end{aligned} \tag{6.2}$$

$$\rho\left[\frac{\partial U_2}{\partial t}+U_1\frac{\partial U_2}{\partial R}+\frac{\tilde{R}U_2}{R+\tilde{R}}\frac{\partial U_2}{\partial \chi}-\frac{U_2U_1}{R+\tilde{R}}\right]=-\left(\frac{\tilde{R}}{R+\tilde{R}}\right)\frac{\partial P}{\partial \chi}+\frac{1}{\left(R+\tilde{R}\right)^2}\frac{\partial}{\partial R}\left\{\left(R+\tilde{R}\right)^2 S_{R\chi}\right\}$$
$$+\frac{\tilde{R}}{R+\tilde{R}}\frac{\partial}{\partial \chi}S_{\chi\chi}, \tag{6.3}$$

$$\rho c_p\left[\frac{\partial T}{\partial t}+U_1\frac{\partial T}{\partial R}+\frac{\tilde{R}U_2}{R+\tilde{R}}\frac{\partial T}{\partial \chi}\right]=k\left(\frac{1}{\left(R+\tilde{R}\right)}\frac{\partial}{\partial R}\left\{\left(R+\tilde{R}\right)\frac{\partial T}{\partial R}\right\}+\left(\frac{\tilde{R}}{R+\tilde{R}}\right)^2\frac{\partial^2 T}{\partial \chi^2}\right)+$$
$$S_{RR}\frac{\partial U_1}{\partial R}+S_{R\chi}\left(\frac{\partial U_2}{\partial R}+\frac{\tilde{R}}{R+\tilde{R}}\frac{\partial U_1}{\partial \chi}+\frac{\tilde{R}}{R+\tilde{R}}\frac{\partial U_2}{\partial \chi}-\frac{U_2}{R+\tilde{R}}\right)+S_{\chi\chi}\left(\frac{U_1}{R+\tilde{R}}+\frac{\tilde{R}}{R+\tilde{R}}\frac{\partial U_2}{\partial \chi}\right). \tag{6.4}$$

According to Robinowitsch model the empirical stress-strain relations in component form are:

$$S_{RR}=2\mu\frac{\partial U_1}{\partial R}, \tag{6.5}$$

$$S_{R\chi}+\alpha'\left(S_{R\chi}\right)^3=\mu\left(\left(\frac{\tilde{R}}{R+\tilde{R}}\right)\frac{\partial U_1}{\partial \chi}+\left(R+\tilde{R}\right)\frac{\partial}{\partial R}\left(\frac{U_2}{R+\tilde{R}}\right)\right), \tag{6.6}$$

$$S_{\chi\chi}=2\mu\left(\left(\frac{\tilde{R}}{R+\tilde{R}}\right)\frac{\partial U_2}{\partial \chi}+\frac{U_1}{R+\tilde{R}}\right), \tag{6.7}$$

where α' is the non-linear factor responsible for the non-Newtonian effects. By adopting the same procedure as described in chapter 4, Eqs. (6.2)- (6.7) are reduced to following form:

$$\frac{\partial p}{\partial \eta}=0, \tag{6.8}$$

$$-\frac{\partial p}{\partial x}+\frac{1}{\gamma\left(\eta+\gamma\right)}\frac{\partial}{\partial\eta}\left\{\left(\eta+\gamma\right)^{2}S_{\eta x}\right\}=0, \tag{6.9}$$

$$\frac{1}{(\eta+\gamma)}\frac{\partial}{\partial\eta}\left(\left(\eta+\gamma\right)\frac{\partial\theta}{\partial\eta}\right)+BrS_{\eta x}\left(-\frac{1}{\eta+\gamma}\left(1-\frac{\partial\psi}{\partial\eta}\right)-\frac{\partial^{2}\psi}{\partial\eta^{2}}\right)=0, \tag{6.10}$$

$$S_{xx}=0, \tag{6.11}$$

$$S_{\eta x}+\beta'\left(S_{\eta x}\right)^{3}=\frac{\partial u}{\partial\eta}-\frac{\left(u+1\right)}{\eta+\gamma}, \tag{6.12}$$

$$S_{\eta\eta}=0, \tag{6.13}$$

where $\beta'=\dfrac{\alpha'\mu^{2}c^{2}}{a^{2}}$.

Adopting the stream function formulation through the Eq. (2.25), Eq. (6.12) becomes

$$S_{\eta x}+\beta' {S_{\eta x}}^{3}=-\frac{\partial^{2}\psi}{\partial\eta^{2}}-\frac{1}{\eta+\gamma}\left(1-\frac{\partial\psi}{\partial\eta}\right). \tag{6.14}$$

Eliminating $S_{\eta x}$ between (6.9) and (6.14) and integrating twice we get

$$\begin{aligned}\psi=c_{3}+\frac{1}{192}\Bigg(&192\eta-\frac{1}{\left(\eta+\gamma\right)^{4}}\left(2c_{1}-\gamma^{3}\frac{\partial p}{\partial x}\right)^{3}-\frac{9\gamma\beta'}{\left(\eta+\gamma\right)^{2}}\frac{\partial p}{\partial x}\left(-2c_{1}+\gamma^{3}\frac{\partial p}{\partial x}\right)^{2}+\\&6\left(\eta+\gamma\right)^{2}\left(-16c_{2}+4\gamma\frac{\partial p}{\partial x}+\gamma^{3}\left(\frac{\partial p}{\partial x}\right)^{2}\beta'\right)-12\gamma\frac{\partial p}{\partial x}\left(\eta+\gamma\right)^{2}\left(4+\gamma^{2}\left(\frac{\partial p}{\partial x}\right)^{2}\beta'\right)\\&\ln\left[\eta+\gamma\right]+12\left(2c_{1}-\gamma^{3}\frac{\partial p}{\partial x}\right)\left(4+3\gamma^{2}\left(\frac{\partial p}{\partial x}\right)^{2}\beta'\right)\ln\left[\eta+\gamma\right]\Bigg)\Bigg).\end{aligned} \tag{6.15}$$

The appropriate boundary conditions in terms of stream function are:

$$\psi = -\frac{q}{2},\ \frac{\partial \psi}{\partial \eta} = 1,\ \theta = 0,\ \text{at}\ \ \eta = h_1 = 1 + \lambda \sin x, \tag{6.16}$$

$$\psi = \frac{q}{2},\ \frac{\partial \psi}{\partial \eta} = 1,\ \theta = 1,\ \text{at}\ \ \eta = h_2 = -1 - \lambda' \sin x. \tag{6.17}$$

The boundary conditions (6.16) and (6.17) yields the following transcendental algebraic equations in terms of unknown c_1, c_2, c_3 and $\partial p/\partial x$.

$$\begin{aligned} 0 = -\left(h_1+\gamma\right)\Bigg(& c_2 + \frac{1}{96}\Bigg(-\frac{2\beta'}{\left(h_1+\gamma\right)^6}\left(2c_1 - \gamma^3\frac{\partial p}{\partial x}\right)^3 - \frac{9\gamma\beta'}{\left(h_1+\gamma\right)^4}\frac{\partial p}{\partial x}\left(-2c_1+\gamma^3\frac{\partial p}{\partial x}\right)^2 + \\ & \frac{6}{\left(h_1+\gamma\right)^2}\left(-2c_1+\gamma^3\frac{\partial p}{\partial x}\right)\left(4+3\gamma^2\left(\frac{\partial p}{\partial x}\right)^2\beta'\right) + 12\gamma\frac{\partial p}{\partial x}\beta'\left(4+3\gamma^2\left(\frac{\partial p}{\partial x}\right)^2\beta'\right)\ln\left[h_1+\gamma\right]\Bigg)\Bigg), \end{aligned} \tag{6.18}$$

$$\begin{aligned} 0 = -\left(h_2+\gamma\right)\Bigg(& c_2 + \frac{1}{96}\Bigg(-\frac{2\beta'}{\left(h_2+\gamma\right)^6}\left(2c_1 - \gamma^3\frac{\partial p}{\partial x}\right)^3 - \frac{9\gamma\beta'}{\left(h_2+\gamma\right)^4}\frac{\partial p}{\partial x}\left(-2c_1+\gamma^3\frac{\partial p}{\partial x}\right)^2 + \\ & \frac{6}{\left(h_2+\gamma\right)^2}\left(-2c_1+\gamma^3\frac{\partial p}{\partial x}\right)\left(4+3\gamma^2\left(\frac{\partial p}{\partial x}\right)^2\beta'\right) + 12\gamma\frac{\partial p}{\partial x}\beta'\left(4+3\gamma^2\left(\frac{\partial p}{\partial x}\right)^2\beta'\right)\ln\left[h_2+\gamma\right]\Bigg)\Bigg), \end{aligned} \tag{6.19}$$

$$\begin{aligned} -\frac{\Theta}{2} = c_3 + \frac{1}{192}\Bigg(& 192h_1 - \frac{1}{\left(h_1+\gamma\right)^4}\left(2c_1-\gamma^3\frac{\partial p}{\partial x}\right)^3 - \frac{9\gamma\beta'}{\left(h_1+\gamma\right)^2}\frac{\partial p}{\partial x}\left(-2c_1+\gamma^3\frac{\partial p}{\partial x}\right)^2 + \\ & 6\left(h_1+\gamma\right)^2\left(-16c_2+4\gamma\frac{\partial p}{\partial x}+\gamma^3\left(\frac{\partial p}{\partial x}\right)^2\beta'\right) - 12\gamma\frac{\partial p}{\partial x}\left(h_1+\gamma\right)^2\left(4+\gamma^2\left(\frac{\partial p}{\partial x}\right)^2\beta'\right)\ln\left[h_1+\gamma\right] \\ & +12\left(2c_1-\gamma^3\frac{\partial p}{\partial x}\right)\left(4+3\gamma^2\left(\frac{\partial p}{\partial x}\right)^2\beta'\right)\ln\left[h_1+\gamma\right]\Bigg), \end{aligned} \tag{6.20}$$

$$\begin{aligned} \frac{\Theta}{2} = c_3 + \frac{1}{192}\Bigg(& 192h_2 - \frac{1}{\left(h_2+\gamma\right)^4}\left(2c_1-\gamma^3\frac{\partial p}{\partial x}\right)^3 - \frac{9\gamma\beta'}{\left(h_2+\gamma\right)^2}\frac{\partial p}{\partial x}\left(-2c_1+\gamma^3\frac{\partial p}{\partial x}\right)^2 + \\ & 6\left(h_2+\gamma\right)^2\left(-16c_2+4\gamma\frac{\partial p}{\partial x}+\gamma^3\left(\frac{\partial p}{\partial x}\right)^2\beta'\right) - 12\gamma\frac{\partial p}{\partial x}\left(h_2+\gamma\right)^2\left(4+\gamma^2\left(\frac{\partial p}{\partial x}\right)^2\beta'\right) \\ & \ln\left[h_2+\gamma\right] + 12\left(2c_1-\gamma^3\frac{\partial p}{\partial x}\right)\left(4+3\gamma^2\left(\frac{\partial p}{\partial x}\right)^2\beta'\right)\ln\left[h_2+\gamma\right]\Bigg). \end{aligned} \tag{6.21}$$

The above equations can be solved for c_1, c_2, c_3 and $\partial p/\partial s$ using any symbolic software such as Mathematica or Maple at each cross-section $x \in [0, 2\pi]$ for specific values of involved parameters. In this way solution at each cross-section can be determined as an explicit function of η. The pressure rise can be obtained through the formula (2.30). The semi-analytical approach used to calculate stream function is not suitable to compute the temperature field due to complicated non-homogenous term. Therefore, temperature is computed numerically using Mathematica routine "NDSolve".

6.2 Results and discussion

The results of computations are displayed in terms of velocity profiles, pressure rise per wavelength profiles, temperature profiles and streamlines contours for different values of coefficient of pseudoplasiticity (β'), Brinkmann number (*Br*) and curvature parameter (γ) through **Figs. 6.1 - 6.7**.

The axial velocity profiles for some specific values of the coefficient of curvature parameter (γ) and coefficient of pseudoplasiticity (β') are shown in **Figs. 6.1** and **6.2**, respectively. It is observed through **Fig. 6.1(a)** that for negative values of β', the velocity achieves maximum above $\eta = 0$ while for positive value the maximum appears below $\eta = 0$. The flow velocity becomes symmetric as $\gamma \to \infty$. **Fig. 6.2** shows the effects of coefficient of pseudoplasiticity on the flow velocity. It is noticed that the $u_2(\eta)$ tends to achieve symmetric profile with increasing β' values from negative to positive.

Figs. 6.3 and **6.4** are designed to analyze the effect of β' and *Br* on the radial distribution of temperature of fluid inside the channel. It is examined that $\theta(\eta)$ enhances by enhancing β' and Br.

The streamlines of flow inside the channel for various values of coefficient of pseudoplasiticity (β') and curvature parameter (γ) are plotted in **Figs. 6.5 - 6.7,** respectively. **Fig. 6.5** shows an asymmetric fluid bolus for which upper part is bigger in size than the lower one for β' = 0. The area of lower part is decreased with increasing β' to 0.1. A further increase in β' results in a low intensity lower part with a substantially decreases area. The lower part eventually vanishes when β' takes the value 15. The area of upper part also decreases with increasing β' from 0 to 15. **Figs. 6.6** and **6.7** show the effect of curvature parameter (γ) on streamlines for $\beta' = -0.005$ (Dilatant Fluid) and $\beta' = 0.1$ (Pseudoplastic Fluid), respectively. It is observed through both figures that streamlines are asymmetric with respect to central plane for smaller values of γ. However, streamlines regain their symmetry as one shifts form curved to straighter channel (i.e., as $\gamma \to \infty$) regardless of the choice of β'. It is important to mention that these results of streamlines are also consistent with the results reported by Sato et al. (2000), Ramanamurthy et al. (2013), and Narla et al. (2015).

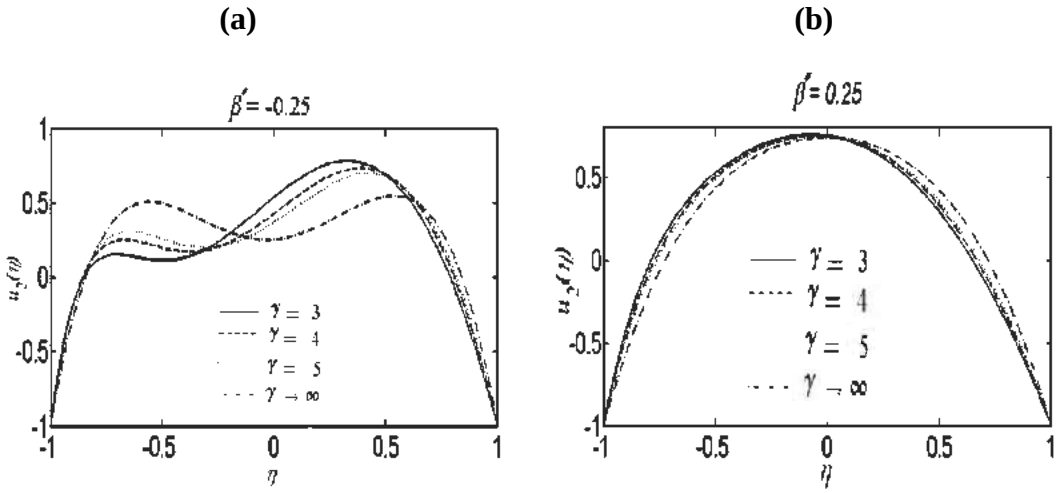

Fig. 6.1: Effect of γ on velocity $u_2(\eta)$ for two different values of β' $(\beta' > 0$ $(Pseudoplastic\ Fluid), and\ \beta' < 0$ $(Dilatant\ Fluid))$, with $\lambda = 0.4$ and $\Theta = 0.5$.

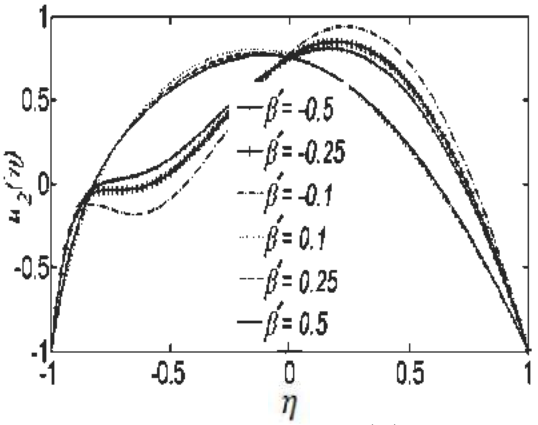

Fig. 6.2: Effect of β' on velocity $u_2(\eta)$ for $\lambda = 0.4$ and $\Theta = 0.5$.

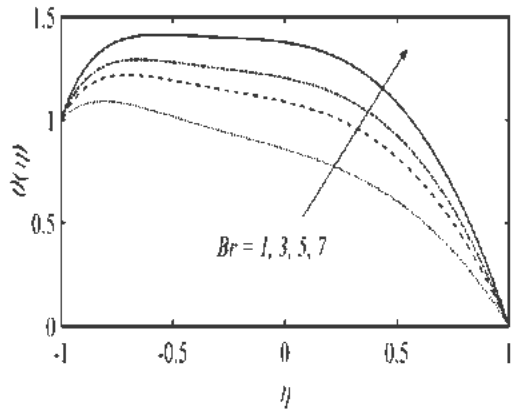

Fig. 6.3: Effect of *Br* on temperature $\theta(\eta)$ for $\lambda = 0.4$, β' =0.5 and $\gamma = 2$.

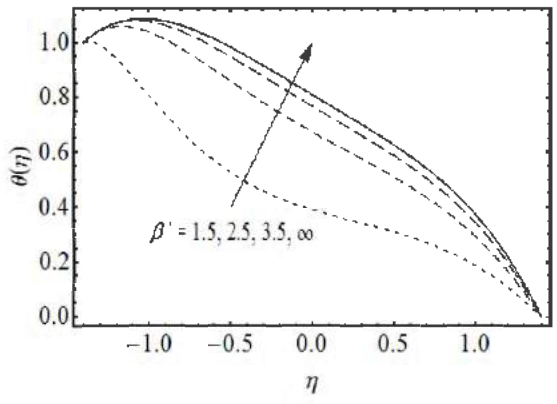

Fig. 6.4: Effect of β' on temperature $\theta(\eta)$ for *Br* = 0.5, $\lambda = 0.4$ and $\gamma = 2$.

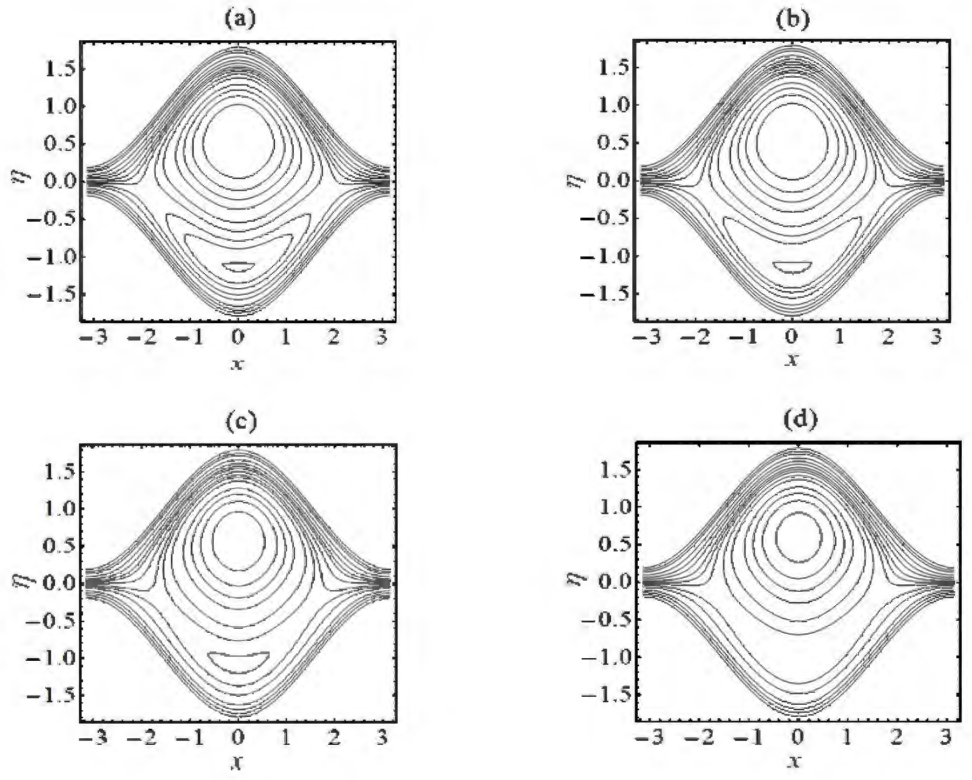

Fig. 6.5: Flow patterns for (Pseudoplastic Fluid) (a) β' = 0 (Newtonian), (b) β' = 0.1, (c) β' = 5 and (d) β' = 15. The other parameters chosen are $\lambda = 0.8, \Theta = 1.5$ and γ = 2.

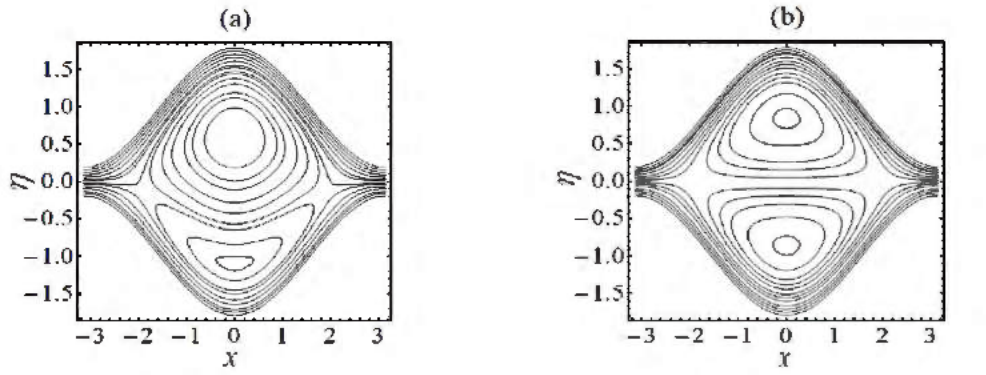

Fig. 6.6: Flow patterns for (a) $\gamma = 3.5$ and (b) $\gamma \to \infty$. The other parameters chosen are $\lambda = 0.8, \Theta = 1.5$ and $\beta' = -0.005$ (Dilatant Fluid).

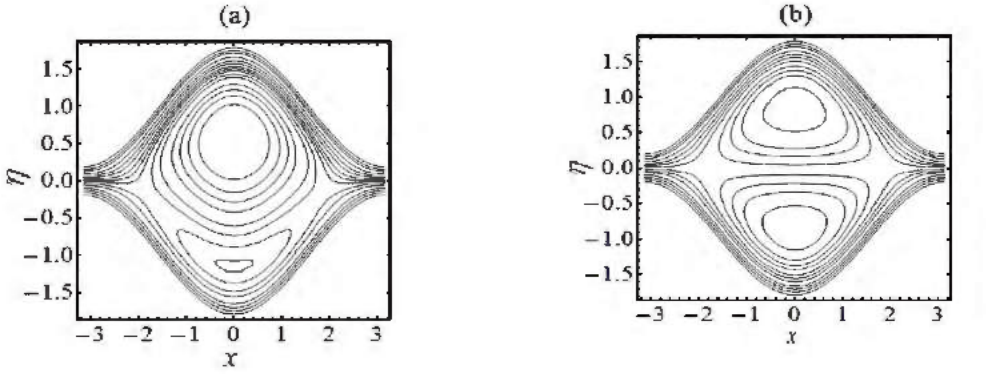

Fig. 6.7: Flow patterns for (a) $\gamma = 3.5$ and (b) $\gamma \to \infty$. The other parameters chosen are $\lambda = 0.8, \Theta = 1.5$ and $\beta' = 0.1$ (Pseudoplastic Fluid).

Chapter 7

Micro structural effects on heat and mass transfer in peristaltic flow through a curved channel

This chapter is prepared to investigate the effect of heat and mass transfer on magnetically influenced micropolar flow induced by peristaltic waves. The equations describing the flow and heat/ mass transfer are developed using curvilinear coordinates. A reduction of these equations is made based on delta approximation. Implicit finite difference scheme is employed to solve the set of reduced linear ordinary differential equations. The effects of coupling number, micropolar parameter, Hartmann number, Brinkmann number, rate of chemical reaction and curvature parameter on longitudinal velocity, pressure rise, temperature and mass concentration are analyzed in detail. The flow patterns in the channel illustrating the effects of several involved parameter are also displayed.

7.1 Governing equations

For micropolar fluid, the equations governing the flow, heat and mass transfer in tensor notation are given by

Continuity Equation: $$U_{i,i} = 0, \tag{7.1}$$

Momentum Equation: $$\rho \dot{U}_k = \tau_{lk,l} + \rho f_k, \tag{7.2}$$

Moment of momentum Equation: $\rho j \dot{w}_k = m_{lk,l} + e_{kij}\tau_{ij},$ (7.3)

Energy Equation: $\rho c_p \dot{T} = kT_{,ii} + \tau_{kl}a_{kl} - m_{kl}b_{kl},$ (7.4)

Concentration Equation: $\dot{C} = DC_{,ii} + \frac{Dk_T}{T_m}T_{,ii} - k_1 C.$ (7.5)

In above equations U_k is the velocity, w_k is the micro-rotation vector, f_k is the body force, τ_{kl} is the Cauchy stress tensor, m_{kl} is the moment stress tensor, k_1 is the rate of chemical reaction, j is micro moment of inertia and dot indicates the material time derivative. Moreover, $\tau_{kl}, m_{kl}, a_{kl}$ and b_{kl} are given by

$$\left.\begin{aligned} \tau_{kl} &= -p\delta_{kl} + (\mu + k_2)a_{kl} + \mu a_{lk}, \\ m_{kl} &= \alpha^* tr(b_{mm})\delta_{kl} + \beta^* b_{kl} + \gamma^* b_{lk}, \\ a_{kl} &= v_{l,k} + e_{lkm}w_m, \\ b_{kl} &= w_{k,l}, \end{aligned}\right\} \quad (7.6)$$

where k_2 is the dynamic microrotation viscosity, e_{lkm} is the permutation symbol and $\alpha^*, \beta^*, \gamma^*$ are the constants called coefficient of angular viscosity. It is important to mention here that if $k_2 = \alpha^* = \beta^* = \gamma^* = 0$, then w_k becomes zero and Eq. (7.2) reduces to Navier-Stokes equations. According to Eringen (1964) $\mu, k_2, \alpha^*, \beta^*$ and γ^* must satisfy the following inequalities:

$$2\mu + k_2 \geq 0, k_2 \geq 0, 3\alpha^* + \beta^* + \gamma^* \geq 0, \alpha^* \geq \left|\beta^*\right|. \quad (7.7)$$

7.2 Mathematical Modeling

Consider an incompressible hydromagnetic micropolar fluid flows inside the channel. The flow is generated due to the sinusoidal deformation of the channel walls. The geometry and coordinate system are illustrated in **Fig. 2.1**. The magnetic field is defined by Eq. (2.7). Thus by generalized Ohm's law the body force term in Eq. (7.2) becomes

$$\rho f_k = (\mathbf{J}\times\mathbf{B})_k, \tag{7.8}$$

where $\mathbf{J}=\sigma(\mathbf{V}\times\mathbf{B})$. Here, we neglected the electric field and invoked the low magnetic Reynolds number assumption. Using the velocity, temperature, concentration and microrotation fields defined by Eq. (2.11), the set of Eqs. (7.1) - (7.5) in component form become;

$$\frac{\partial}{\partial R}\left\{\left(R+\tilde{R}\right)U_1\right\}+\tilde{R}\frac{\partial U_2}{\partial \chi}=0, \tag{7.9}$$

$$\frac{\partial U_1}{\partial t}+(U_1.\nabla)U_1-\frac{U_2^{\,2}}{R+\tilde{R}}=-\frac{1}{\rho}\frac{\partial P}{\partial R}+\frac{1}{\rho}\left(\mu+k_2\right)\left[\nabla^2U_1-\frac{U_1}{\left(R+\tilde{R}\right)^2}-\frac{2\tilde{R}}{\left(R+\tilde{R}\right)^2}\frac{\partial U_2}{\partial \chi}\right]+\frac{k_2\tilde{R}}{\rho\left(R+\tilde{R}\right)}\frac{\partial w}{\partial \chi}, \tag{7.10}$$

$$\frac{\partial U_2}{\partial t}+(U_1.\nabla)U_2+\frac{U_1U_2}{R+\tilde{R}}=-\frac{\tilde{R}}{\rho\left(R+\tilde{R}\right)}\frac{\partial P}{\partial \chi}+\frac{1}{\rho}\left(\mu+k_2\right)\left[\nabla^2U_2-\frac{U_2}{\left(R+\tilde{R}\right)^2}+\frac{2\tilde{R}}{\left(R+\tilde{R}\right)^2}\frac{\partial U_1}{\partial \chi}\right]-\frac{k_2}{\rho}\frac{\partial w}{\partial R}$$

$$-\frac{\sigma B^{*2}\tilde{R}^2}{\rho\left(R+\tilde{R}\right)^2}U_2, \tag{7.11}$$

$$\left(U_1.\nabla\right)w=-\frac{\gamma^*}{\rho j}\left[\frac{\partial^2 w}{\partial R^2}+\frac{1}{R+\tilde{R}}\frac{\partial w}{\partial R}+\left(\frac{\tilde{R}}{R+\tilde{R}}\right)^2\frac{\partial^2 w}{\partial \chi^2}\right]+\frac{k_2}{\rho j}\left[2w-\frac{\tilde{R}}{R+\tilde{R}}\frac{\partial U_1}{\partial \chi}+\frac{\partial U_2}{\partial R}+\frac{U_2}{R+\tilde{R}}\right], \tag{7.12}$$

$$\rho c_p\left(\frac{\partial T}{\partial t}+U_1\frac{\partial T}{\partial R}+\frac{U_2\tilde{R}}{R+\tilde{R}}\frac{\partial T}{\partial \chi}\right)=k\left(\frac{\partial^2 T}{\partial R^2}+\frac{1}{R+\tilde{R}}\frac{\partial T}{\partial R}+\frac{\tilde{R}^2}{\left(R+\tilde{R}\right)^2}\frac{\partial^2 T}{\partial \chi^2}\right)+$$

$$\frac{\partial U_1}{\partial R}\left(-p+2\mu\frac{\partial U_1}{\partial R}+k_2\frac{\partial U_1}{\partial R}\right)+\left(\frac{\tilde{R}}{R+\tilde{R}}\frac{\partial U_1}{\partial \chi}-\frac{U_2}{R+\tilde{R}}-w\right)\left(\frac{\mu\tilde{R}}{R+\tilde{R}}\frac{\partial U_1}{\partial \chi}+\right.$$

$$\mu\frac{\partial U_2}{\partial R}-\frac{\mu U_2}{R+\tilde{R}}+\frac{k\tilde{R}}{R+\tilde{R}}\frac{\partial U_1}{\partial \chi}-\frac{kU_2}{R+\tilde{R}}-k_2 w\Big)+\left(\frac{\partial U_2}{\partial R}+w\right)\left(\frac{\mu\tilde{R}}{R+\tilde{R}}\frac{\partial U_1}{\partial \chi}+\right. \tag{7.13}$$

$$\mu\frac{\partial U_2}{\partial R}-\frac{\mu U_2}{R+\tilde{R}}+k_2\frac{\partial U_2}{\partial R}+k_2 w\Big)+\left(\frac{\tilde{R}}{R+\tilde{R}}\frac{\partial U_2}{\partial \chi}+\frac{U_1}{R+\tilde{R}}\right)\left(-p+\frac{2\mu\tilde{R}}{R+\tilde{R}}\frac{\partial U_2}{\partial \chi}+\right.$$

$$\left.\frac{2\mu U_1}{R+\tilde{R}}+\frac{k\tilde{R}}{R+\tilde{R}}\frac{\partial U_2}{\partial \chi}+\frac{kU_1}{R+\tilde{R}}\right)+\gamma^*\left(\left(\frac{\partial w}{\partial R}\right)^2+\left(\frac{\tilde{R}}{R+\tilde{R}}\frac{\partial w}{\partial \chi}\right)^2\right),$$

$$\frac{\partial C}{\partial t}+(U_1.\nabla)C=D\nabla^2 C+\frac{D\,K_T}{T_m}\left(\frac{\partial^2 T}{\partial R^2}+\frac{\tilde{R}}{R+\tilde{R}}\frac{\partial T}{\partial R}+\left(\frac{\tilde{R}}{R+\tilde{R}}\right)^2\frac{\partial^2 T}{\partial \chi^2}\right)-k_1 C, \tag{7.14}$$

where

$$U_1.\nabla=U_1\frac{\partial}{\partial R}+\frac{\tilde{R}U_2}{R+\tilde{R}}\frac{\partial}{\partial \chi}, \tag{7.15}$$

$$\nabla^2=\frac{1}{R+\tilde{R}}\frac{\partial}{\partial R}\left\{\left(R+\tilde{R}\right)\frac{\partial}{\partial R}\right\}+\left(\frac{\tilde{R}}{R+\tilde{R}}\right)^2\frac{\partial^2}{\partial \chi^2}. \tag{7.16}$$

The boundary conditions associated with Eqs. (7.9) - (7.14) are Eqs. (2.17) and (2.18).

After making use of transformation given by Eq. (2.19), the governing equations are obtained in the wave frame. These equations after defining the dimensionless variables

$$\theta=\left(T-T_1\right)\Big/\left(T_0-T_1\right),\ \phi=\left(C-C_1\right)\Big/\left(C_0-C_1\right),\ \overline{J}=j\Big/a^2,\ N_1=k_2\Big/\mu,\ N_2=\gamma^*\Big/a^2\mu,$$

and invoking the lubrication approximations ($\delta\approx 0, \mathrm{Re}\approx 0$) reduce to

$$\frac{\partial p}{\partial \eta} = 0, \tag{7.17}$$

$$-\frac{\partial p}{\partial x} - \frac{1}{\gamma(1-N_1)}\left[\frac{\partial}{\partial \eta}\left\{(\eta+\gamma)\frac{\partial^2 \psi}{\partial \eta^2}\right\} + \frac{1}{\eta+\gamma}\left(1-\frac{\partial \psi}{\partial \eta}\right) - N_1(\eta+\gamma)\frac{\partial w}{\partial \eta}\right] - \frac{\gamma Ha^2}{\eta+\gamma}\left(1-\frac{\partial \psi}{\partial \eta}\right) = 0, \tag{7.18}$$

$$\left(\frac{2-N_1}{N_2}\right)\left[\frac{\partial^2 w}{\partial \eta^2} + \frac{1}{\eta+\gamma}\frac{\partial w}{\partial \eta}\right] - 2w + \frac{\partial^2 \psi}{\partial \eta^2} - \frac{1}{\eta+\gamma}\left(1-\frac{\partial \psi}{\partial \eta}\right) = 0, \tag{7.19}$$

$$\begin{aligned}&\frac{\partial^2 \theta}{\partial \eta^2} + \frac{1}{(\eta+\gamma)}\frac{\partial \theta}{\partial \eta} + Br\left(\frac{1}{\eta+\gamma}\left(1-\frac{\partial \psi}{\partial \eta}\right) + w\right)\left(\frac{\partial^2 \psi}{\partial \eta^2} + \frac{1}{\eta+\gamma}\left(1-\frac{\partial \psi}{\partial \eta}\right)(1+N_1) + N_1 w\right) + \\ &Br\left(\frac{\partial^2 \psi}{\partial \eta^2} - w\right)\left(\frac{\partial^2 \psi}{\partial \eta^2} + \frac{1}{\eta+\gamma}\left(1-\frac{\partial \psi}{\partial \eta}\right) + N_1\left(\frac{\partial^2 \psi}{\partial \eta^2} - w\right)\right) + N_2 Br\left(\frac{\partial w}{\partial \eta}\right)^2 = 0,\end{aligned} \tag{7.20}$$

$$\frac{\partial^2 \phi}{\partial \eta^2} + \frac{1}{(\eta+\gamma)}\frac{\partial \phi}{\partial \eta} - R_c\phi = -SrSc\left(\frac{\partial^2 \theta}{\partial \eta^2} + \frac{1}{(\eta+\gamma)}\frac{\partial \theta}{\partial \eta}\right) + R_c. \tag{7.21}$$

Here N_1, N_2 and R_c denote the coupling number, the micropolar parameter and the dimensionless rate of chemical reaction parameter, respectively.

Combining Eq. (7.17) with Eq. (7.18), one gets

$$\frac{1}{1-N_1}\left[\frac{\partial^2}{\partial \eta^2}\left\{(\eta+\gamma)\frac{\partial^2 \psi}{\partial \eta^2}\right\} + \frac{\partial}{\partial \eta}\left(\frac{1}{\eta+\gamma}\left(1-\frac{\partial \psi}{\partial \eta}\right)\right) - N_1\frac{\partial}{\partial \eta}\left((\eta+\gamma)\frac{\partial w}{\partial \eta}\right)\right] - \frac{\gamma^2 Ha^2}{\eta+\gamma}\left(1-\frac{\partial \psi}{\partial \eta}\right) = 0. \tag{7.22}$$

Eqs. (7.19)- (7.22) are solved subject to the subsequent boundary conditions.

$$\psi = -\frac{q}{2}, \frac{\partial \psi}{\partial \eta} = 1, w = 0, \theta = 0, \phi = 0, \text{ at } \eta = h_1 = 1 + \lambda \sin x, \tag{7.23}$$

$$\psi = \frac{q}{2},\ \frac{\partial \psi}{\partial \eta} = 1, w = 0,\ \theta = 1,\ \phi = 1,\ \text{at}\ \ \eta = h_2 = -1 - \lambda \sin x. \tag{7.24}$$

The physical quantities of interest such as pressure rise per wavelength and heat transfer coefficients at both the wall $z_i (i = 1, 2)$ are defined by Eqs. (2.30) and (2.31), respectively. In summary, we have to solve Eqs. (7.19), (7.20), (7.21) and (7.22) subject to boundary conditions (7.23) and (7.24). An implicit finite difference technique is employed for the solution. For details of the method the reader is referred to section (2.2) of chapter 2.

7.3 Results and Discussion

The computations carried out using the above-mentioned method are displayed in terms of velocity profiles, pressure rise per wavelength profiles, temperature and concentration profiles, streamlines contours and heat transfer coefficient for different values of coupling number (N_1), micropolar parameter (N_2), Brinkman number (Br), Hartmann number (*Ha*) and curvature parameter (γ), we interpret the graphical results provided in **Figs. 7.1 - 7.24**.

The effects of micropolar parameter (N_2), Hartmann number (*Ha*) and coupling number (N_1) on axial velocity $u_2(\eta)$ and micro rotation $w(\eta)$ are shown through **Figs. 7.1-7.6**. **Fig. 7.1** shows that $u_2(\eta)$ increases with increasing *Ha* in the upper half of the channel while reverse trend is noticed in the lower half. **Fig. 7.2** exhibits the effect of Hartmann number (*Ha*) on micro rotation $w(\eta)$. It is noticed that $w(\eta)$ rises with rising *Ha* in lower

half of the channel while its behavior is reversed in the upper half. The decrease in velocity with increasing *Ha* in lower part of the channel is attributed to the resistive nature of the Lorentz force due to applied magnetic field. In order to maintain the prescribed flux the velocity increases with increasing *Ha* in upper part of the channel. **Fig. 7.3** shows the effect of N_1 on $u_2(\eta)$. The parameter N_1 is the ratio of the vortex viscosity to the dynamic viscosity of the fluid. In fact, it is a measure of which viscosity dominates the flow under consideration. Larger values of N_1 correspond the situation in which vortex viscosity due to spinning motion of fluid particles dominates the flow and as a result axial velocity $u_2(\eta)$ decreases in the upper part of the channel. In order to maintain the prescribed flow rate the axial velocity $u_2(\eta)$ rises with rising N_1. **Fig. 7.4** shows an enhancement in the magnitude of microrotation component $w(\eta)$ with increasing N_1 in both the parts of the channel. **Fig. 7.5** shows the impact of micropolar parameter (N_2) on $u_2(\eta)$. It is observed $u_2(\eta)$ increases with increasing N_2 in lower part of the channel. In contrast $u_2(\eta)$ decreases with increasing N_2 in upper part of the channel. **Fig. 7.6** displays influence of N_2 on $w(\eta)$. It is examined that $w(\eta)$ decreases in lower portion of the channel while it increases in upper portion with increasing N_2. **Figs. 7.7 - 7.10** exhibit the effect of Hartmann number (*Ha*), coupling number (N_1), micropolar parameter (N_2) and curvature parameter (γ) on Δp. The shapes of Δp for various magnitudes of *Ha* (Hartmann number) and coupling number (N_1) are shown in **Figs. 7.7** and **7.8**. It is examined that in pumping region $(\Theta > 0, \Delta p > 0)$, pressure rise per wavelength increases with increasing *Ha* and N_1 **Fig. 7.9** shows the

effects of micropolar parameter (N_2) on Δp. In case of micropolar parameter an opposite trend is observed as seen in figure **7.7**. **Fig. 7.10** depicts the influence of curvature parameter (γ) on Δp. It is noticed that Δp decreases with increasing γ.

The profiles of temperature field $(\theta(\eta))$ for different values of Brinkman number (Br), coupling number (N_1), micropolar parameter (N_2) and Hartmann number (*Ha*), are shown through **Figs. 7.11 - 7.14**, respectively. It is examined that $\theta(\eta)$ increases over the entire cross-section with mounting each of *Br*, N_1 and N_2. The increase in $\theta(\eta)$ with increasing N_1 and N_2 is due to retarding effect of these parameters on velocity $u_2(\eta)$. Brinkmann number is a parameter which is the ratio of viscous heat to the heat transported by conduction. Larger values of Brinkmann correspond to the scenario when heat generated due to viscous dissipation is dominant. **Fig. 7.14** shows that $\theta(\eta)$ decreases with increasing *Ha*.

The variations of *z* at the upper wall for various values of *Ha*, N_1 and N_2 are displayed in **Figs. 7.15 - 7.17**. The behavior of *z* is clearly oscillating which is attributed to oscillatory nature of the channel walls. A damping in amplitude of oscillations is observed with increasing *Ha*.

The effects of *Br* (Brinkman number), R_c (rate of chemical reaction), *Ha* (Hartmann number), *Sc* (Schmidt number) and *Sr* (Soret number) on mass concentration ($\phi(\eta)$) can be observed through **Figs. 7.18 - 7.22.** It is observed that $\phi(\eta)$ is enhanced with increasing *Br*, R_c, *Sc* and *Sr*. On the contrary, $\phi(\eta)$ decreases with increasing *Ha*.

The streamlines of flow inside the channel for various values of curvature parameter (γ), and coupling number (N_1) are shown in **Figs. 7.23 - 7.24**. The objective is to investigate the trapping phenomenon. **Fig. 7.23** shows the effect of γ on flow patterns. A trapped fluid appeared in the upper part of the channel occurs for smaller magnitudes of γ. However, such a bolus slits two symmetric parts with increasing γ. The effects of coupling number N_1 on flow patterns are displayed in **Fig. 7.24.** It is observed that with increasing N_1 to 1.2, the bolus divides into two parts. The upper part is bigger in size than the lower one. The lower part of the bolus increases in size with increasing N_1 to 1.4. It is strongly anticipated that upper part of bolus vanishes with further increasing N_1 and channel is only filled with a single bolus concentrated in the lower part.

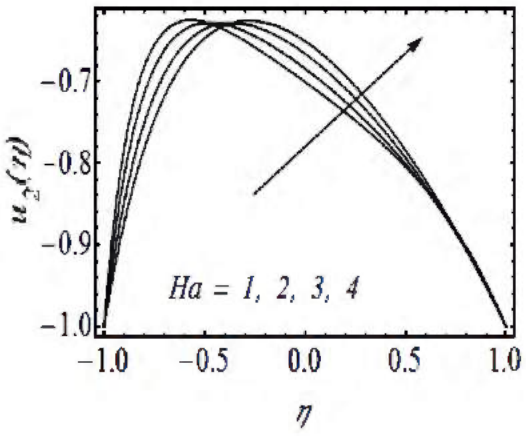

Fig. 7.1: Effect of *Ha* on $u_2(\eta)$ for γ = 2.5, N_1 = 0.5, N_2 = 1.2 and Θ = 1.5.

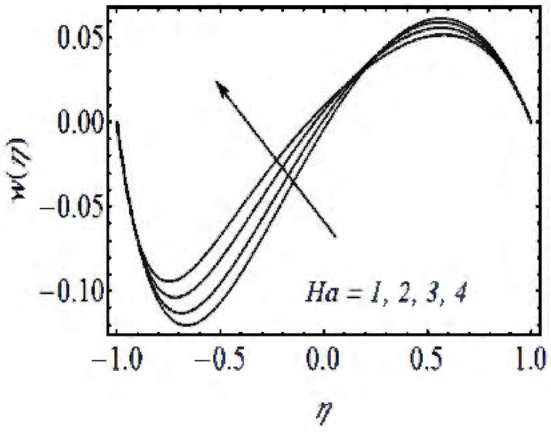

Fig. 7.2: Effect of *Ha* on $w(\eta)$ for γ = 2.5, N_1 = 0.5, N_2 = 1.2 and Θ = 1.5.

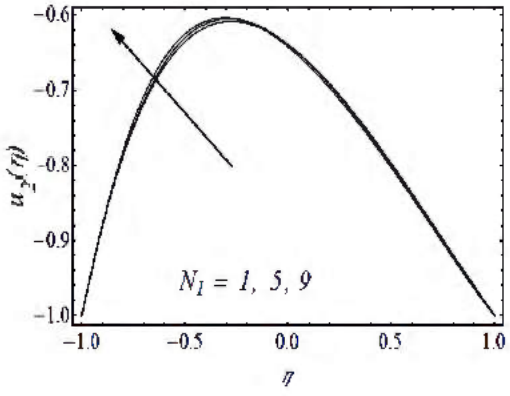

Fig. 7.3: Effect of N_1 on $u_2(\eta)$ for γ = 2.5, *Ha* = 2, N_2 = 0.2, λ = 0.4 and Θ = 1.5.

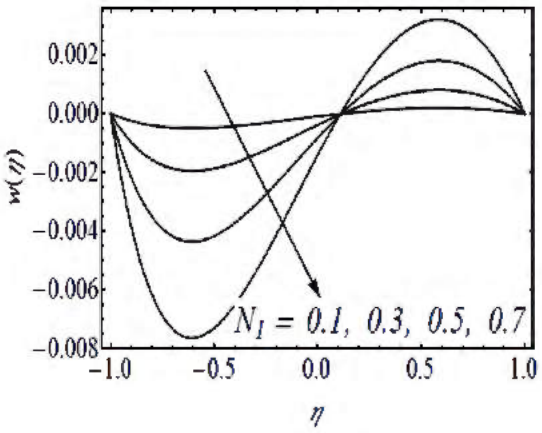

Fig. 7.4: Effect of N_1 on $w(\eta)$ for γ = 2.5, N_2 = 0.2, λ = 0.4 and Θ = 1.5.

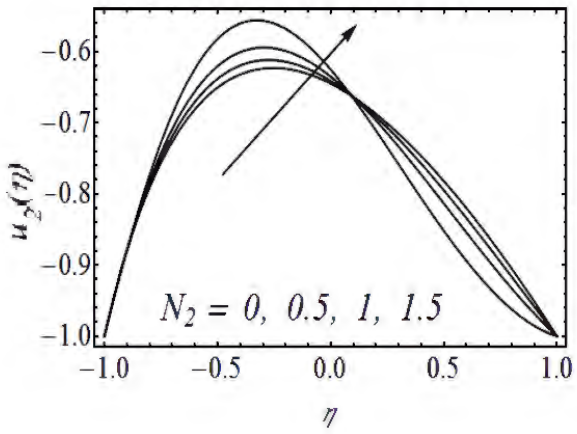

Fig. 7.5: Effect of N_2 on $u_2(\eta)$ for γ = 2.5, Ha = 2, N_1 = 0.5, $\lambda = 0.4$ and Θ = 1.5.

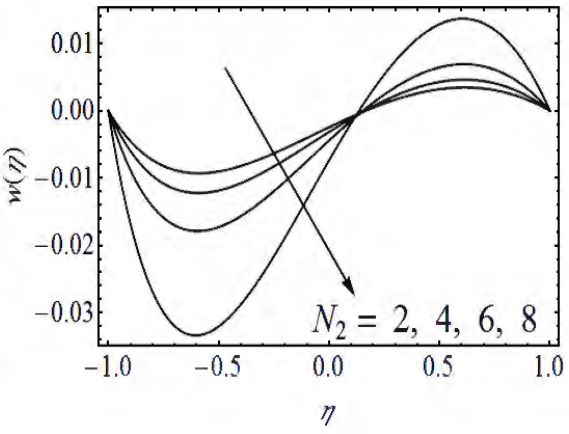

Fig. 7.6: Effect of N_2 on $w(\eta)$ for γ = 2.5, N_1 = 0.5, $\lambda = 0.4$ and Θ = 1.5.

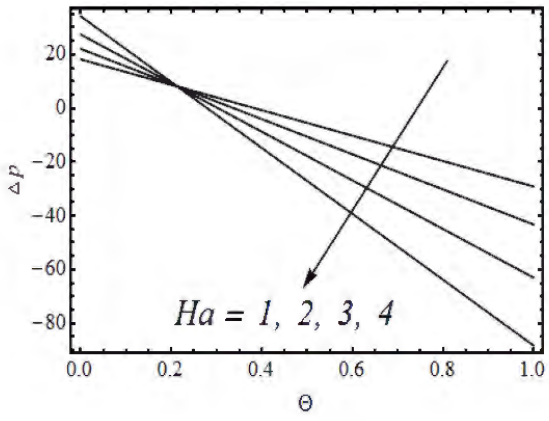

Fig. 7.7: Effect of Ha on Δp for N_1 = 0.5, N_2 = 1.2, γ = 2.5 and $\lambda = 0.4$.

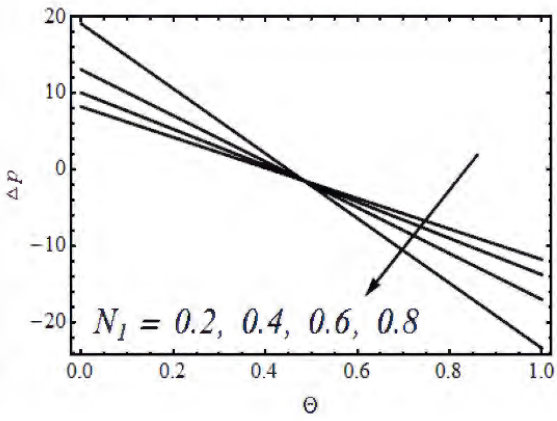

Fig. 7.8: Effect of N_1 on Δp for γ = 2.5, N_2 = 1.2 and $\lambda = 0.4$.

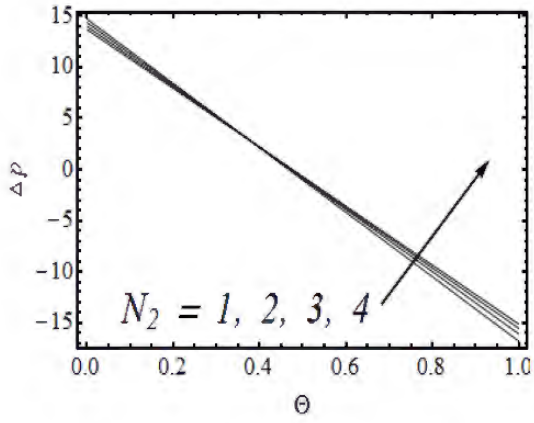

Fig. 7.9: Effect of N_2 on pressure rise per wavelength for $N_1 = 0.5$, $\gamma = 2.5$ and $\lambda = 0.4$.

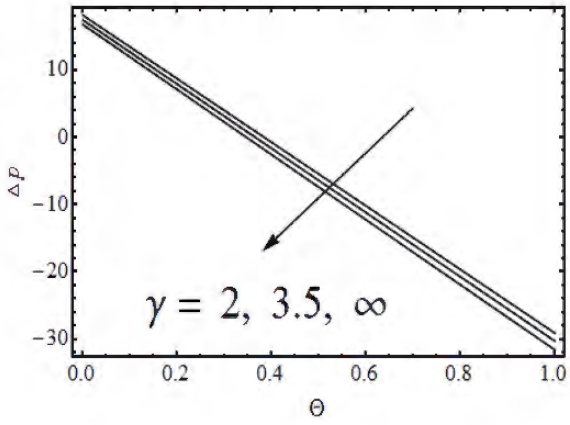

Fig. 7.10: Effect of γ on pressure rise per wavelength for $N_1 = 0.5$, $N_2 = 1.2$ and $\lambda = 0.4$.

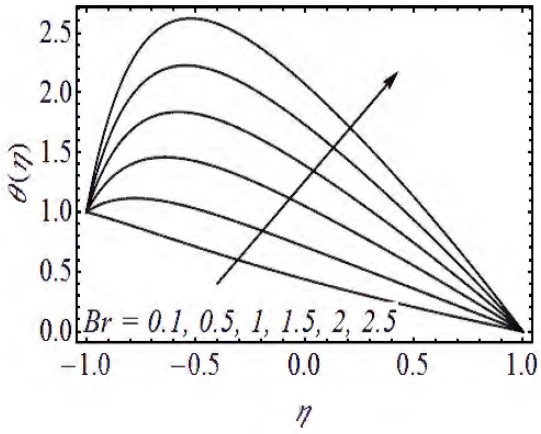

Fig. 7.11: Effect of *Br* on temperature $\theta(\eta)$ for $N_1 = 0.5$, $N_2 = 1.2$, $\lambda = 0.4$ and $\gamma = 2$.

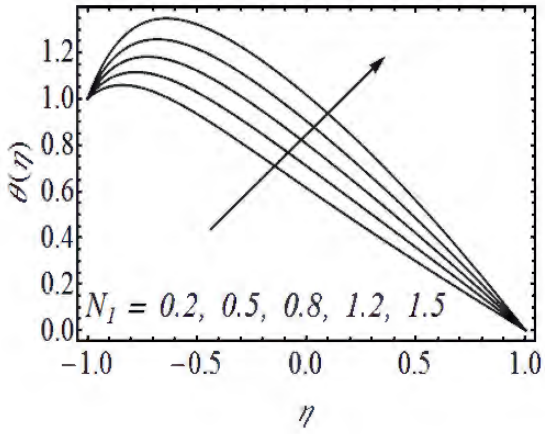

Fig. 7.12: Effect of N_1 on temperature $\theta(\eta)$ for $N_2 = 1.2$, $\lambda = 0.4$ and $\gamma = 2$.

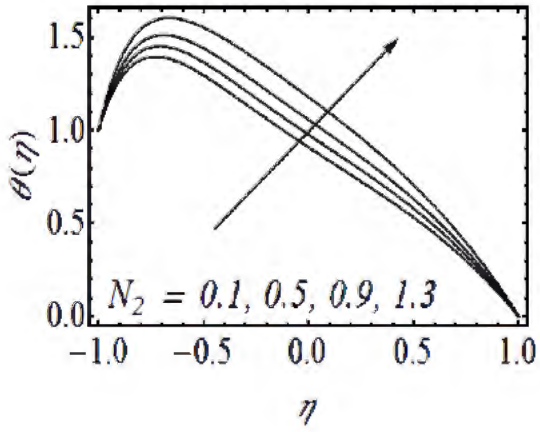

Fig. 7.13: Influence of N_2 on $\theta(\eta)$ for Br = 2, N_1 = 0.5, $\lambda = 0.4$ and γ = 2.

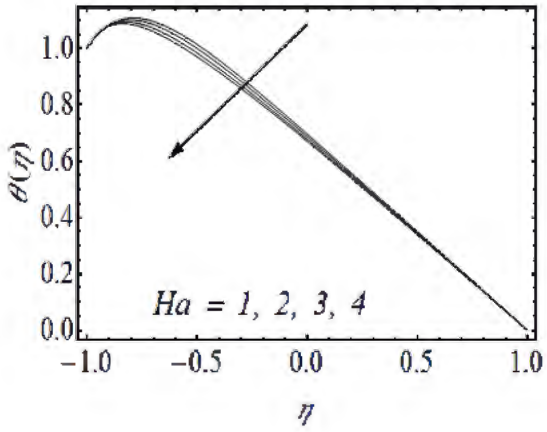

Fig. 7.14: Influence of Ha on $\theta(\eta)$ for N_1 = 0.5, N_2 = 1.2, $\lambda = 0.4$ and γ =2.

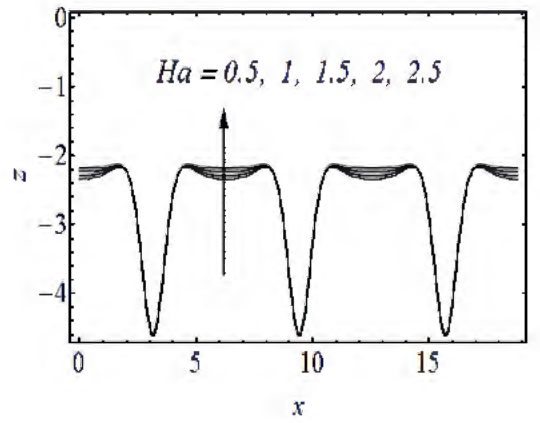

Fig. 7.15: Effect of Ha on z at upper wall for N_1 = 0.5, N_2 = 1.2 and γ = 2.

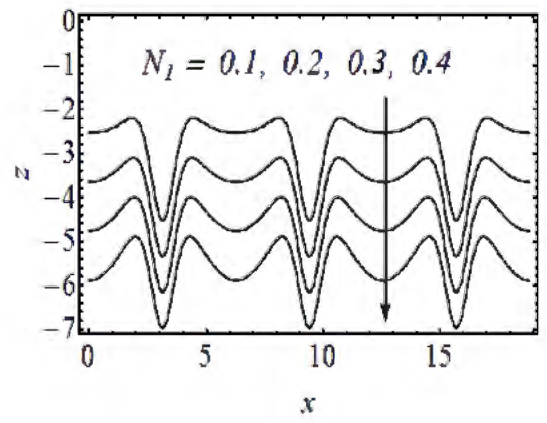

Fig. 7.16: Effect of N_1 on z at upper wall for Br = 2, N_2 = 1.2 and γ = 2.

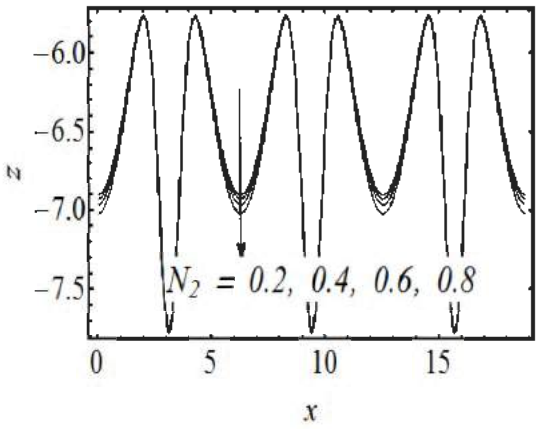

Fig. 7.17: Influence of N_2 on *z* at upper wall for $N_1 = 0.5$, $\lambda = 0.4$ and $\gamma = 2$.

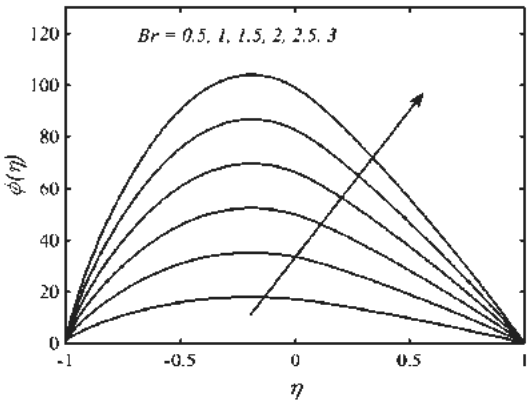

Fig. 7.18: Influence of *Br* on concentration $\phi(\eta)$ for $N_1 = 0.5$, $N_2 = 1.2$, $\lambda = 0.4$, and $\gamma = 2$.

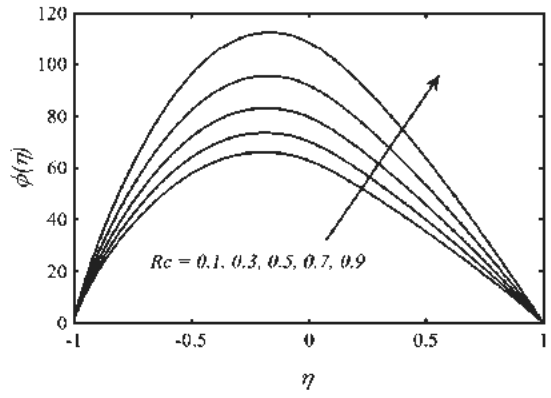

Fig. 7.19: Effect of R_c on concentration $\phi(\eta)$ for *Br* = 2, $N_1 = 0.5$, $N_2 = 1.2$, $\lambda = 0.4$, and $\gamma = 2$.

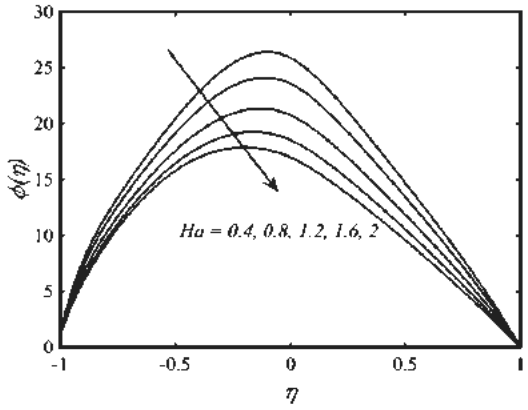

Fig. 7.20: Effect of *Ha* on concentration $\phi(\eta)$ for *Br* = 2, $N_1 = 0.5$, $N_2 = 1.2$, $\lambda = 0.4$, and $\gamma = 2$.

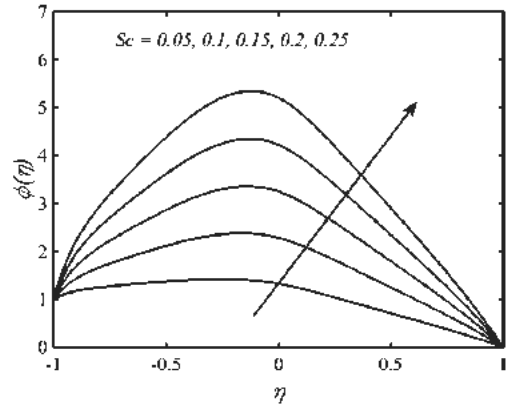

Fig. 7.21: Effect of Schmidt number *Sc* on concentration $\phi(\eta)$ for *Br* = 2, N_1 = 0.5, = 1.2, $\lambda = 0.4$ and γ = 2.

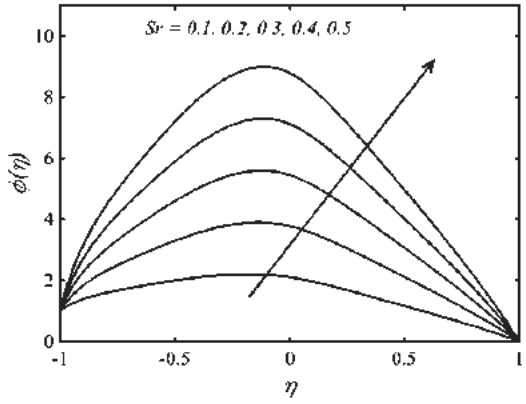

Fig. 7.22: Effect of Soret number *Sr* on concentration $\phi(\eta)$ for *Br* = 2, N_1 = 0.5, N_2 = 1.2, $\lambda = 0.4$ and γ = 2.

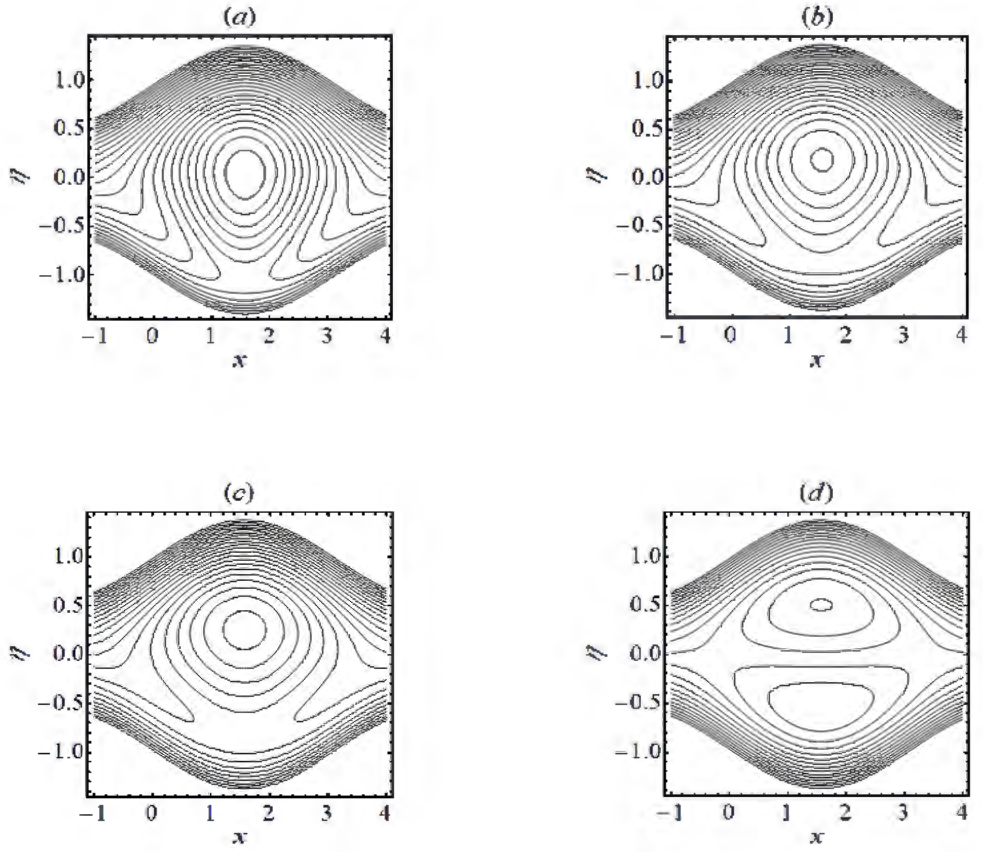

Fig. 7.23: Flow patterns for (a) $\gamma = 2$, (b) $\gamma = 2.5$, (c) $\gamma = 3$ and (d) $\gamma \to \infty$, using $N_1 = 0.5$, $N_2 = 1.2$ and $\lambda = 0.8$.

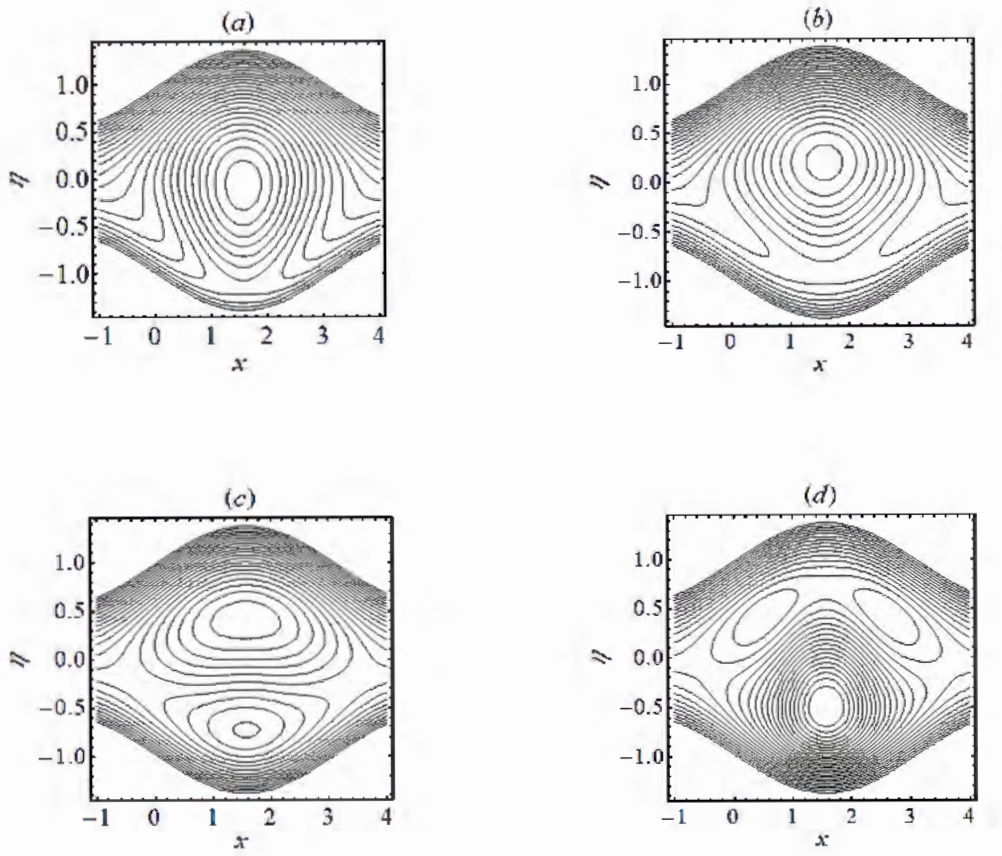

Fig. 7.24: Flow patterns for (a) $N_1 = 0.8$, (b) $N_1 = 1$, (c) $N_1 = 1.2$, and (d) $N_1 = 1.4$, using $Ha = 2$, $N_2 = 1.2$, $\gamma = 2.5$ and $\lambda = 0.8$.

Chapter 8

Numerical modeling of heat and mass transfer in flow of bi-viscosity fluid through a porous-saturated curved channel with contracting and expanding walls

In this chapter we discussed the heat/ mass transfer in flow of bi-viscosity fluid through a porous-saturated curved channel with sinusoidally deformed walls. The magnetic field and Joule heating effects are also taken into account. A reduction of these equations is made based on long wavelength and low Reynolds approximations. The reduced linear ordinary differential equations are integrated numerically using an implicit finite difference scheme. It is observed that the bi-viscosity fluid parameter, permeability parameter and Hartmann number have analogous effects on the longitudinal velocity. Moreover, temperature of the fluid, heat coefficient and mass concentration increase by increasing bi-viscosity fluid parameter, Brinkmann number and Hartmann number.

8.1 Modeling

An incompressible bi-viscosity fluid flows inside the porous-saturated curved channel. The continuity and energy equations are given by Eqs. (2.3) and (2.5), respectively. The momentum and mass concentration are given by

$$\rho \frac{d\mathbf{U}}{dt} = \nabla \cdot \boldsymbol{\tau} - \frac{\mu}{k^*}\mathbf{U} + \mathbf{J} \times \mathbf{B}, \qquad \textit{(Momentum Equation)} \qquad (8.1)$$

$$\frac{dC}{dt} = D\nabla^2 C + \frac{DK_T}{T_m}\nabla^2 T - k_1 C. \qquad (\textit{Mass Concentration Equation}) \qquad (8.2)$$

Eq. (8.2) differ from its counterparts due to the addition of chemical reaction term. For bi-viscosity fluid model

$$\boldsymbol{\tau} = \begin{cases} \left(\mu_b + \dfrac{P_y}{\sqrt{2\Pi}}\right)\mathbf{A_1}, & \text{when } \Pi > \Pi_C \\ \left(\mu_b + \dfrac{P_y}{\sqrt{2\Pi}}\right)\mathbf{A_1}, & \text{when } \Pi < \Pi_C \end{cases}, \qquad (8.3)$$

where P_y is the yield stress of the fluid given by

$$P_y = \frac{\mu_b\sqrt{2\Pi}}{\beta}. \qquad (8.4)$$

Here β is the bi-viscosity fluid parameter, μ_b is the plastic dynamic viscosity, Π is second invariant of $\mathbf{A_1}$, Π_C is the critical value based on non-Newtonian model. For bi-viscosity fluid flow, where $\Pi > \Pi_C$, it is possible to write

$$\mu = \mu_b + \frac{P_y}{\sqrt{2\Pi}}. \qquad (8.5)$$

Using (8.4) and (8.5), we get stress tensor for bi-viscosity fluid flow

$$\boldsymbol{\tau} = \mu_b\left(1 + \frac{1}{\beta}\right)\mathbf{A_1}. \quad \text{when } \Pi > \Pi_C. \qquad (8.6)$$

In view of (8.6), Eq. (8.1) becomes

$$\rho\frac{d\mathbf{U}}{dt} = \mu_b\left(1 + \frac{1}{\beta}\right)\nabla\cdot\mathbf{A_1} - \frac{\mu}{k^*}\mathbf{U} + \mathbf{J}\times\mathbf{B}. \qquad (8.7)$$

By using Eq. (2.11), we get above equations in component form

$$\frac{\partial U_1}{\partial t}+(U_1.\nabla)U_1-\frac{{U_2}^2}{R+\tilde{R}}=-\frac{1}{\rho}\frac{\partial P}{\partial R}+\frac{\mu_b}{\rho}\left(1+\frac{1}{\beta}\right)\left[\nabla^2U_1-\frac{U_1}{\left(R+\tilde{R}\right)^2}-\frac{2\tilde{R}}{\left(R+\tilde{R}\right)^2}\frac{\partial U_2}{\partial\chi}\right] \tag{8.8}$$

$$-\frac{\nu}{k^*}U_1,$$

$$\frac{\partial U_2}{\partial t}+(U_1.\nabla)U_2+\frac{U_1U_2}{R+\tilde{R}}=-\frac{\tilde{R}}{\rho\left(R+\tilde{R}\right)}\frac{\partial P}{\partial\chi}+\frac{\mu_b}{\rho}\left(1+\frac{1}{\beta}\right)\left[\nabla^2U_2-\frac{U_2}{\left(R+\tilde{R}\right)^2}+\frac{2\tilde{R}}{\left(R+\tilde{R}\right)^2}\frac{\partial U_1}{\partial\chi}\right] \tag{8.9}$$

$$-\frac{\nu}{k^*}U_2-\frac{\sigma B^{*2}\tilde{R}^2}{\rho\left(R+\tilde{R}\right)^2}U_2,$$

$$\frac{\partial C}{\partial t}+(U_1.\nabla)C=D\nabla^2C+\frac{DK_T}{T_m}\left(\frac{\partial^2T}{\partial R^2}+\frac{\tilde{R}}{R+\tilde{R}}\frac{\partial T}{\partial R}+\left(\frac{\tilde{R}}{R+\tilde{R}}\right)^2\frac{\partial^2T}{\partial\chi^2}\right)-k_1C, \tag{8.10}$$

where

$$\Phi=\left[2\left(\frac{\partial U_1}{\partial R}\right)^2+\left(\frac{\tilde{R}}{R+\tilde{R}}\frac{\partial U_1}{\partial\chi}-\frac{U_2}{R+\tilde{R}}\right)\left(\frac{\partial U_2}{\partial R}+\frac{\tilde{R}}{R+\tilde{R}}\frac{\partial U_1}{\partial\chi}-\frac{U_2}{R+\tilde{R}}\right)+\frac{\partial U_2}{\partial R}\left[\frac{\partial U_2}{\partial R}+\frac{\tilde{R}}{R+\tilde{R}}\frac{\partial U_1}{\partial\chi}\right.\right. \tag{8.11}$$

$$\left.\left.-\frac{U_2}{R+\tilde{R}}\right]+2\left(\frac{\tilde{R}}{R+\tilde{R}}\frac{\partial U_2}{\partial\chi}+\frac{U_1}{R+\tilde{R}}\right)\right].$$

After making use of transformations given in (2.19), the governing equations in the wave frame obtained. These equations after defining the dimensionless variables and invoking long wavelength and low Reynolds number approximations ($\delta\approx 0, \mathrm{Re}\approx 0$) reduce to

$$\frac{\partial p}{\partial\eta}=0, \tag{8.12}$$

$$-\frac{\partial p}{\partial x}+\frac{1}{\gamma}\left\{-\frac{\partial}{\partial\eta}\left((\eta+\gamma)\frac{\partial^2\psi}{\partial\eta^2}\right)-\frac{1}{\eta+\gamma}\left(1-\frac{\partial\psi}{\partial\eta}\right)\right\}-\frac{\eta+\gamma}{K^*\gamma}\left(1-\frac{\partial\psi}{\partial\eta}\right)-\frac{\gamma Ha^2}{\eta+\gamma}\left(1-\frac{\partial\psi}{\partial\eta}\right)=0, \tag{8.13}$$

$$\frac{\partial^2 \phi}{\partial \eta^2}+\frac{1}{(\gamma+\eta)}\frac{\partial \phi}{\partial \eta}-R_c\phi=-SrSc\left(\frac{\partial^2 \theta}{\partial \eta^2}+\frac{1}{(\gamma+\eta)}\frac{\partial \theta}{\partial \eta}\right)+R_c. \tag{8.14}$$

Elimination of pressure between Eqs. (8.12) and (8.13) yield

$$\frac{\partial}{\partial \eta}\left[\frac{1}{\gamma}\left(\frac{\partial}{\partial \eta}\left\{(\eta+\gamma)\frac{\partial^2 \psi}{\partial \eta^2}\right\}+\frac{1}{\eta+\gamma}\left(1-\frac{\partial \psi}{\partial \eta}\right)\right)+\frac{\eta+\gamma}{K^*\gamma}\left(1-\frac{\partial \psi}{\partial \eta}\right)+\frac{\gamma Ha^2}{\eta+\gamma}\left(1-\frac{\partial \psi}{\partial \eta}\right)\right]=0. \tag{8.15}$$

Therefore, for the analysis of present problem we have to solve Eqs. (2.23), (8.14) and (8.15) subject to boundary conditions (2.27) and (2.28). Though it is possible to find an exact solution of Eq. (8.15) but the whole set of equations can be solved numerically. An implicit finite difference technique is employed for the solution Eqs. (2.23), (8.14) and (8.15) subject to boundary conditions (2.27) and (2.28).

8.2 Results and discussion

In this section, it is intended to analyze the important features of peristaltic motion such as velocity, pressure rise, temperature distribution, mass concentration and trapping for various values of the curvature parameter (γ), bi-viscosity parameter (β), Brinkman number (*Br*), rate of chemical action (R_c), permeability parameter (K^*) and Hartmann number (*Ha*).

The axial velocity distribution for some specific values of bi-viscosity parameter (β), permeability parameter (K^*), Hartmann number (*Ha*) and curvature parameter (γ), is shown in **Figs. 8.1 - 8.4**, respectively. **Fig. 8.1** depicts that velocity profile increases by increasing

bi-viscosity parameter. **Fig. 8.1** depicts that velocity profile increases by increasing Casson parameter. **Fig. 8.2** shows the effects of permeability parameter (K^*) on velocity $(u_2(\eta))$. Smaller values of K^* correspond to weaker porous medium effects while larger values represent the case when resistance due to porous matrix is strong. It is seen that greater values of K^* impede the velocity amplitude and shift the maximum velocity away from the lower wall of the channel towards the central line $(\eta = 0)$. **Fig. 8.3** exhibits the influence of *Ha* on $u_2(\eta)$. Here it is quite obvious that flow velocity displays boundary layer character for increasing values of *Ha*. The fluid outside the boundary layer moves with a velocity which varies linearly with radial coordinate η. In contrast, the fluid outside the boundary layers moves with constant velocity in a straight channel. **Fig. 8.4** depicts the influence of γ on $u_2(\eta)$. For smaller values of γ the velocity is asymmetric about $\eta = 0$ with maximum seeming in the upper half of the channel. With increasing γ, $u_2(\eta)$ regains its symmetry about $\eta = 0$.

Figs 8.5 - 8.8 demonstrate the effect of different parameters on pressure rise per wavelength. **Fig 8.5** shows the influence of bi-viscosity parameter on Δp. It is noticed that Δp is decreasing by increasing β in the peristaltic pumping region. The profile of pressure rise per wavelength for various values of K^* (permeability parameter) is shown in **Fig. 8.6**. Here, it is noticed that Δp decreases with enhancing K^* for fixed value of prescribed flow rate. Thus, in the present settings the porous medium inside the channel hampers the normal flow of the fluid and peristalsis has to do greater work against the pressure rise to maintain the same flux as in the case of clear medium inside the channel. This eventually reduces

the pumping efficiency. **Figs. 8.7 and 8.8** are designed to show the variation of Δp against dimensionless mean flow rate Θ for numerous values of *Ha* and γ, respectively. It is noticed that Δp rises by rising *Ha* and γ.

Figs. 8.9 - 8.12 are plotted to analyze the effect of bi-viscosity parameter (β), Brinkmann number (*Br*), permeability parameter (K^*) and Hartmann number (*Ha*) on radial distribution of temperature of the fluid inside the channel. Figs. **8.9**, **8.10** and **8.12** respectively, report that $\theta(\eta)$ increases by increasing β, *Br* and *Ha* inside the channel. In contrast, **Fig 8.11** shows a decrease in temperature with increasing permeability parameter. It is due to the fact that heat transfer rate from boundaries to the fluid is reduced for clear medium and as a result a decrease in temperature is noted inside the channel.

The shift of z for β, *Br*, K^* and *Ha* is shown through **Figs. 8.13 - 8.16**. The profiles of *z* are clearly oscillating (periodic) due to periodic oscillating nature of the boundary. The amplitude of oscillation enhances with enhancing β, *Br* and *Ha*, while it shows opposite behavior with increasing K^*.

The profiles of mass concentration inside the channel for several values of bi-viscosity parameter, Brinkmann number, rate of chemical reaction, Hartmann number, Schmidt number and Soret number are shown in **Figs. 8.17 - 8.22**. It is noticed that mass concentration inside the channel enhances with enhancing each of these parameters.

The streamlines of flow for specific values of bi-viscosity parameter (β), permeability parameter (K^*), Hartmann number (*Ha*) and curvature parameter (γ) are shown in **Figs. 8.23 - 8.25**. **Fig. 8.23** shows two nearly symmetric circulating rolls in lower and upper halves of the channel. However, lower roll increases in size while the upper one shrinks

with increasing β. **Fig. 8.24** illustrates the impact of K^* on trapping phenomenon. For slight values of K^* i.e. for strong permeability effects the circulating roll in lower half contains two small eddies. The size of lower half is greater than the upper one. With increasing K^*, the two eddies inside the lower roll merge into a single cell. Moreover, the size of upper roll reduces with increasing K^*. The formation of two circulating eddies in the lower roll for small values of K^* is never reported in the earlier available literature on the peristaltic flows through porous-saturated curved channel. **Fig. 8.25** shows the effect of γ (dimensionless radius of curvature) on trapping. It is observed that both circulating roll become equal in size with increasing γ.

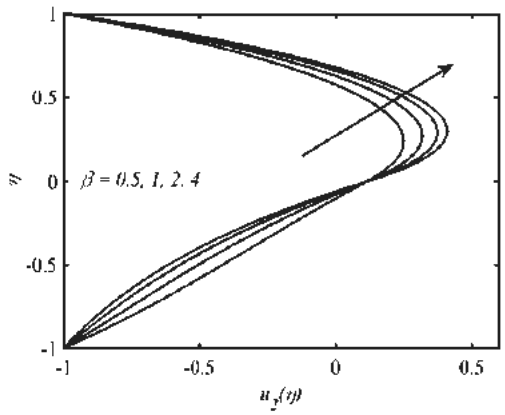

Fig. 8.1: Effect of β on velocity $u_2(\eta)$ for γ = 2.5, K^* = 0.2, *Ha* = 0.5, $\lambda = 0.4$, and Θ = 1.5.

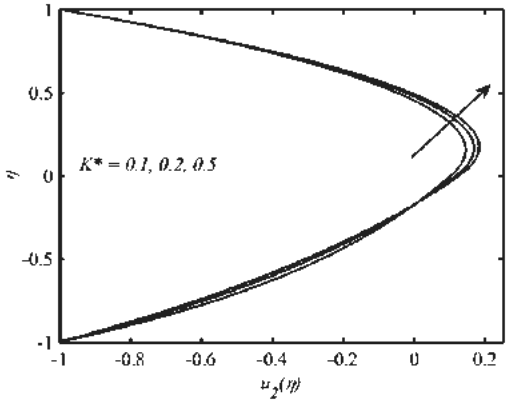

Fig. 8.2: Effect of K^* on velocity $u_2(\eta)$ for γ = 2.5, β = 0.2, $\lambda = 0.4$, and Θ = 1.5.

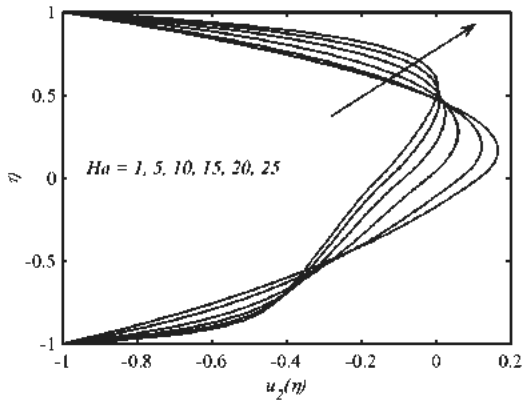

Fig. 8.3: Effect of *Ha* on velocity $u_2(\eta)$ for γ = 2.5, K^* = 0.2, β = 0.2, $\lambda = 0.4$, and Θ = 1.5.

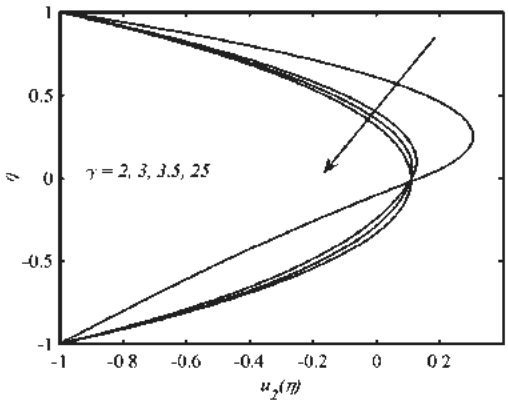

Fig. 8.4: Effect of γ on velocity $u_2(\eta)$ for β = 0.2, K^* = 0.2, *Ha* = 0.5, $\lambda = 0.4$, and Θ = 1.5.

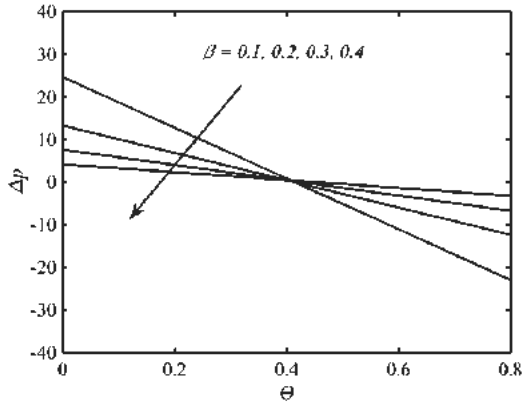

Fig. 8.5: Effect of β on Δp for γ = 2.5, K^* = 0.2, Ha = 0.5, $\lambda = 0.4$, and Θ = 1.5.

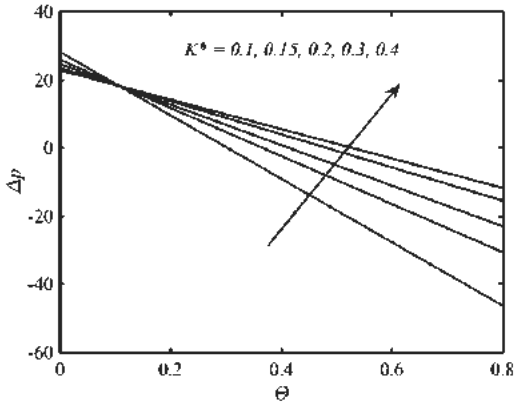

Fig. 8.6: Effect of K^* on Δp for γ = 2.5, Ha = 0.5, $\lambda = 0.4$, and Θ = 1.5.

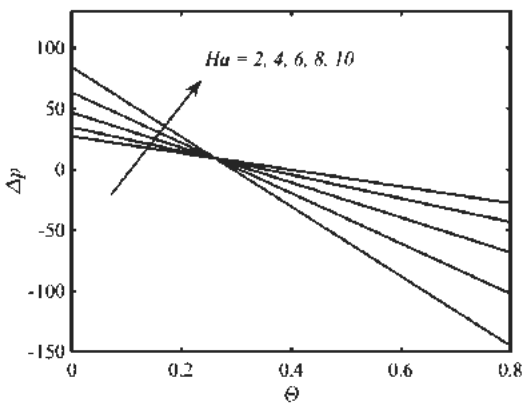

Fig. 8.7: Effect of Ha on Δp for γ = 2.5, K^* = 0.2, β = 0.2, $\lambda = 0.4$, and Θ = 1.5.

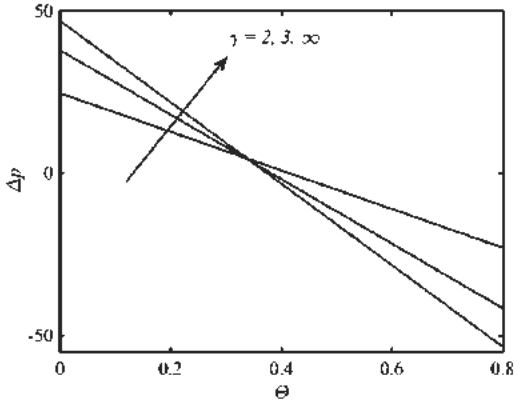

Fig. 8.8: Effect of γ on Δp for K^* = 0.2, β = 0.2, $\lambda = 0.4$, and Θ = 1.5.

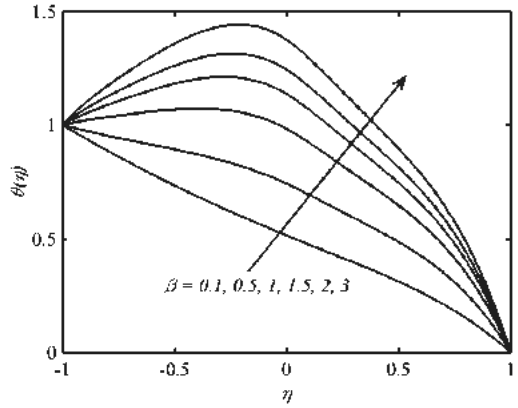

Fig. 8.9: Effect of β on temperature $\theta(\eta)$ for Br = 0.2, γ = 2, K^* = 1, Ha = 0.5, $\lambda = 0.4$, and Θ = 1.5.

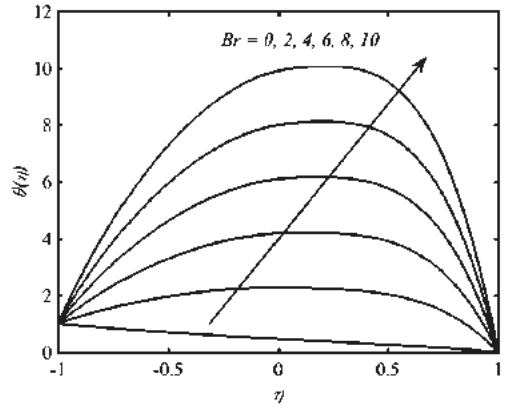

Fig. 8.10: Effect of Br on temperature $\theta(\eta)$ for β =0.2, γ = 2, Ha = 0.5, $\lambda = 0.4$ and Θ = 1.5.

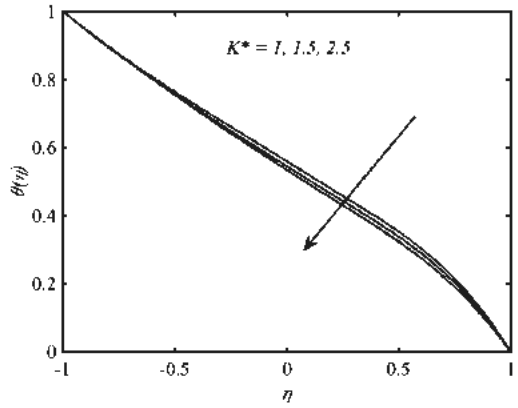

Fig. 8.11: Effect of K^* on temperature $\theta(\eta)$ for Br = 0.2, γ = 2, Ha = 0.5, β = 0.2, $\lambda = 0.4$, and Θ = 1.5.

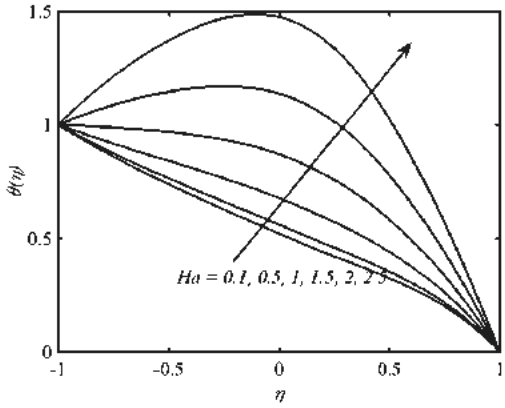

Fig. 8.12: Effect of Ha on temperature $\theta(\eta)$ for Br = 0.2, γ = 2, K^* = 1.5, β = 0.2, $\lambda = 0.4$, and Θ = 1.5.

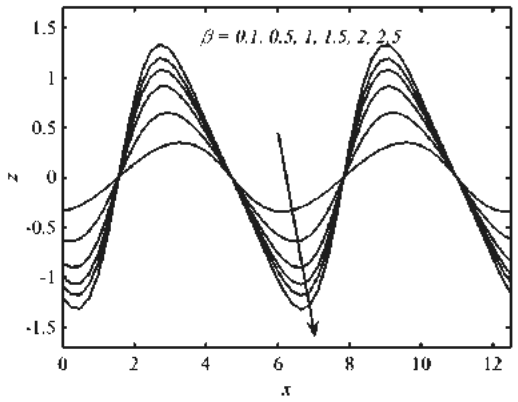

Fig. 8.13: Influence of β on z for Br = 0.2, γ = 2, K^* = 1, $\lambda = 0.4$ and Θ = 1.5.

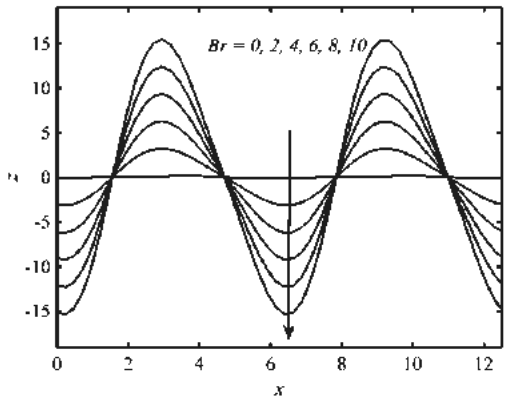

Fig. 8.14: Influence of Br on z for β = 0.2, γ = 2, $\lambda = 0.4$ and Θ = 1.5.

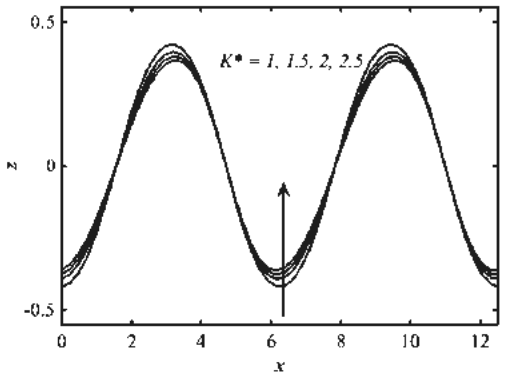

Fig. 8.15: Effect of K^* on z for Br = 0.2, γ = 2, Ha = 0.5, $\lambda = 0.4$ and Θ = 1.5.

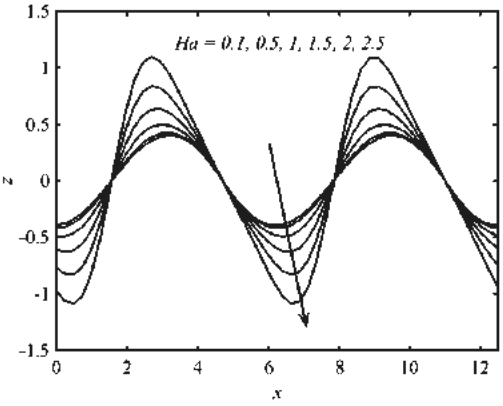

Fig. 8.16: Effect of Ha on z for Br = 0.2, γ = 2, K^* = 1.5, $\lambda = 0.4$ and Θ = 1.5.

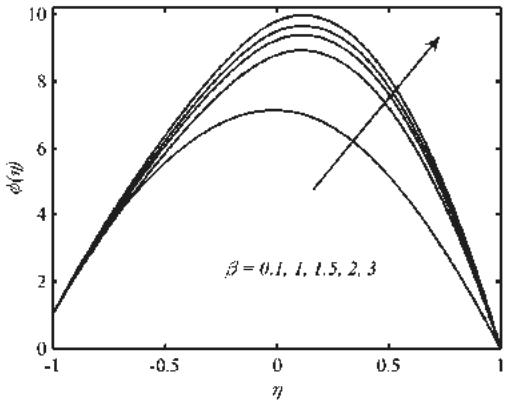

Fig. 8.17: Effect of β on $\phi(\eta)$ for *Br* = 2, γ = 2, R_c = 0.2, *Sr* = 1.5, *Sc* = 1.2, $\lambda = 0.4$ and Θ = 1.5.

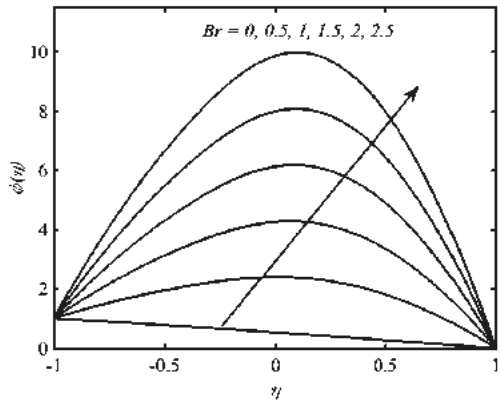

Fig. 8.18: Effect of *Br* on $\phi(\eta)$ for β = 0.4, γ = 2, *Sr* = 1.5, *Sc* = 1.2, $\lambda = 0.4$ and Θ = 1.5.

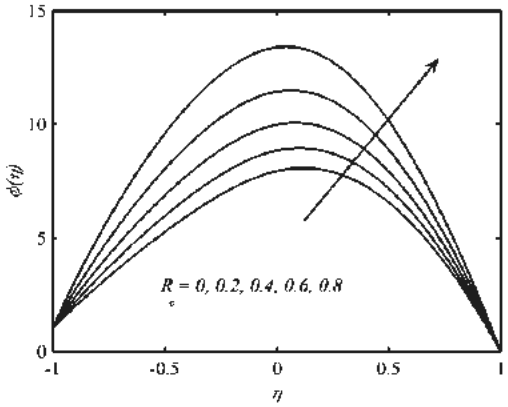

Fig. 8.19: Effect of β on $\phi(\eta)$ for β = 0.4, *Br* = 2, γ = 2, *Sr* = 1.5, *Sc* = 1.2, $\lambda = 0.4$ and Θ = 1.5.

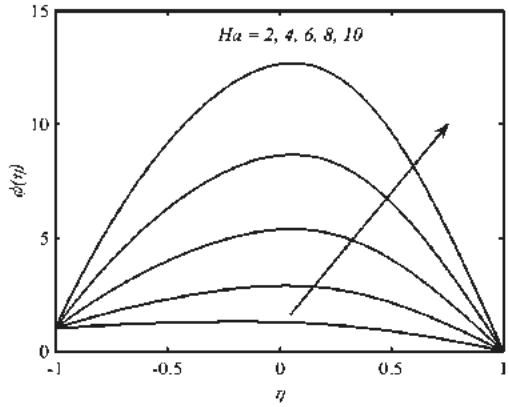

Fig. 8.20: Effect of *Ha* on $\phi(\eta)$ for β = 0.4, R_c = 0.2, *Sr* = 1.5, *Sc* = 1.2 $\lambda = 0.4$ and Θ = 1.5.

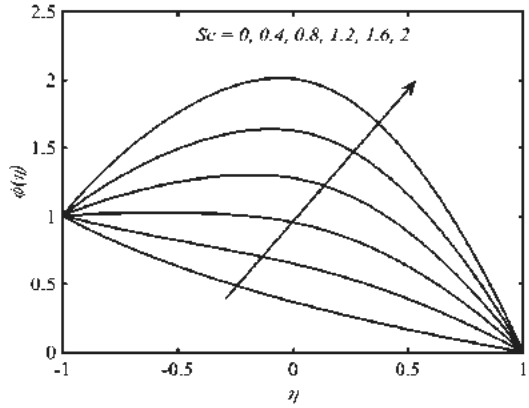

Fig. 8.21: Influence of *Sc* on $\phi(\eta)$ for β = 0.4, *Br* = 2, γ = 2, R_c = 0.2, *Sr* = 1.5, $\lambda = 0.4$ and Θ = 1.5.

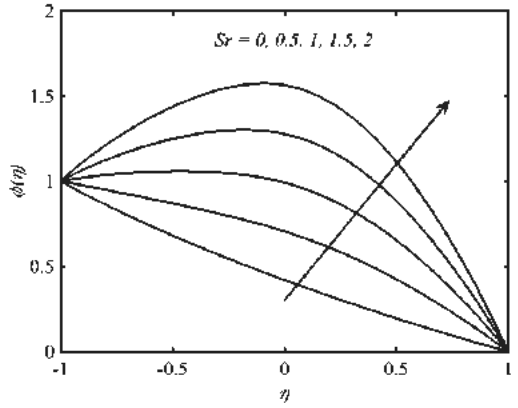

Fig. 8.22: Influence of *Sr* on $\phi(\eta)$ for β = 0.4, *Br* = 2, γ = 2, R_c = 0.2, *Sc* = 1.2, $\lambda = 0.4$ and Θ = 1.5.

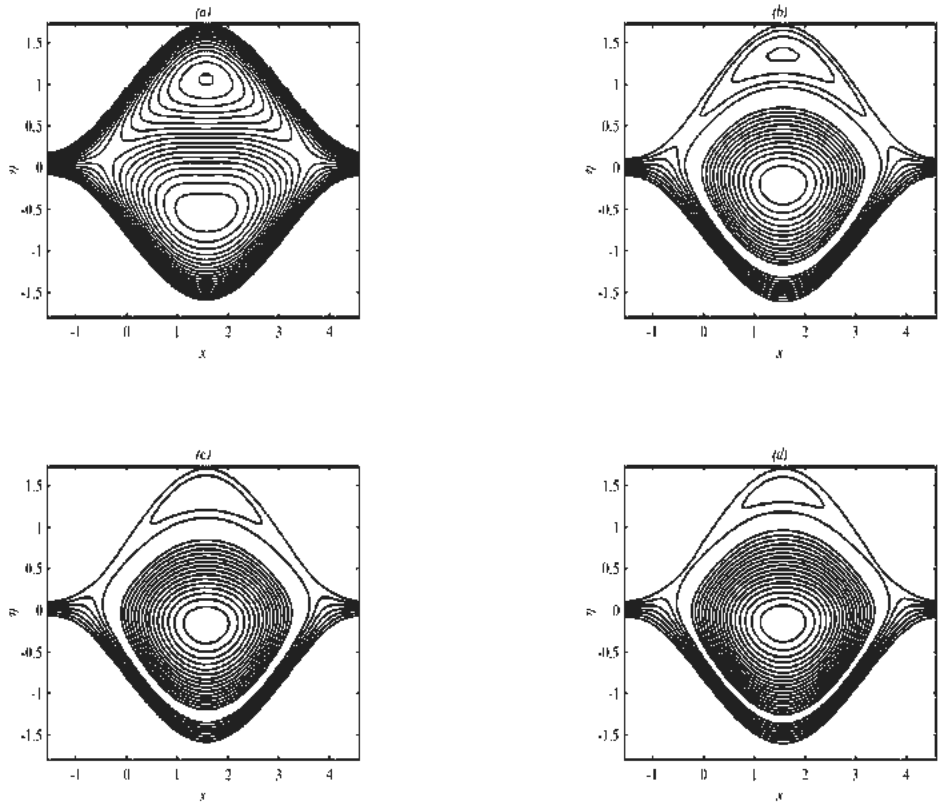

Fig. 8.23: Flow patterns for (a) $\beta = 0.1$, (b) $\beta = 0.5$, (c) $\beta = 1$ and (d) $\beta = 1.5$, using $\gamma = 2$, $K^* = 1$, $Ha = 0.5$, $\lambda = 0.4$ and $\Theta = 1$.

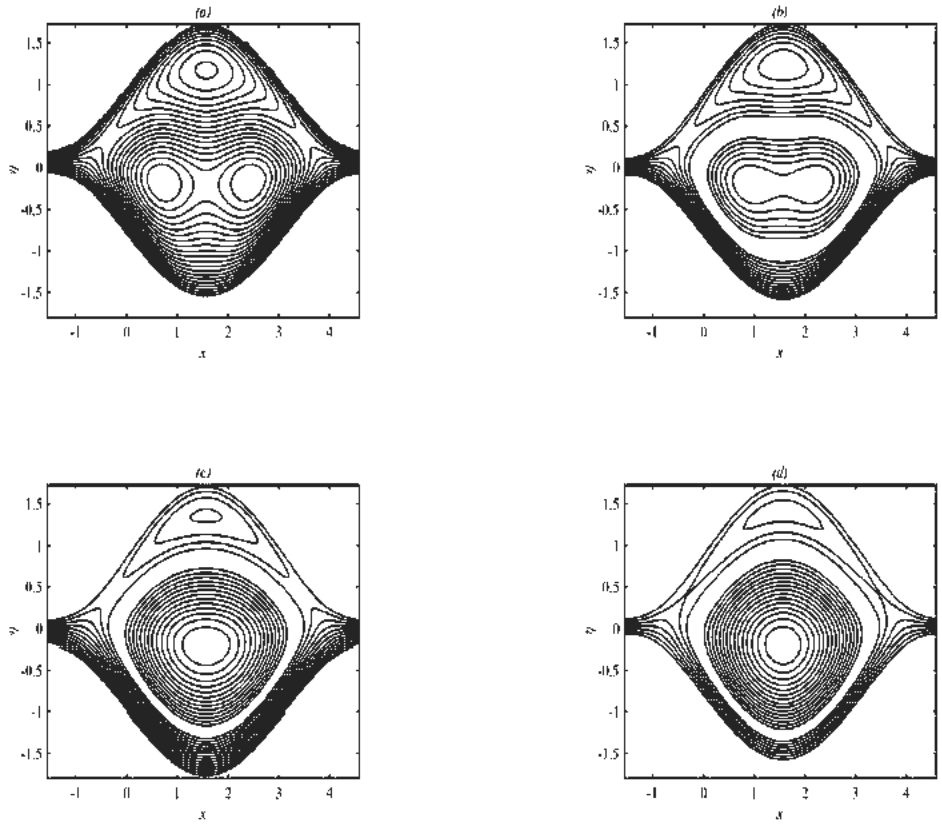

Fig. 8.24: Flow patterns for (a) $K^* = 0.1,$ (b) $K^* = 0.15,$ (c) $K^* = 0.2,$ and (d) $K^* = 0.3,$ using γ = 2, *Ha* = 0.5, $\beta = 0.5,$ $\lambda = 0.4$ and Θ = 1.5.

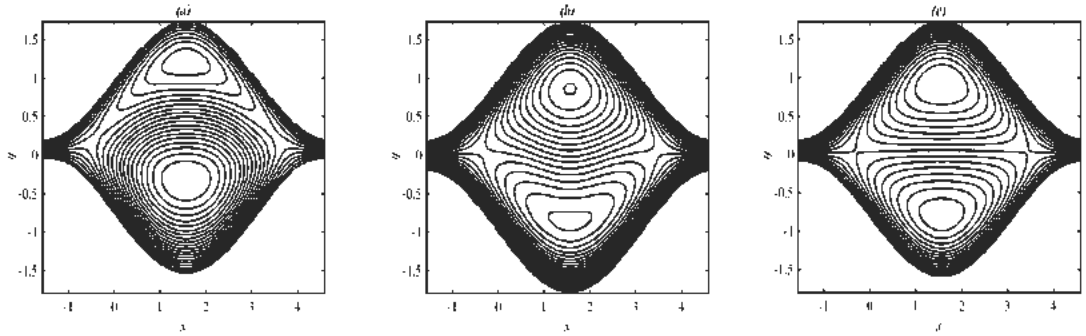

Fig. 8.25: Flow patterns for (a) $\gamma = 2,$ (b) $\gamma = 3.5$ and (c) $\gamma \to \infty,$ using *Ha* = 0.5, K^* = 0.2, $\beta = 0.5,$ $\lambda = 0.4$ and Θ = 1.5.

Chapter 9

CONCLUSIONS

The main objective of thesis was to analyze the heat and mass transfer characteristics in peristaltic flows through a curved geometry. To achieve the objective, the simulations are performed by utilizing FDM. The major predictions of the thesis are summarized below.

- The flow velocity diminishes with increasing permeability parameter and Hartmann number.
- Pressure rise per wavelength increases with increasing permeability parameter and Hartmann number.
- The radial distribution of temperature inside the channel follows an increasing trend with increasing Brinkmann number, permeability parameter and Hartmann number while it decreases with enhancing Forchiemmer parameter.
- The size of circulating bolus of fluid reduces with increasing permeability parameter and Hartmann number while it is almost unaffected with enhancing Forchiemmer parameter.
- The symmetry in velocity and streamlines pattern is observed when curvature parameter is increased indefinitely.
- The flow velocity and pressure rise increases with increasing thermal transfer Grashof number. A reverse trend is noted with increasing concentration Grashof number and Hartmann number.

- The temperature field is enhanced with increasing thermal Grashof number and Hartmann number.
- The mass concentration decreases with increasing thermal Grashof number and Hartmann number while it enhances with enhancing concentration Grashof number.
- The circulations become intense for greater values of Brinkman number, thermal Grashof number and Hartmann number. Thus, more mixing is realized in mixed convective peristaltic flow than that in a purely peristaltic flow.
- Both temperature and mass concentration profiles are strongly influenced by Sisko fluid parameter and Brinkmann number. Each of this physical quantity is found to increase with increasing viscosity parameter and Brinkmann number.
- The heat transfer coefficient and Sherwood number oscillates periodically and their amplitudes are greatly enhanced with enhancing the numerical values viscosity parameter and Brinkmann number.
- The flow velocity achieves symmetric profile with increasing coefficient of pseudoplasiticity.
- The area of trapping region reduces with increasing the coefficient of pseudoplasiticity.
- The axial velocity enhances with enhancing micropolar parameter in vicinity of the lower wall while it shows opposite behavior near the upper wall.
- The Hartmann number and coupling number have similar effects on axial velocity.

- The temperature inside the channel follows an increasing trend with increasing coupling number and micropolar parameter. However, it decreases with increasing Hartmann number.
- The mass concentration increases with increasing Brinkmann number and rate of chemical reaction.
- The flow velocity increases with increasing bi-viscosity fluid parameter.
- Pressure rise per wavelength decreases with increasing bi-viscosity fluid parameter and permeability parameter.
- The temperature of fluid follows a decreasing trend with increasing permeability parameter. However, it increases with increasing bi-viscosity fluid parameter.
- The mass concentration increases with increasing rate of chemical reaction and bi-viscosity fluid parameter.
- The results for Newtonian fluid are achieved for larger values of bi-viscosity fluid parameter.

REFERENCES

Abbas, M.A., Bai, Y.Q., Bhatti, M.M. and Rashidi, M.M., (2016a) Three dimensional peristaltic flow of hyperbolic tangent fluid in non-uniform channel having flexible walls, Alex. Eng. J. 55 pp. 653-662.

Abbas, M.A., Bai, Y.Q., Rashidi, M.M., and Bhatti, M.M., (2016b) Application of drug delivery in magnetohydrodynamics peristaltic blood flow of nanofluid in a non-uniform channel, Journal of Mechanics in Medicine and Biology, 16 pp. 1650052.

Abbas, M.A., Bai, Y.Q., Rashidi, M.M., and Bhatti, M.M., (2016c) Analysis of entropy generation in the flow of peristaltic nanofluids in channels with compliant walls, Entropy 18 (3) pp. 90.

Abd El Hakeem Abd El Naby, El Misery, A. E. M., and Abd El Kareem, M. F., (2004a) Separation in the flow through peristaltic motion of a Carreau fluid in uniform tube, Physica A, 343 pp. 1–14.

Abd El Hakeem Abd El Naby, El Misery, A. E. M., and Abd El Kareem, M. F., (2006) Effects of a magnetic field on trapping through peristaltic motion for generalized Newtonian fluid in channel, Physica A, 367 pp. 79–92.

Abd El Hakeem, Abd El Naby, El Misery, A.E.M., and El Shamy, I.I., (2004b) Effects of an endoscope and fluid with variable viscosity on peristaltic motion, Appl. Math. Comp., 158 pp. 497.

Ali, N., Javid, K., and Sajid, M., (2015a) O.A. Beg, Numerical simulation of peristaltic flow of a biorheological fluid with shear-dependent viscosity in a curved channel, Comp. Meth. BioMech. BioMed. Eng., 19(6) pp. 1-14.

Ali, N., Javid, K., Sajid, M., and Hayat, T., (2016) New concept about existence of Hartmann boundary layer in peristalsis through Curved Channel-Asymptotic solution, Meccanica, 51 pp. 1783–1795.

Ali, N., Javid, K., Sajid, M., Zaman, A., Hayat, T., (2015b) Numerical simulations of Oldroyd 8-constant fluid flow and heat transfer in a curved channel, Int. J. Heat Mass Transfer, 94 500–508.

Ali, N., Sajid, M., Abbas, Z., and Javed, T., (2010d) Non-Newtonian fluid flow induced by peristaltic waves in a curved channel, European. Journal of Mechanics-B/Fluids, pp. 384-397.

Ali, N., Sajid, M., and Hayat, T., (2010a) Long wavelength flow analysis in a curved channel, Z. Naturforsch., 65 pp. 191–196.

Ali, N., Sajid, M., Javed, T. and Abbas, Z., (2010b) Heat transfer analysis of peristaltic flow in a curved channel, Int. J. of Heat and Mass Trans., 53 pp. 3319–3325.

Ali, N., Sajid, M., Javed, T., and Abbas, Z., (2010c) An analysis of peristaltic flow of a micropolar fluid in a curved channel. Chin. Phys. Letts. 28(1) pp. 0147041–0147044

Ali, N., Wang, Y., Hayat, T., and Oberlack, O., (2009) Slip effects on the peristaltic flow of a third grade fluid in a circular cylindrical tube, J. of App. Mech., 76 pp. 1-10.

Ariman, T., Turk, M. A., and Sylvester, N., (1974) Application of microcontinum fluid mechanics, Int. J. Eng. Sci. 12 pp. 273-293.

B.B., Gupta, and V., Seshardi, (1976) Peristaltic pumping in non-uniform tubes, J. Biomech., 77 pp. 105.

Barton, C., and Raynor, S., (1968) Peristaltic flow in tubes, Bull. Math. Biophys. 30 pp. 663–680.

Böhme, G., and Müller, A., (2013) Analysis of non-Newtonian effects in Peristaltic pumping, J. of Non-Newtonian Fluid Mech., 201 pp. 107–119.

Brown, T.D., and Hung, T.K., (1977) Computational and experimental investigations of two-dimensional nonlinear peristaltic flows, J. of Fluid Mech., 83 pp. 249-272.

Ceniceros, H.D., and Fisher, J.E., (2013) Peristaltic pumping of a viscoelastic fluid at high occlusion ratios and large Weissenberg numbers, J. of Non-Newtonian Fluid Mech., 171, pp. 31–41.

Chu Kwang-Hua, W., (1996) Stokes slip flow between corrugated walls, ZAMP, 34 pp. 591-598.

Chu, W.K., and Fang, J., (2000) On the peristaltic transport in small–Knudsen–number flow, Meccanica, 35 pp. 6.

Eldabe, N.T.M., El-Sayed, M.F., Ghaly, A.Y., and Sayed, H.M., (2008) Mixed convective heat and mass transfer in a non-Newtonian fluid at a peristaltic surface with temperature dependent viscosity, Arch. Appl. Mech., 78 pp. 599–624.

Elshahed, M., and Haroun, M. H., (2005) Peristaltic transport of Johnson-Segalman fluid under effect of a magnetic field, Mathematical Problems in Engineering, 6 pp. 663–677.

Elshehawey, E.F., and Husseny, S.Z.A., (2002) Peristaltic transport of magneto-fluid with porous boundaries, Appl. math. Comp., 129 pp. 421.

Elshehawey, E.F., Eladabe, N.T., Elghazy, E.M., and Ebaid, A., (2006) Peristaltic transport in an asymmetric channel through a porous medium, Appl. Math. Comp., 182 pp. 140.

Eringen, A. C., (1964) Some micro fluids. Int. J. Eng. Sci. 2 pp. 205-217.

Eringen, A. C., (2001) Microcontinuum Field Theories. II. Fluent Media, Springer Verlag, New York.

Fung, Y.C., and Yih, C.S., (1968) Peristaltic transport, Trans. ASME J. Appl. Mech., 33 pp. 669–675.

Goldstein, S., (1938) Oxford University Press, 1.

Haroun, M. H., (2007a) Effect of Deborah number and phase difference on peristaltic transport of a third order fluid in an asymmetric channel, Communications in Nonlinear Science and Numerical Simulation, 12 pp. 1464–1480.

Haroun, M.H., (2007b) Nonlinear peristaltic flow of a fourth grade fluid in an inclined asymmetric channel, Comp. Material Sci., 39 pp. 324-333.

Hayat, T., Abbasi, F. M., Al-Yami, M., and Monaquel, S., (2014) Slip and Joule heating effects in mixed convection peristaltic transport of nanofluid with Soret and Dufour effects. J Mol Liq. 194 pp. 93–99.

Hayat, T., Abbasi, F.M., Ahmed, B., and Narla, V.K., (2011d) Peristaltic Transport of Carreau-Yasuda Fluid in a Curved Channel with Slip Effects, PLos One, pp. 5126–5136.

Hayat, T., Ali, N., and Asghar, S., (2007) Peristaltic motion of a Burger's fluid in a planar channel, Applied Mathematics and Computation, 186 pp. 309–329.

Hayat, T., Ali, N., Asghar, S., and Siddiqui, A.M., (2006) Exact peristaltic flow in tubes with an endoscope, Appl. Math. Comp., 182 pp. 359.

Hayat, T., and Hina, S., (2010c) The influence of wall properties on the MHD peristaltic flow of a Maxwell fluid with heat and mass transfer, Nonlin. Anal. Real world appl., 11 pp. 3155-3169.

Hayat, T., and Noreen, S., (2010a) Peristaltic transport of fourth grade fluid with heat transfer and induced magnetic field, Comptes Rendus Mécanique, 338 pp. 518–528.

Hayat, T., Bibi, S., Alsaadi, F., and Rafiq, M., (2016) Peristaltic transport of Prandtl-Eyring liquid in a convectively heated curved channel, 11(6).

Hayat, T., Hina, S., and Ali, N., (2010b) Simultaneous effects of slip and heat transfer on the peristaltic flow, Commun Nonlinear Sci Numer Simulat., 15 pp. 1526–1537.

Hayat, T., Hina, S., and Hendi, A.A., (2011b) Peristaltic motion of Power-law fluid with heat and mass transfer, Chin. Phys. Lett., 28 pp. 084707(1–4).

Hayat, T., Hina, S., Hendi, A.A. and Asghar, S., (2011c) Effect of wall properties on the peristaltic flow of a third grade fluid in a curved channel with heat and mass transfer, Int. J Heat Mass Transfer, 54 pp. 5126–5136.

Hayat, T., Hussain, Q., and Ali, N., (2008) Influence of partial slip on the peristaltic flow in a porous medium, Physica A, 387 pp. 3399.

Hayat, T., Hussain, Q., Qureshi, M.U., Ali, N., and Hendi, A.A., (2011a) Influence of slip condition on the peristaltic transport in an asymmetric channel with heat transfer: An exact solution, Int. J. Numer. Meth. Fluids, 67 pp. 1944–1959.

Hayat, T., Noreen, S., and Qasim, M., (2013) Influence of heat and mass transfer on the peristaltic transport of Phan-Thien- Tanner fluid, ZNA, 68a pp. 751.

Hayat, T., Umar Qureshi, M., and Hussain, Q., (2009) Effect of heat transfer on peristaltic flow of an electrically conducting fluid in a porous space, Appl. Math. Model. 33 pp. 1862–1873.

Hayat, T., Wang, Hutter K, Asghar, S., and Siddiqui, A.M., (2004) Peristaltic transport of an Oldroyd-B fluid in a planar channel, Math. Problems in Eng., 4 pp. 347–376.

Hayat, T., Wang, Y., Siddiqui, A.M., and Hutter, K., (2003) Peristaltic motion of Johnson-Segalman fluid in a planar channel, Math. Problems in Eng., 1 pp. 1-23.

Hayat, T., Wang, Y., Siddiqui, A.M., Hutter, K., and Asghar, S., (2002) Peristaltic transport of third order fluid in a cylindrical tube, Math. Models and Methods in App. Sci., 12 pp. 169-176.

Hina, S., Hayat, T., and Asghar, S., (2012) Peristaltic transport of Johnson–Segalman fluid in a curved channel with compliant walls, Non-linear Analysis, Modeling and Control, 17 pp. 297-311.

Hina, S., Mustafa, M., Hayat, T., and Alsaedi, A., (2013a) Peristaltic flow of pseudo plastic fluid in a curved channel with wall properties, ASME J. Appl. Mech., 80 024501–024507.

Hina, S., Mustafa, M., Abbasbandy, S., Hayat, T., and Alsaedi, A., (2013b) Peristaltic Motion of Nanofluid in a Curved Channel, J. of heat transfer, 136 pp. 52001-52007

Jaffrin, M.Y., (1973) Inertia and streamline curvature effects in peristaltic pumping, Int. J. of Eng. Sci., 11 pp. 681-699.

Jaffrin, M.Y., and Shapiro, A.H., (1971) Peristaltic pumping, Annual Review of Fluid Mech., 3 pp. 13-37.

Javid, K., Ali, N., and Sajid, M., (2016) Simultaneous effects of viscoelasticity and curvature on peristaltic flow through a curved channel, Meccanica 51 pp. 87–98.

Kalantari, A., Sadeghy, K. and Sadeqi, S., (2013) Peristaltic flow of non-Newtonian fluids through curved channels: a Numerical Study, Ann. Trans. Nordic Rheol. Soc., 21 pp. 163-170.

Kothandapani, M., and Srinivas, S., (2008) On the influence of wall properties in the MHD peristaltic transport with heat transfer and porous medium, Physics Letters A, 372 pp. 4586–4591.

Latham, T.W., (1966) Fluid motion in peristaltic pump, MS Thesis, MIT Press, Cambridge, MA.

Maraj, E. N., and Nadeem, S., (2015) Application of Rabinowitsch fluid model for the mathematical analysis of peristaltic flow in a curved channel. Naturforsch. A 70 pp-513.

Mekheimer, Kh. S., (2008a) Peristaltic flow of a magneto-micropolar fluid: Effect of induced magnetic field; J. Appl. Math. 23 pp. 570825.

Mekheimer, Kh. S., and El Kot, M. A., (2008b) The micropolar fluid model for blood flow through a tapered artery with a stenosis, Acta Mech Sin, 24 pp. 637–644.

Mekheimer, Kh.S., (2003a) Nonlinear peristaltic through a porous medium in an inclined planar channel, J. Porous Media, 6 pp. 189.

Mekheimer, Kh.S., (2003b) Nonlinear peristaltic transport of magnetohydrodynamic flow in an inclined planar channel, Arab. J. Sci. Eng., 28 pp. 183.

Mekheimer, Kh.S., (2005) Peristaltic transport of a Newtonian fluid through a uniform and non-uniform annulus, The Arabian J. of Sci. and Eng., 30 pp. 71-83.

Mekheimer, Kh.S., and Abd elmaboud, Y., (2008c) The influence of heat transfer and magnetic field on peristaltic transport of a Newtonian fluid in a vertical annulus: Application of endoscope, Physics Letters A, 372 pp. 1657–1665.

Mishra, M., and Rao, A.R., (2005) Peristaltic transport in a channel with a porous peripheral layer: model of a flow in gastrointestinal tract, J. Biomech., 38 pp. 779.

Mishra, M., Rao, A.R., (2003) Peristaltic transport of a Newtonian fluid in an asymmetric channel, Z. Angew. Math. Phys., 54 pp. 532.

Mittra, T.K., and Parsad, S.N., (1974) Interaction of peristaltic motion with Poiseuille flow, The Bulletin of Math. Bio., 36 pp. 127-141.

Na, T.Y., and Pop, I., (1997) Boundary-layer flow of a micropolar fluid due to a stretching wall, Arch. Appl. Mech. 67 pp. 229–236.

Nabil, T. M. El-dabe, Sallam, N. S., Mona A. A., Mohamed, Y. A., and Assmaa, A. H., (2011) Effects of chemical reaction with heat and mass transfer on peristaltic flow of Jeffrey fluid through porous medium in an inclined asymmetric channel with Hall currents. International Journal of Applied Mathematics and Physics, 3(2), pp. 155-167.

Nadeem, S., and Akbar, N.S., (2008) Influence of heat transfer on a peristaltic transport of Herschel–Bulkley fluid in a non-uniform inclined tube, Comm. Nonlinear Sci. Num. Simul., 14 4100.

Narla, V. K., Prasad, K. M., and Ramanamurthy, J. V., (2013) Peristaltic Motion of Viscoelastic Fluid with Fractional Second Grade Model in Curved Channels. Chinese J. Eng pp. 582390.

Noreen, S., (2017) Peristaltic Flow in a non-Uniform Channel with Heat and Mass Transfer, Biomater Med. Appl. 1.

Pandey, S.K., and Tripathi, D., (2010) Influence of magnetic field on the peristaltic flow of a viscous fluid through a finite-length cylindrical tube, Appl. Bionics Biomech., 7 pp. 169.

Radhakrishnamacharya, G., and Murty, V.R., (1993) Heat transfer to peristaltic transport in a non-uniform channel, Defence Sci. J., 43 pp. 275.

Raju, K.K., and Devanathan, R., (1974) Peristaltic motion of a non-Newtonian fluid II: viscoelastic fluid, Rheol. Acta, 13 pp. 944.

Ramanamurthy, J.V., Prasad, K.M., and Narla, V.K., (2013) Unsteady peristaltic transport in curved channels, Phy. of Fluids, 25 pp. 091903–091920.

Sato, H., Kawai, T., Fujita, T., and Okabe, M., (2000) Two dimensional peristaltic flow in curved channels, Trans. Japan Soc. Mech. Eng. B, 66 pp. 679–685.

Shapiro, A.H., Jaffrin, M.Y., and Weinberg, S.L., (1969) Peristaltic pumping with long wavelength at low Reynolds number, J. Fluid Mech., 37 pp. 799-825.

Shehzad, S. A., Abbasi, F. M., Hayat, T., and Alsaadi, F., (2014) MHD mixed convective peristaltic motion of nanofluid with Joule heating and thermophoresis effects. PLoS one 9 pp. 11.

Shit, G.C., and Roy, M., (2014) Hydromagnetic effect on inclined peristaltic flow of a couple stress fluid, Alex. Eng. J., 53 pp. 949–958.

Siddiqui, A.M., and Schwarz, W.H., (1994) Peristaltic flow of second order fluid in tubes, J. of Non-Newtonian Fluid Mech., 53 pp. 257–284.

Siddiqui, A.M., Provost, A., and Schwarz, W.H., (1991) Peristaltic pumping of second order fluid in a planar channel, Rheol. Acta, 30 pp. 249-262.

Sokolnikoff, I.S., McGram, (1956) Mathematical theory of elasticity. Hill Book company New York.

Srinivas, S., and Kothandapani, M., (2008) Peristaltic transport in an asymmetric channel with heat transfer: a note, Int. Commun. Heat Mass Transf., 35 pp. 514.

Srinivas, S., and Kothandapani, M., (2009) The influence of heat and mass transfer on MHD peristaltic flow through a porous space with compliant walls, Appl. Math. Comput., 213 pp. 197–208.

Srinivas, S., Gayathri, R., and Kothandapani, M., (2011) Mixed convective heat and mass transfer in an asymmetric channel with peristalsis, Commun. Nonlinear Sci. Numer. Simul. 16 pp. 1845–1862.

Srinivasacharya, D., Mishra, M., and Rao, A. R., (2003) Peristaltic pumping of a micropolar fluid in a tube, Acta. Mech., 161 pp. 165-178.

Srivastava, L.M., and Srivastava, V.P., (1985) Interaction of peristaltic flow with pulsatile flow in a circular cylindrical tube, J. of Biomech., 18 pp. 247-253.

Takabatake, S., and Ayukawa, K., (1982) Numerical study of two-dimensional waves, J. of Fluid Mech., 122 pp. 439-465.

Takabatake, S., Ayukawa, K., and Mori, A., (1988) Peristaltic pumping in circular cylindrical tubes: a numerical study of fluid transport and its efficiency, J. of Fluid Mech., 193 pp. 267-283.

Tang, D., and Rankin, S.M., (1992) Peristaltic transport of a heat-conducting viscous fluid as an application of abstract differential equations and semi-group of operators, J. Math. Anal. Appl., 169 pp. 391.

Tang, D., and Shen, M.C., (1993) Non-stationary peristaltic transport of a heat-conducting fluid, J. Math. Anal. Appl., 174 pp. 265.

Tanveer, A., Hayat, T., Alsaedi, A., and Ahmad, B., (2017) Mixed convective peristaltic flow of Sisko fluid in curved channel with homogeneous-heterogeneous reaction effects, Journal of Molecular Liquids, 233, pp. 131-138.

Tanveer, A., Hina, S., Hayat, T., Mustafa, M., and Ahmed, B., (2016) Effects of the Cattaneo–Christov heat flux model on peristalsis. Engineering applications of computational fluid mechanics, 10 pp. 373-383.

Tripathi, D. and Bég, O.A., (2013) Mathematical modelling of heat transfer effects on swallowing dynamics of viscoelastic flood bolus through the human esophagus, Int. J Thermal Sci., 70 pp. 41-53.

Tripathi, D. and Bég, O.A., (2014a) Mathematical modelling of peristaltic propulsion of viscoplastic bio-fluids, Proceedings of the Institution of Mechanical Engineers, Part H, J. of Eng. in Med., 228 pp. 67–88.

Tripathi, D., (2012b) A mathematical model for swallowing of food bolus through the oesophagus under the influence of heat transfer, Int. J. Thermal Sci., 51 pp. 91.

Tripathi, D., and Bég, O.A., (2012a) A study of unsteady physiological magneto-fluid flow and heat transfer through a finite length channel by peristaltic pumping, Proceedings of the Institution of Mechanical Engineers, Part H, J. of Eng. in Med., 226 pp. 631–644.

Tripathi, D., and Bég, O.A., (2014b) A study on peristaltic flow of nanofluids: Application in drug delivery systems, Int. J. Heat and Mass Transfer, 70 pp. 61.

Vajravelu, K., Radhakrishnamacharya, G., and Radhakrishnamurty, V., (2008) Peristaltic flow and heat transfer in a vertical porous annulus with long wavelength approximation, Int. J. of Nonlinear Mech., 42 pp. 754–759.

Walker, S.W., and Shelley, M.J., (2010) Shape optimization of peristaltic pumping, J. of Comp. Phy., 229 pp. 1260–1291.

Wang, Y., Hayat, T., Ali, N., and Oberlack, M., (2008) Magnetohydrodynamic peristaltic motion of a Sisko fluid in a symmetric or asymmetric channel, Physica A, 387 pp. 347–362.